PARTICLE-IN-CELL SIMULATIONS OF FAST ELECTRON TIME SCALE PHENOMENA

By

CHANDRASEKHAR SHUKLA

PHYS06201104004

INSTITUTE FOR PLASMA RESEARCH, GANDHINAGAR

A thesis submitted to the
Board of Studies in Physical Sciences

In partial fulfillment of the requirements
for the Degree of

DOCTOR OF PHILOSOPHY

of

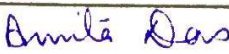## HOMI BHABHA NATIONAL INSTITUTE

February 2017

Homi Bhabha National Institute[1]

Recommendations of the Viva Voce Committee

As members of the Viva Voce Committee, we certify that we have read the dissertation prepared by **Chandrasekhar Shukla** entitled " **Particle In Cell Simulations of the Fast Electron Time Scale Phenomena** " and recommend that it may be accepted as fulfilling the thesis requirement for the award of Degree of Doctor of Philosophy.

Chairman - Prof. Subroto Mukherjee	*signature*	Date: 25/07/17
Guide / Convener – Prof. Amita Das	*signature*	Date: 25/07/17
Co-guide - <Name> (if any)		Date:
Examiner – Prof. G. Ravindra Kumar	*signature*	Date: 25/07/17
Member 1- Prof. Abhijit Sen	*signature*	Date: 25/07/17
Member 2- Prof. Sudip Sengupta	*signature*	Date: 25/07/17

Final approval and acceptance of this thesis is contingent upon the candidate's submission of the final copies of the thesis to HBNI.

I/We hereby certify that I/we have read this thesis prepared under my/our direction and recommend that it may be accepted as fulfilling the thesis requirement.

Date:

Place:

(**Prof. Amita Das**)

Co-guide (if applicable)　　　　　　　　　**Guide**

---

[1] This page is to be included only for final submission after successful completion of viva voce.

STATEMENT BY AUTHOR

CHANDRASEKHAR SHUKLA

DECLARATION

I, hereby declare that the investigation presented in the thesis has been carried out by me. The work is original and the work has not been submitted earlier as a whole or in part for a degree/diploma at this or any other Institution or University.

CHANDRASEKHAR SHUKLA

List of Publications arising from the thesis

List of Publications

Publications in Peer Reviewed Journals:

- **Absorption of laser energy in interaction of intense short pulse laser- rippled plasma target**,
  Chandrasekhar Shukla and Amita Das
  In preparation for journal publication

- **Particle-in-cell simulation of two-dimensional electron velocity shear driven instability in relativistic domain**,
  Chandrasekhar Shukla, Amita Das, and Kartik Patel
  Physics of Plasmas, 23(082108), 2016.

- **Two-dimensional studies of relativistic electron beam plasma instabilities in an inhomogeneous plasma**,
  Chandrasekhar Shukla, Amita Das, and Kartik Patel
  Physics of Plasmas, 22(112118), 2015.

- **1d3v pic simulation of propagation of relativistic electron beam in an inhomogeneous plasma**,
  Chandrasekhar Shukla, Amita Das, and Kartik Patel
  Phys. Scr., 90(085605), 2015.

Conferences/Schools:
International Participation

- Propagation of relativistic electron current through an inhomogeneous plasma. (Talk), Chandrasekhar Shukla, Amita Das, Kartik Patel, and Predhiman Kaw
  ASHULA, 5th - 7th Jan 2016, Osaka, Japan.

- Transportation of relativistic electron beam in laser-nano structured target interaction. (Talk), Chandrasekhar Shukla, Amita Das, and Kartik Patel
  APFA, 14th - 18th Dec 2015, Gujrat, India.

- International School on Ultra-Intense Lasers, Moscow, Russia, 4th- 9th Oct 2015.

- Particle-in-cell simulations of counter-streaming electron beam in an inhomogeneous background plasma . (Talk), Chandrasekhar Shukla, Amita Das, and Kartik Patel
  ASHULA, 20th - 21st Jan, 2015, Lonavala, India.

- Particle-in-Cell simulation of non-linear evolution filamentation instability in counter-streaming relativistic beams. (Poster), Chandrasekhar Shukla, Amita Das, and Kartik Patel
  29th National Symposium on Plasma Science and Technology and International Conference on Plasma and Technology, 8th-11th Dec 2014, Kerala, India.

- Particle-in-Cell simulations of electron beam propagation through plasma medium. (poster), Chandrasekhar Shukla, Amita Das, and Kartik Patel
  10th International Conference on High Energy Density Laboratory Astrophysics, 12th-16th May, 2014, Bordeaux, France.

- Particle-in-Cell simulation of relativistic counter-streaming electrons through an inhomogeneous Dense Plasma. (Poster), Chandrasekhar Shukla, Amita Das, and Kartik Patel
  ASHULA, Seoul, Korea, 20th - 22nd January, 2014.

- Nonlinear evolution of the Weibel instability of counter-streaming relativistic electron beams. (Poster), Chandrasekhar Shukla, Amita Das, and Kartik Patel
  CNSD, IIT, Indore, INDIA, 11th - 14th December, 2013.

- Particle-in-Cell simulation of transportation of electron beam through an inhomogeneous dense plasma. (Poster),
  Chandrasekhar Shukla, Amita Das, and Kartik Patel
  LPAW, Goa, India, 2nd - 6th September, 2013.

National Participation

- Guiding of relativistic electron beam through the structured plasma. (Poster), Chandrasekhar Shukla, Amita Das, and Kartik Patel
  PSSI, (KIIT), Bhubhaneshwar, India, 3rd - 6th December, 2013.

- DST SERC School on Tokamaks and Magnetized Plasma Fusion 25th-Feb to 15th-Mar-2013.

CHANDRASEKHAR SHUKLA

Dedicated to

My family and friends

ACKNOWLEDGEMENTS

complete my thesis work.

Contents

SYNOPSIS

There has been rapid progress in high-intensity short pulse laser technology recently. These lasers are capable of delivering enormous energy density ranging from 10^{18} W/cm^2 to $10^{22} W/cm^2$ in femtosecond time scales. When such a laser is incident on a solid target, the target gets ionized and gets converted into a plasma. At such short time scales, only the lighter electron species of the plasma interacts with the laser field. Thus the incident laser energy is primarily absorbed by the electrons creating fast energetic electrons. These electrons can help transport energy in the overdense region of the plasma which is inaccessible to lasers. In fact Fast Ignition (FI) [1] scheme of laser fusion depends crucially on energy transport through electrons in the dense core region for ignition. Thus it would be desirable to have schemes which improves the laser absorption efficiency to generate energetic electrons and also improves its unhindered propagation towards the dense plasma region. In this thesis one such idea, namely that involving structured targets is investigated and significant improvement in both the properties are demonstrated. We have used Particle - In - Cell (PIC) code PICPSI [2] to study the interaction of laser with a target plasma. A comparison of laser energy absorption in the case of a homogeneous target and when the target is structured (by placing a periodic array of nano-wires transverse to the laser propagation direction) has been made. The pre-pulse of the high intensity lasers in general ionizes the target material and converts it into a plasma. Thus it is the plasma which interacts with the main laser pulse. In the case of structured nano-wire targets, the attached nano-wires also get ionized by the pre-pulse. However, since the plasma can expand only at a slow ion acoustic speed c_s, the interaction of the main pulse sees a target plasma having a spatial inhomogeneity at the scale of the nano-wires, transverse to the laser propa-

iv

gation direction. The laser interaction with such a structured target plasma in the PIC simulation is mimicked by a configuration of sinusoidal ripple of the plasma density transverse to the laser propagation direction. The scale length of the ripple was varied in the study. The results show that there is significant improvement in the laser absorption in the case of laser interacting with such structured targets. This has been understood on the basis of a novel vacuum heating like mechanism [3] by us. It occurs as the plasma density inhomogeneity at the surface of the nano-wire acts like a vacuum plasma interface prompting a vacuum heating like absorption. The plasma density inhomogeneity due to the structures ensures that even for the case of normal incidence of the laser the vacuum heating like mechanism is operative in the transverse direction. Thus the geometry of structured targets in fact enhances the absorption of the laser light. The second important observation made by us in simulations is that the subsequent propagation of the energetic electrons is also significantly collimated over much longer distances in the case of structured targets in simulations. This has been understood on the basis of the suppression of certain instabilities which are invariably present in a beam plasma system. It is well known that the fast electrons generated in intense laser-solid interaction propagate inside the overdense plasma and are able to carry currents more than Alfvén current limit I_A ($I_A \approx 17\beta\gamma$ kAmps where $\beta = v_e/c$ and γ is Lorentz factor). In vacuum this is impossible as the self generated magnetic fields will turn the trajectories of the electrons responsible for the current. However in plasma, current propagation exceeding Alfvén current limit occurs as a result of a return reverse shielding current from the background electrons. If the focal spot size of an electron beam is less than the skin depth (c/ω_p) of plasma, the induced return currents flows outside the beam otherwise it flows within the beam.

In overdense case, the transverse spot size of the fast electron beam is nearly equal to the focal spot size of laser which is in general much greater than the skin depth of plasma. In this case, the return current spatially overlaps with the fast electron current and annihilates the magnetic field. This full and/or partial annihilation of the magnetic field in plasma permits the fast electron transportation with current exceeding the Alfvén limit. Thus the spatially overlapping configuration of forward and return current has no net magnetic field to stop the propagation of electrons. However, the spatially overlapping oppositely propagating forward and reverse shielding currents are unstable to several micro- instabilities. The most dominating is Weibel or filamentation instability [4, 5], which can lead to spatial separation of currents and generate huge magnetic fields. The generated magnetic field can in turn deflect the electrons and is thus detrimental to their propagation. This poses serious limit to the propagation of energetic electrons in plasma. As stated above we have demonstrated a significant suppression of the growth rate of the beam Weibel instability in our simulations for structured targets in both 1-D and 2-D simulations. Once the energetic electrons move past the electron skin depth region the laser fields have no role to play and it propagates under the influence of its own self consistently generated fields as well those due to that of the reverse shielding currents. The evolution of an interpenetrating spatially overlapping oppositely flowing currents of electrons were considered by PIC simulation. In 1-D simulations the variations are chosen to be perpendicular to the current flow direction. This geometry permits the Weibel destabilization. In 2-D two distinct geometries are possible, one in which the 2-D plane is orthogonal to the current flow direction. The other is the one for which the current flow is along one of the dimensions of the 2-D simulation box. In the former only variations normal to

the current propagation (e.g. Weibel/filamentation instability) are permitted. In the latter both Weibel and electrostatic two stream instabilities can get excited. Simulations were carried out in both the configurations. The linear instability leading to current separation is clearly visible. In the latter 2-D configuration one observes appearance of tilted magnetic field lines which is in conformity with the fact that the oblique mode typically has the maximum growth rates. A detailed study of growth rates of maximally growing modes observed from the simulations is compared with the growth rate obtained from a two fluid description obtained by linearization and eigen value evaluation process. The growth rate obtained from simulations match reasonable well with those obtained from linearized eigen values. The nonlinear regime shows the development of longer scales. We explore these instabilities in the nonlinear regime. We also study the effect of plasma density inhomogeneity on these instabilities. The inhomogeneity is chosen to mimic the behaviour of the presence of structured targets. In this inhomogeneous case a clear suppression of the instability is observed. The above simulations were all carried out for a periodic geometry, which assumes an infinite transverse extension of the beam. For realistic cases, the relativistic electron beam would be produced with a finite transverse width, typically commensurate with the laser focal spot. The propagation an electron beam with a finite width will also induce return current in background electron. However, this return current may not be able to completely spatially overlap with the beam current . There will be an imbalance at the edges. Thus at the edge, there would appear a sheared flow between the plasma and beam. Such a sheared configuration in electron flow would also arise in the aftermath of Weibel instability, wherein the forward and the reverse shielding currents get spatially separated and the oppositely propagating filaments merge with each

other. Keeping this in view, we have also carried out the numerical study of the instabilities associated with a 2-D sheared electron flow configuration against a neutralizing background of ions. Analysis of sheared electron configuration has been carried out earlier in the context of electron magnetohydrodynamic (EMHD) fluid description for non relativistic and weakly relativistic cases [6]. EMHD fluid simulations studies have also been carried out for the nonrelativistic case. Here we carry out PIC studies for the sheared electron flow configuration in the regime of both weak and strong relativistic flow velocities. We have shown the development of Kelvin Helmholtz instability and the formation of electromagnetic KH vortices. When the flow velocities are weakly relativistic we find that they agree with the predictions made by EMHD model earlier [6, 7]. However, for mild and strong relativistic case, we have seen that the fluid tends to become fairly compressible. Since EMHD model provides a description for incompressible electron flow, the PIC observations significantly deviate from the EMHD fluid inferences. The PIC studies shows a development of electron density oscillations at the beam edge constituting compression and rarefaction. This observation was then understood on the basis of one-dimensional magnetized relativistic electron fluid equations for electrostatic disturbances. We find that the compression and rarefaction are upper hybrid oscillation which suffers breaking in the nonlinear regime. The final turbulent behaviour of the observed magnetic fields in the simulations were identified with the help of their spectral behaviour. In the turbulent stage for weakly relativistic flows there is a slow cascade of energy from short to long scales. While for mild and strong relativistic cases the energy continues to remain trapped at higher k modes. To summarize, in this thesis we have carried out PIC studies for several fast time scale phenomena involving only the lighter electron species in the

plasma. In particular we have studied the process of energetic electrons generation by the absorption of laser energy in the plasma. We identified the presence of a novel vacuum heating like mechanism in the context of structured targets which enhances the laser absorption process. We have also considered the propagation of energetic electron beam in the plasma and its associated instabilities in simulations for both ordinary and structured targets. We observe that the instabilities which are responsible for scattering the electron beam and hindering its propagation get suppressed in the presence of structured targets when the inhomogeneity scale length is shorter than the skin depth. The plasma density inhomogeneity perpendicular to the flow direction with scale length shorter than skin depth provides a coupling between the growing electromagnetic mode and the short scale perturbations. Thus, the inhomogeneity acts as a conduit for the transfer of the energy of the growing mode to short scale damped perturbations resulting in the suppression of the growing modes. We have simulated the sheared electron flow configuration with the help of PIC simulations. The growth of Kelvin Helmholtz mode has been observed. While in the weakly relativistic case it matches with the prediction of the EMHD fluid model, in mild and/or strongly relativistic case the compressibility effects dominate. electron density pinching constituting compression and rarefaction is observed which at later stage is observed to undergo wave breaking. We identify this as the electrostatic upper hybrid oscillations which suffers wave breaking ultimately. The thesis has thus addressed certain issues associated with the generation and propagation of energetic electron in plasmas. The 3-D simulations, finite beam size effects (both transverse and longitudinal) etc., are some questions which remain to be explored for future studies.

List of Figures

1

Introduction

The thesis concentrates on the study of fast electron scale phenomena in plasmas using Particle - In - Cell (PIC) simulation. In particular, the interaction of fast femtosecond laser pulse with plasma has been studied, which is responsible for the excitation of phenomena at fast electron time scales. The laser power gets absorbed as a result of interaction with plasma electrons. The propagation of energetic electrons in the plasma results in a host of phenomena related to beam-plasma instabilities that get excited. In this work, the absorption of laser energy and the beam plasma instability in the presence of plasma density inhomogeneity has been studied in considerable detail.

1.1   Introduction

In the last few decades, there has been a rapid progress in high-intensity short pulse laser technology. At present lasers are capable of delivering enormous energy density ranging from $10^{18}W/cm^2$ to $10^{22}W/cm^2$ within a couple of femtoseconds. When such a laser irradiates a solid target, the target ionizes and converts into a plasma instantaneously. The time scale of the laser being rapid, the lighter electron species in the plasma are typically the only one suited to interact with the electromagnetic field of the laser. Thus the behaviour of subsequent processes are predominantly governed by electron dynamics. At higher intensities bordering close to $10^{22}W/cm^2$ ion involvement would also be expected even at such rapid time scales. We have, however, focused in this thesis on the study of that regime of laser plasma interaction where electrons species alone plays a dominant role in

dynamics.

The study of electron dynamics under the influence of high power laser fields in a plasma medium attracts a great deal of attention amongst the scientific community. The reason being that the understanding of such a system is applicable to a variety of frontier research areas ranging from astrophysics to laboratory experiments which are both of fundamental interest as well as cater to development of cutting edge technologies. For instance, such applications are in the areas of fusion technology through Fast Ignition Scheme (FIS) in inertial confined fusion (ICF) [1,8,9], plasma based particle accelerators [10–12], plasmas switches [13] etc. In addition a variety of physical phenomena related to fundamental interest such as magnetic reconnection [14–16], gamma rays bursts [17], generation of magnetic field in early universe [18] etc., are some issues which seem to be also crucially tied up with the behaviour of electrons in high intensity electromagnetic fields which can now be reasonably mimicked in a laboratory setting. The *laser energy absorption resulting in the creation of energetic electrons* and the *propagation and dynamics of energetic electrons through plasma* are two key aspects in most of the applications and fundamental phenomena that have been listed above.

The crucial role that these two aspects have in the context of Fast ignition (one of the frontier problem of interest) can be understood by the following discussion. In conventional ICF scheme, the spherical fuel target pellet is compressed and ignited with a very slow nano-second laser pulse. This process is not very efficient from the point of view of energetics. The system is susceptible to the hydrodynamic Rayleigh Taylor (RT) instability which mixes the hot and cold fluids making the condition to achieve ignition temperature difficult. The effect of RT instability can be avoided by imposing stringent conditions on the precise spherical symmetry of the imploding fuel capsule as well as the incident laser pulse, which is difficult and almost impossible to achieve. The other option that has been thought of is that of fast ignition scheme, wherein the task of compression and heating for ignition are separated. A tailored slow nanosecond laser pulse first merely compresses the target fuel. The fuel remains cold during this phase and hence compression is easier. After compression, an ignitor laser pulse of sub - picosecond duration is sent. The compressed target being overdense for this laser, the laser energy is absorbed at the critical density layer (critical density n_c is decided by laser wavelength as $n_c = (\omega_L^2 m_e/4\pi e^2)$ where ω_L is laser frequency, m_e is the electron mass, and e is the

4

electronic charge) generating fast energetic electrons. These energetic electrons are expected to propagate inside a high density core region and dump their energy over a localized region to create the hot spot for ignition. It is thus clear that the success of fast ignition crucially hinges upon efficient absorption of laser energy and also the subsequent propagation of the energetic electrons through the plasma. The generation and evolution of magnetic field in laboratory laser plasma experiments is another area where the propagation of energetic electron beam through plasma plays a crucial role and its proper understanding is important.

In this thesis, we focus on the issue of laser absorption and the propagation of energetic electron beam through plasma using Particle - In - Cell (PIC) simulations. Lately, there have been some experiments in which structured targets were used to study their implication on improved energy absorption [19–24] as well as collimated propagation characteristics of energetic electrons [25] through plasma. This has been studied in detail here with the help of PIC simulations. In the next section of this Chapter, we introduce some preliminary concepts on laser-plasma interaction. A brief review of earlier works on fast electron time scale phenomena, relevant to present thesis, have been provided in section 1.3. Section 1.4 summarizes the salient aspects of the thesis.

1.2   Laser-plasma interaction

For high intensity laser pulses, the pre-pulse and/or the rising edge of the laser light itself has sufficient power to ionize the solid target it impinges upon. Thus target surface is thus converted into a dense plasma. The trailing laser pulse interacts with plasma. Plasma is instrumental in getting the laser energy absorbed. The next subsection, summarizes certain well known processes of the intense laser absorption mechanisms in plasma. The creation of energetic electrons, their propagation in the plasma medium and its susceptibility to various instabilities has been elaborated upon in the subsequent subsections.

1.2.1   Light absorption and generation of hot electrons

The absorption, reflection or propagation of laser wave in plasma depends on characteristic features of laser as well as the plasma. The intensity of the laser, its

pulse duration, the shape of the pulse, laser wavelength, polarization, angle of the incident etc., are the main effective parameters of laser which influence the absorption process. The plasma density profile and the scale length of its inhomogeneity are the plasma related important determining factors for the absorption process.

In vacuum, an electron oscillates in the electric field of the laser light. If the strength of laser electric field strong for the electron to be in relativistic regime, it makes a figure-8 trajectory and drifts along the laser propagation direction. However, ultimately there is no gain of energy by the free electron as the laser pulse goes past it. In plasma, however, the presence of ions creates a different scenario. The oscillating electrons collide with ions and thereby transfers a part of laser wave energy into the thermal energy of the plasma. The electron - ion Coulomb collision frequency is given as [26]

$$\nu_{ei} = \frac{e^4 n_e Z ln\Lambda}{4\pi \epsilon_0^2 m_e^2 v_e^3}, \tag{1.1}$$

Where e and Ze are electron and ion charge respectively. The plasma electron density is n_e and $ln\Lambda$ is Coulomb logarithm and v_e is the velocity of electrons relative to the ion scattering centre. Thus we can see that electron-ion collision frequency depends on electron density and relative velocity of colliding charge particles.

When the intensity of laser beam is low (e.g. $< 10^{15}W/cm^2$) and pulse duration is long ($\sim ns$), collisional absorption processes dominate and heat the plasma. The main collisional absorption processes are inverse bremsstrahlung [27, 28] and normal skin effect [29]. When the laser intensity is high (e.g. $I > 10^{15}W/cm^2$), the quiver velocity of electrons oscillations become high (with energies $\sim 1keV$). Since electron-ion collision frequency ν_{ei} is inversely proportional to the cube of velocity of colliding charge particles ($\propto v_e^{-3}$), the collisional absorption process is thus ineffective at high laser intensities. Thus, for laser intensity $I > 10^{15} W/cm^2$, collisionless absorption processes start becoming dominant [30]. The dominating collisionless absorption processes are anomalous skin effect, sheath inverse bremsstrahlung [31], sheath transit absorption [32], resonance absorption [33], vacuum (Brunel) heating [3], $\mathbf{J} \times \mathbf{B}$ acceleration [34], ponderomotive acceleration [35, 36], stochastic heating [37], and absorption due to parametric decay instabilities [38]. While vacuum heating, resonance absorption, $\mathbf{J} \times \mathbf{B}$ acceleration, and

ponderomotive acceleration processes are dominant for overdense plasmas, stochastic and parametric decay instabilities aid the absorption processes in underdense plasmas.

In resonance absorption case, the obliquely incident (i.e. $\theta > 0$) p-polarized laser reflects before reaching to the critical density n_c to satisfy the momentum conservation (incident **K**-wave vector conservation). The plasma density n_r from where the laser wave gets reflected is given by

$$n_r = n_c cos\theta, \tag{1.2}$$

At the turning point, the electric field component of the incident wave generates an oscillating standing wave. In case of a sufficiently small distance between the turning point and the position of the critical density, the evanescent electric field excites plasma electron oscillations parallel to density gradient direction within the region of the reflection and the critical density point. This localized and quasi-standing plasma wave satisfying resonance condition reaches high amplitude and ultimately suffers wave breaking generating a sufficiently high number of energetic electrons. This process is called resonance absorption and dominates all other processes when the condition

$$\omega_L L/c \sim sin\theta, \tag{1.3}$$

is satisfied. Here L is the plasma density scale length and ω_L is the laser frequency.

A collisionless absorption mechanism for p-polarized laser pulse obliquely incident on steep plasma density surface is given by Brunel [3]. This mechanism is known as Brunel's heating or vacuum heating. In this mechanism, the laser electric field pulls the electron from surface boundary to vacuum in half of its cycle and in the next half cycle it accelerates the electrons, thereby increasing the kinetic energy of the electrons. This mechanism is highly efficient when following conditions are satisfied

$$L < v_{osc}/\omega_L; \quad v_{osc} > v_t$$

Where v_{osc} and v_t are the quiver and the thermal velocity of the electron respectively.

The intensity at which the quiver velocity of electrons become comparable to

the speed of light c is known as relativistic intensity. A normalized vector potential a_0 is defined as

$$a_0 = \frac{eA}{m_e c^2}.$$ (1.4)

For $a_0 \geq 1$ the electron motion becomes relativistic. This corresponds to an intensity of $I \geq 10^{18} W/cm^2$. In this range the magnetic field B of the laser starts to influence the electron trajectory by the Lorentz force component $\mathbf{v}_e \times \mathbf{B}$. The resultant Lorentz force accelerates the electron in laser propagation direction. This mechanism is known as $\mathbf{J} \times \mathbf{B}$ heating process.

Thus when an intense short pulse laser interacts with an overdense plasma, absorption processes lead to a sizeable fraction of electrons having much higher mean kinetic energy. These electrons are known as the supra-thermal component (and/or hot electrons component) and can often be in a form of relativistic electron beam.

1.2.2 Propagation of relativistic electron beam in overdense plasma

The fast electrons generated in intense laser-solid interaction has a density of the order of critical density, i.e., $\sim 10^{22}$. The velocity of these electrons being close to the speed of light, these electrons carry currents which is of the order of $\sim MAmps$ [39, 40]. In vacuum, the electron trajectories carrying this current would turn due to the self generated magnetic field. In fact, the maximum current that an electron beam can carry in vacuum is provided by the Alfvén current limit, which is $17\beta\gamma$ kAmps, where $\beta = v_e/c$ and γ is the Lorentz factor. In plasma, propagation of fast electrons with current exceeding the Alfvén limit is permissible. In the presence of plasmas, the charge imbalance generated by the beam causes electrostatic fields to which the background plasma electrons respond by flowing in the reverse direction. If the focal spot size of an electron beam is less than the skin depth (c/ω_p) of plasma, the induced return currents flow outside of beam, else the reverse shielding current also flows within the beam. Typically, the focal spot size of the fast electron beam is nearly equal to the focal spot size of the laser. In overdense case, this is much greater than the skin depth of plasma. In general, thus the return current spatially overlaps with fast electron currents and annihilates the magnetic field

generated by the fast electrons. The full or partial annihilation of the magnetic field in plasma permits the fast electron transportation even though the Alfvén current limit is exceeded.

1.2.3 Beam-plasma instability

The configuration of spatially overlapping forward and return current is, however, susceptible to a host of beam-plasma instabilities which drastically influence the propagation of beam electrons in the plasma. For instance, the two stream instability [41], Weibel instability [4], filamentation [5] and oblique modes instability [42] are some instabilities which have a profound influence on electron beam propagation in the plasma.

Langmuir observed oscillations in electron beam-plasma system for the first time in 1925 [43]. Subsequently in 1948 Pierce demonstrated that these oscillations might be unstable. Bohm and Gross developed a kinetic theory to study unstable perturbations that propagate along beam direction. This class of instability has been termed as the two-stream instability [41]. This instability has a pure longitudinal electrostatic character that creates charge density bunching in the direction parallel to the beam propagation. The bunching of electrons creates space charge separation. Their are two populations of electrons, one which gets trapped and oscillate in the space charge potential and other with higher kinetic energy are passing particles and remain un-trapped. The oscillating electrons form nonlinear coherent structures such as vortices in phase space. The energy boundary where the kinetic energy of a charged particle equals to electric potential energy is knowns as separatrix. The separatrix defines the boundary between the trapped and untrapped electrons.

Fried showed that beam-plasma system may also be unstable to electromagnetic perturbations that vary normal to the flow direction of the beam [5]. This class of instability is known as "filamentation instability". The unstable perturbation breaks up a homogeneous electron beam into small-scale current filaments, and are responsible for the generation of magnetic fields. In fact, temperature anisotropy in electron fluid also results in such a separation as demonstrated by Weibel in 1959 [4] and has been subsequently termed as the Weibel instability.

In actual scenario, the perturbations are the superposition of randomly oriented

modes. The eigen mode with the maximum growth rate grows with time and is the one to be observed. The maximally growing mode may have variations oblique to the beam propagation direction. In that case, both two-stream and filamentation instability characteristics are coupled to each other, and it is known as oblique mode instability. Sometimes it is also referred as coupled Two-Stream Filamentation (TSF) instability [42]. The tilted current filaments in beam-plasma system are the signature of this instability [44, 45].

1.3 Review of earlier works relevant to thesis

We now briefly review theoretical, numerical and experimental works carried out earlier in the area of intense laser-solid interaction which are relevant for the work that has been carried out in the thesis here. We, therefore, focus specifically issues pertaining to electron energy gain through laser and its dynamics in plasmas.

Lately, there has been a great deal of interest towards possible mechanisms of enhancing laser energy absorption so as to increase the number and the energy of hot electrons [46–52]. Most of these studies have emphasized the role of laser pulse duration, intensity, role of pre-plasma formation on the front surface of the target etc. It is reported that the presence of pre-plasma on the front surface of the target increases the absorption of laser energy as well as the number of hot electrons [48,53,54]. Recently, a novel technique of structured target has been used which shows significant absorption of laser energy as compared to the conventional approaches. Both experimental and simulation work have been carried out towards observing and understanding increased production of hot electrons by designed target [19–23]. We investigate the absorption of laser energy in rippled plasma targets, where the ripples mimick the inhomogeneous plasma density created by the ionization of nano structures protruding from the target surface by the pre-pulse of laser light.

The propagation of hot electrons which get generated in the target by laser energy absorption is another area of wide interest. The techniques for possible guiding and reduction in divergence of beam propagation through plasma medium are being explored. It is well known that the beam propagation in the plasma is fraught with various instabilities which are responsible for deterioration in the

beam transport. The attempt has been, therefore, towards curbing the growth of such instabilities.

Some other technique involves the resistive collimation of fast electrons by generating guiding magnetic field on the boundary of two different material. This has been proposed in Ref. [55]. The experimental investigations, based on this scheme, have been carried out by S. Kar *et al.* [25] and shown the similar results which were predicted in Ref. [55]. Another experimental work by Chatterjee *et al.* involves using aligned carbon nanowire arrays as the target. The irradiation of such a target generates inhomogenous plasma. They have demonstrated experimentally efficient transportation of laser-generated mega- ampere electron currents over long distances compared to flat solid target [24]. A theoretical interpretation was provided by Mishra *et al.* which suggests that the beam Weibel instabilities get suppressed in such inhomogeneous targets [56]. We present the 1-D and 2-D PIC (Particle - In - Cell) simulation of counter-steaming plasma with rippled background density, and discuss the beam-Weibel instability in this case.

The beam-Weibel or current filamentation instability have been extensively studied theoretically as well as numerically in the context of laser-solid interaction as well as the astrophysical scenario. This instability leads to current separation and generation of magnetic fields [57]. The Weibel instability maximizes at the electron skin depth scale. The current filaments, therefore, in the aftermath of the Weibel instability form at the scale length of electron skin depth. The subsequent nonlinear evolution the filaments have shown in PIC simulations to undergo the process of merging and coalascence processes forming long scale current structures. The separated current filaments have sheared electron flow configuration and are, therefore, susceptible to shear flow instabilities of magnetized electron flow [58]. In the non-relativistic limit, the electromagnetic effects on KH instability in the context of sheared electron flows have been investigated in detail by employing the Electron Magnetohydrodynamic (EMHD) model by Jain *et al.* [59]. Relativistic effects on sheared-electron flow led instability have been explored in Ref. [6]. We have conducted the particle-in-cell (PIC) simulation technique to understand the electrons dynamics at electron time scale in context to laser-plasma interaction and have demonstrated the results in subsequent chapters.

11

1.4   Layout of the thesis

This thesis is divided into 7 chapters in the following manner. In Chapter 2, we provide a brief introduction to the Particle - In - cell simulation technique which has been adopted for most of the work in this thesis. The basic algorithms which are used to develop the fully electromagnetic relativistic code have been described in this chapter. In Chapter 3, we present PIC studies on absorption of high-intensity short pulse laser-plasma interactions. We have chosen structured targets with inhomogenous density for the purpose. We demonstrate that for the structured targets the laser absorption is better. The dependence on scale length of the inhomogeneity on absorption efficiency has also been studied. We have then investigated the question of the role of inhomogeneity in suppressing the beam-plasma instabilities for efficient transport of the energetic electrons in the plasmas For this purpose in Chapter 4 we consider the evolution of counterpropagating electron currents in 1-D PIC simulations. It is demonstrated that the rippled targets are better suited for the task. In Chapter 5, we consider the 2-D case. The multidimensional nature of unstable spectrum in 2-D from the simulation and a two fluid model has been considered which show the suppression of the instabilities when the rippled density scale lengths are shorter than the skin depth. The nonlinear regime of the instability has also been explored through PIC studies.

In laser-plasma interaction, the relativistic electron beam is produced with finite beam width being commensurate with the laser focal spot. The propagation the finite width electron beam induce the return current in background electron. This return current may be induced with the time delay or not able to fully nullify the beam current due to low background density. In this case, there may be sheared flow between the plasma and the edge of the beam. Furthermore, the nonlinear stage of Weibel instability, the beam filaments merge into each-other and expel the return background plasma out of the beam. This separation leads to a sheared electron flow configuration. Keeping this in view, we carried out the numerical study of the instabilities associated with a 2-D sheared electron flow configuration against a neutralizing background of ions, in both weak and strong relativistic flow velocities regime, and have presented the details of such studies in Chapter 6.

Finally, in the last the Chapter 7, we summarize our findings and conclude our thesis work with the discussion of the possible future scope.

2

Description of Particle-In-Cell (PIC) algorithms

As mentioned in chapter 1, we have carried out simulation and theoretical studies on laser-matter interaction with specific emphasis on aspects such as efficient absorption of laser energy and the subsequent propagation of energetic electrons in the plasma. The Particle - In - Cell (PIC) code named PICPSI3D [2] has been suitably adapted for most of these studies. We have analyzed the simulation observations appropriately to draw inferences related to these phenomena. In this chapter, we provide a brief description of the PIC code.

2.1   Introduction

The experimental studies of complex phenomena are often very expensive and time consuming. Furthermore, in experiments, there is also the difficulty of not being able to span the entire range of parameter space. Neither it is possible to have control over various conditions to assess the underlying important mechanism at work. The analytical approach also has limitations wherein the solutions are possible only for oversimplified models. The computer simulation fills in this gap as it can provide observational data on complex processes over an extensive range of parameters which can then be suitably analyzed to extract an understanding of the essence of any phenomena.

In plasma physics, a technique known as Particle-In-Cell (PIC) is mostly used. Here particles are dynamically evolved in the external and self-consistent elec-

tromagnetic fields. Thus, it preserves the discrete particle nature in evolution. However, the evolution does not require the exact number of particles present in the system to be evolved. In fact, the simulation particles are considered as super-particles representing a collection of real particles, corresponding to similar charge by mass ratio and the same density as in the system. We provide a brief introduction and salient features of relativistic electromagnetic PIC simulation technique here.

2.2   Governing equations for relativistic electromagnetic system

The collection of charged particles in plasma can be described by the distribution function $f_s(\mathbf{r}, \mathbf{v}, t)$. Here s represents the plasma species and $\mathbf{r}$ and $\mathbf{v}$ are the position and velocity vectors of the particle respectively. The distribution function f_s gives the probability of finding the species "s" at time t at a position between $\mathbf{r}$ and $\mathbf{r} + d\mathbf{r}$ and having velocity between $\mathbf{v}$ and $\mathbf{v} + d\mathbf{v}$. The charged particles, in the plasma, interact with each other via external and self-consistent electromagnetic fields and through collisions. In the absence of collisions, we can describe the evolution of plasma particles by a coupled set of Maxwell-Vlasov equations. One can write the Vlasov equation for the evolution of the distribution function f_s as following,

$$\frac{\partial f_s}{\partial t} + \mathbf{v} \cdot \frac{\partial f_s}{\partial \mathbf{r}} + q_s \left(\mathbf{E} + \frac{\mathbf{v} \times \mathbf{B}}{c} \right) \frac{\partial f_s}{\partial \mathbf{p}} = 0, \qquad (2.1)$$

Here c is the speed of light and $\mathbf{p_s} = m_s \gamma_s \mathbf{v_s}$, m_s, q_s and γ_s are the momentum, rest mass, charge and the Lorentz factor of the species "s". The electric $\mathbf{E}$ and magnetic $\mathbf{B}$ fields in the Vlasov's equations evolve according to Maxwell's equations which

have been written below.

$$\nabla \cdot \mathbf{E} = 4\pi\rho, \tag{2.2}$$

$$\nabla \times \mathbf{B} = 0, \tag{2.3}$$

$$\nabla \times \mathbf{E} = -\frac{1}{c}\frac{\partial \mathbf{B}}{\partial t}, \tag{2.4}$$

$$\nabla \times \mathbf{B} = \frac{4\pi}{c}\mathbf{J} + \frac{1}{c}\frac{\partial \mathbf{E}}{\partial t}, \tag{2.5}$$

The charge density

$$\rho = \sum_s q_s \int f_s(t, r, p) d^3 p$$

and current density

$$\mathbf{J} = \sum_s q_s \int \mathbf{v_s} f_s(t, r, p) d^3 p$$

in Maxwell's equations have to be determined from the distribution function which obeys Vlasov's equation. It can thus be observed that the Vlasov equation(eq. (2.1)) is a complicated partial differential equation. It is coupled with the Maxwell's equations through charge and current density, thereby acquiring a highly non-linear form. In most cases, this complex non-linear structure of the equation make it difficult to find analytical solutions for this set. In such cases, one resorts to numerical techniques to solve eq.(2.1). The simple and straightforward numerical technique would be to discretize coupled Vlasov-Maxwell's equations in phase space. This method, however, requires a large number of computational grid (in both position and momentum space). This technique also looses its effectiveness when the distribution function is compact in momentum space and continues to remain so with time.

The other techniques of solving Vlasov-Maxwell's equation is to consider the evolution of discrete set of particles. In this case, thus a continuum distribution function in momentum and position space is replaced by the dynamical evolution of a discrete set of particles from which the continuum properties of charge and current densities are evaluated at the grid points by proper interpolation techniques. This is known as Particle-In-Cell (PIC) method.

The relationship between the distribution function and the position and mo-

mentum of the super-particles in the simulation can be expressed by the following relationship:

$$f_s(t, r, p) = \sum N_n S_r(r - r_n(t)) S_p(p - p_n(t)), \qquad (2.6)$$

where N_i is the number of physical particles that are represented by the nth computational particle. The functions S_r and S_p are the shape functions of computation particle in position and momentum space. The ensemble average of orbit of computation particles in phase space gives the solution of Vlasov equation. The orbit of computational super-particle in momentum and physical space is governed by the equation of motion of particles under Lorentz force as follows:

$$\frac{d\mathbf{r_n}}{dt} = \mathbf{v_n}, \qquad (2.7)$$

$$\frac{d\mathbf{p_n}}{dt} = q_n \left(\mathbf{E(t, r_n)} + \frac{\mathbf{v_n} \times \mathbf{B(t, r_n)}}{c} \right), \qquad (2.8)$$

Since the particle position and momentum can take continuum values, the Lorentz force needs to be evaluated at these points. The fields which are known at the location of grid points are interpolated at the location of the computational particle at every time step for the Lorentz force evaluation needed for solving eqs. (2.7,2.8). With the updated location and momentum of the particles the charge density and current densities are evaluated at grid points which are used for updating the fields at the next time step. This entire process runs in the time loop. The standard cycle of PIC simulation technique is summarized by Fig. 2.1. The interpolation of parameters from grid to particle location and vice versa would clearly depend on the shape of the computational particle. In the next section, we present a description of evaluating the weighting factors for interpolation from the shape of the computational particle.
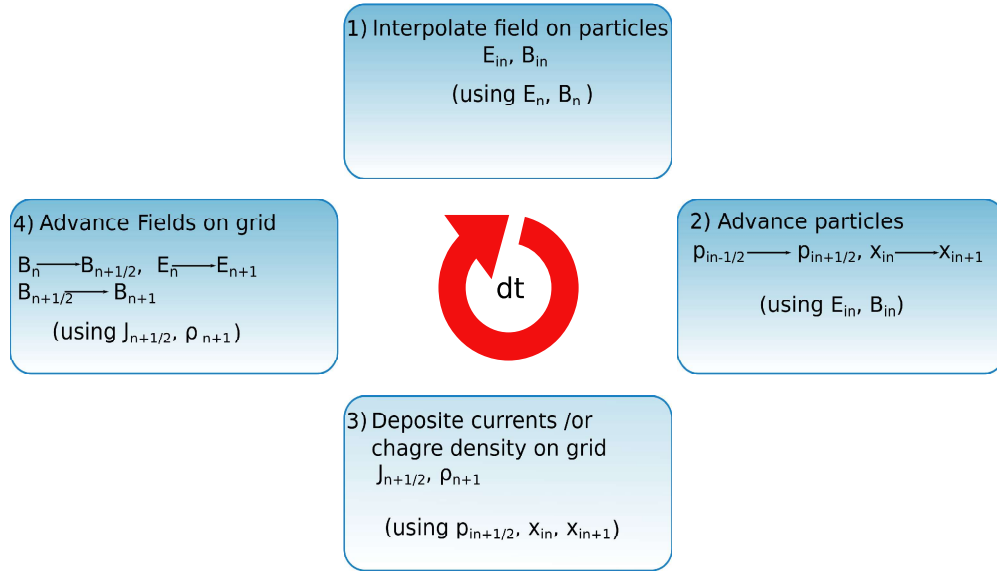
Figure 2.1: The standard cycle of PIC simulation

2.3 The shape of computational particle and the weighting factors

The standard PIC method uses the Dirac's delta function for momenta shape factor

$$S_p(p - p_i) = \delta(p - p_i) \tag{2.9}$$

On the other hand, the spatial shape factor depends on chosen b-splines function, b_l, which is defined as

$$b_l(x_i) = \int_{-\infty}^{\infty} dx' b_0(x_i - x') b_{l-1}(x') \tag{2.10}$$

where

$$b_0(\xi) = \begin{cases} 1, & \text{if } |\xi| \leq \frac{1}{2} \\ 0, & \text{otherwise} \end{cases}$$

The shape factor of super particle is defined as

$$S_i(x_i) = b_l\left(\frac{x - x_i}{\Delta_i}\right), \tag{2.11}$$

17

One can choose the shape factor of the computational particle to any order. Depending on shape factor, the charge, and current densities are assigned on the grid point and the fields are interpolated from the grid to particles. The choice of a higher order shape factor reduces the associated numerical noise of the system but it results in an increased computational cost. For low computation cost the zeroth order spline, known as Nearest Grid Point (NGP) weighting scheme, is used. We have used the first-order weighting for our studies which is known as Cloud In Cell (CIC) weighting. The zeroth and first order of b-spline are shown schematically in Fig. 2.2.
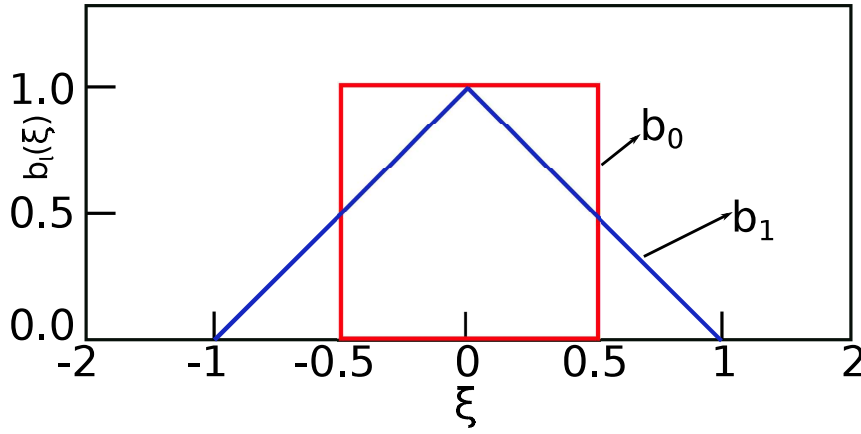
Figure 2.2: B-spline curve of various order

The first order b_1 is defined as

$$b_1 = \begin{cases} 1 - \frac{|x_p - x_i|}{\Delta x}, & \text{if } \frac{|x_p - x_i|}{\Delta x} \leq \frac{1}{2} \\ 0, & \text{otherwise} \end{cases}$$

In the simulation, the first order b-spline is realized by the following weighting factors in two-dimensional space, for the nth superparticle corresponding to the first order b-spline, are

$$W_j = j + 1 - \frac{y_n}{\Delta y}, \quad W_{j+1} = \frac{y_n}{\Delta y} - j,$$
$$W_k = k + 1 - \frac{z_n}{\Delta z}, \quad W_{k+1} = \frac{z_n}{\Delta z} - k, \qquad (2.12)$$

Where $j = \text{floor}(\frac{y_n}{\Delta y})$ and $k = \text{floor}(\frac{z_n}{\Delta z})$ where floor(n) means the largest integer

but less than n.

2.4   Spatial gridding and assignment of the physical variables with the time step chart

To solve the Maxwell's equations numerically, we use the Finite-Difference-Time-Domain (FDTD) method which is based on Yee's algorithm. The basic idea of this algorithm is to get the successive update of magnetic and electric field in time based on leap-frog method on staggered grid point of Yee's lattice as illustrated in Fig. 2.3. The staggered grid point is used to improve the numerical accuracy. We grid the
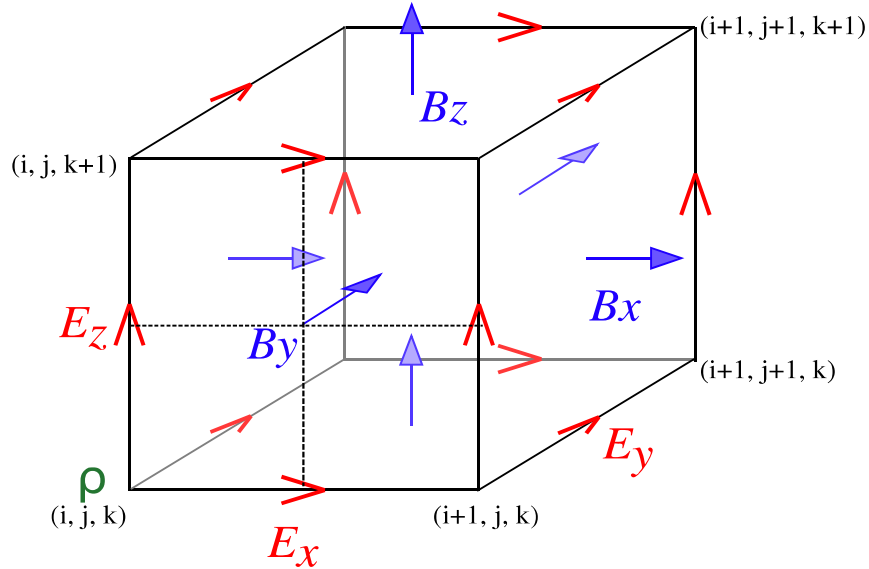
Figure 2.3: Grid assignment of the physical parameters of three-dimensional system

computation box in the integral multiples of grid spacing viz., Δx, Δy and Δz along x, y and z directions respectively. The indices i, j and k represent the ith, j^{th} and k^{th} multiple of the grid spacing in the three directions respectively. In addition, a shifted grid with half integral spacing is denoted by $i + 1/2, j + 1/2, k + 1/2$ indices.

The specification of various fields is carefully done depending on the kind of differential equation satisfied by them on appropriate grid points. For instance, the charge density ρ is specified at the full integer (i, j, k) grid points. The x component of electric field E_x is specified at (i+$\frac{1}{2}$, j, k). This is so because in the

Poisson's equation the x derivative of E_x is required. Since E_x is specified at the half integral grid along x, the central difference yields the derivative at the integral locations where the charge density is defined. Similarly, the $\hat{y}$ component of the electric field E_y is defined at (i, j+$\frac{1}{2}$, k) and $\hat{z}$ component of E_z is defined at (i, j, k+$\frac{1}{2}$) as their y and z differentiation appears in the Poisson's equation. Applying similar logic it can be shown that the electrostatic potential Φ should be assigned on full integer (i, j, k) grid points and current density components J_x, J_y, J_z should be assigned at the grid point similar to that of the electric fields components. The magnetic field components B_x, B_y, B_z require being assigned at (i, j+$\frac{1}{2}$, k+$\frac{1}{2}$), (i+$\frac{1}{2}$, j, k+$\frac{1}{2}$) and (i+$\frac{1}{2}$, j+$\frac{1}{2}$, k) respectively. For two-dimensional system, we put k=0. After the initialization of physical parameters at time t=0, we push back the velocity by time $t - \frac{\Delta t}{2}$. After that simulation is run in the time loop according to KEMPO1 [60] which is illustrated in Fig. 2.4
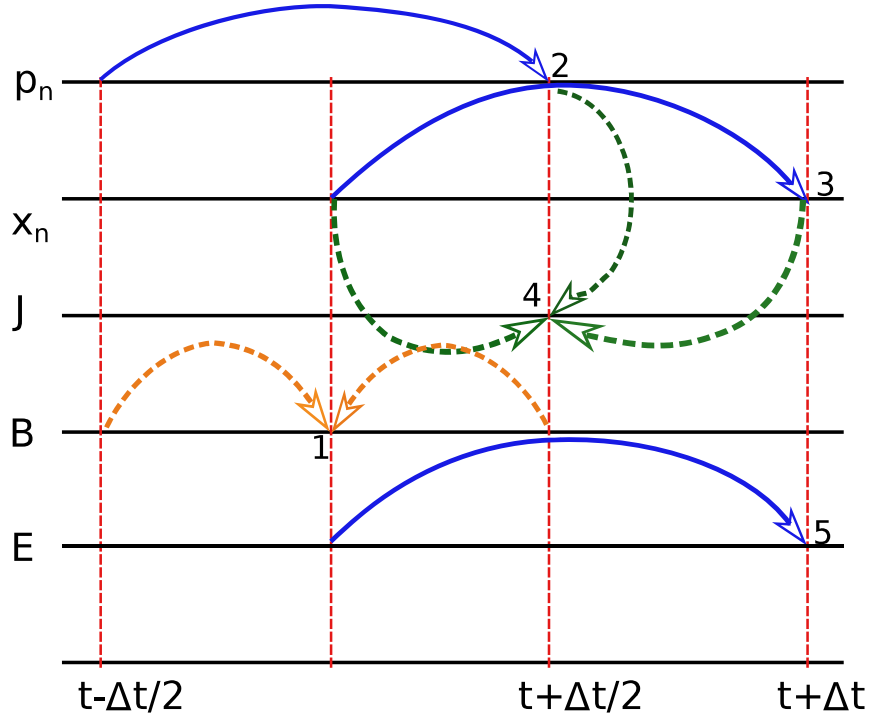
Figure 2.4: Time step chart used in the present PIC code: At initial time, we know x_n and E at time t, P_n and B at time t-Δt. 1. Compute B from $t - \frac{\Delta t}{2}$ to $t + \frac{\Delta t}{2}$ by using E at t and average it $\left(B = \left(B(t - \frac{\Delta t}{2}) + B(t + \frac{\Delta t}{2}) \right) / 2 \right)$ to get B at t.(dotted orange color) 2.compute p_n at time $t + \frac{\Delta t}{2}$(blue color) 3. Then, move particle's position x_n from t to $t + \Delta t$ (blue color) 4. The current density J is calculated at time $t + \frac{\Delta t}{2}$ by using $x_n(t - \frac{\Delta t}{2}, t + \frac{\Delta t}{2})$ and $p_n(t + \frac{\Delta t}{2})$ (dotted green color) 5. Finally calculate the electric field E at time $t + \Delta t$.(blue color)

2.5 Charge density

From the particle location obtained at each time step the charge density on the grid is assigned by using the weighting function defined by eq. (2.12).

$$\rho(j, k) = q_n W_j W_k, \qquad \rho(j, k + 1) = q_n W_j W_{k+1},$$
$$\rho(j + 1, k) = q_n W_{j+1} W_k, \quad \rho(j + 1, k + 1) = q_n W_{j+1} W_{k+1}, \qquad (2.13)$$

Where q_n is charge of nth super particle. The charge density ρ at each grid point is obtained from the superposition of contributions obtained by each superparticle.

2.6 Solution of Maxwell's equations

We now describe the solution of Maxwell's equation in the PIC simulation.

2.6.1 Poisson solver

The gradient of scalar potential ϕ gives the electrostatic electric field $\mathbf{E}$.

$$\mathbf{E} = -\nabla\phi \tag{2.14}$$

The two eq. 2.14 in eq. 2.2 gives the Poisson equation,

$$\nabla^2\phi = \frac{4\pi}{c}\rho \tag{2.15}$$

With the knowledge of charge density at each grid point this equation is solved by Successive Over Relaxation (SOR) numerical technique [61] to obtain scalar potential ϕ. This provides for the electrostatic part of the electric field.

2.6.2 The FDTD scheme

For the electromagnetic problem the Finite-Difference-Time-Domain (FDTD) numerical scheme is used for the evaluation of electric and magnetic fields in time through the Maxwell's equations (eq. (2.4), eq. (2.5)). We have in our studies employed only 2-D simulations with variations confined in the $y - z$ plane. No variations are considered along $\hat{x}$ which is taken as the direction of symmetry with $\frac{\partial}{\partial x} = 0$.

The electric and magnetic fields are then determined by the following procedure,

2.6.2.1 Electric field

We can rewrite the eq. (2.5) in the component form as follows:

$$\partial_t E_x = c\left(\partial_y B_z - \partial_z B_y\right) - 4\pi J_x, \tag{2.16}$$

$$\partial_t E_y = c\partial_z B_x - 4\pi J_y, \tag{2.17}$$

$$\partial_t E_z = -c\partial_y B_x - 4\pi J_z, \tag{2.18}$$

The eq. (2.16), eq. (2.17) and eq. (2.18) upon discretization in time and in space are written as

$$
E_{x,(j,k)}^{t+\Delta t} = E_{x,(j,k)}^{t} - 4\pi\Delta t J_{x,(j,k)}^{t+\Delta t/2}
$$
$$
+ c\Delta t \left(\frac{B_{z,(j+\frac{1}{2},k)}^{t+\Delta t/2} - B_{z,(j-\frac{1}{2},k)}^{t+\Delta t/2}}{\Delta y} - \frac{B_{y,(j,k+\frac{1}{2})}^{t+\Delta t/2} - B_{y,(j,k-\frac{1}{2})}^{t+\Delta t/2}}{\Delta z} \right), \tag{2.19}
$$

$$
E_{y,(j+\frac{1}{2},k)}^{t+\Delta t} = E_{y,(j+\frac{1}{2},k)}^{t} - 4\pi\Delta t J_{y,(j+\frac{1}{2},k)}^{t+\Delta t/2}
$$
$$
+ c\Delta t \left(\frac{B_{x,(j+\frac{1}{2},k+\frac{1}{2})}^{t+\Delta t/2} - B_{x,(j+\frac{1}{2},k-\frac{1}{2})}^{t+\Delta t/2}}{\Delta z} \right), \tag{2.20}
$$

$$
E_{z,(j,k+\frac{1}{2})}^{t+\Delta t} = E_{z,(j,k+\frac{1}{2})}^{t} - 4\pi\Delta t J_{z,(j,k+\frac{1}{2})}^{t+\Delta t/2}
$$
$$
+ c\Delta t \left(\frac{B_{x,(j-\frac{1}{2},k+\frac{1}{2})}^{t+\Delta t/2} - B_{x,(j+\frac{1}{2},k+\frac{1}{2})}^{t+\Delta t/2}}{\Delta y} \right), \tag{2.21}
$$

Here Δy and Δz are spatial step size along y and z directions respectively and Δt is the time step size.

2.6.2.2 Magnetic field

To compute the magnetic field, we rewrite eq. (2.4) in component form as follows:

$$\partial_t B_x = -c\left(\partial_y E_z - \partial_z E_y\right), \tag{2.22}$$

$$\partial_t B_y = -c\partial_z E_x, \tag{2.23}$$

$$\partial_t B_z = c\partial_y E_x, \tag{2.24}$$

Using the center difference scheme, we discrete the above eq. (2.22), eq. (2.23) and eq. (2.24) in space as well as time to obtain

$$
B_{x,(j+\frac{1}{2},k+\frac{1}{2})}^{t+\Delta t} = B_{x,(j+\frac{1}{2},k+\frac{1}{2})}^{t}
$$

$$
+c\Delta t \left(\frac{E_{y,(j+\frac{1}{2},k+1)}^{t+\Delta t/2} - E_{y,(j+\frac{1}{2},k)}^{t+\Delta t/2}}{\Delta z} - \frac{E_{z,(j+1,k+\frac{1}{2})}^{t+\Delta t/2} - E_{z,(j,k+\frac{1}{2})}^{t+\Delta t/2}}{\Delta y} \right) , \qquad (2.25)
$$

$$
B_{y,(j,k+\frac{1}{2})}^{t+\Delta t} = B_{y,(j,k+\frac{1}{2})}^{t} - c\Delta t \left(\frac{E_{x,(j,k+1)}^{t+\Delta t/2} - E_{x,(j,k)}^{t+\Delta t/2}}{\Delta z} \right) , \qquad (2.26)
$$

$$
B_{z,(j+\frac{1}{2},k)}^{t+\Delta t} = B_{z,(j+\frac{1}{2},k)}^{t} + c\Delta t \left(\frac{E_{x,(j+1,k)}^{t+\Delta t/2} - E_{x,(j,k)}^{t+\Delta t/2}}{\Delta y} \right) , \qquad (2.27)
$$

2.7 Equation of motion

2.7.1 Particle momentum

The difference form of momentum equation (eq. 2.8) for n^{th} superparticle can be written as

$$
\mathbf{p}_n^{t+\Delta t/2} = \mathbf{p}_n^{t-\Delta t/2} + \Delta t q_n \left(\mathbf{E}^t + \frac{\mathbf{p}_n^t \times \mathbf{B}^t}{m_n \gamma_n^t c} \right) , \qquad (2.28)
$$

Since we do not know the momenta p_n^t at time t, we rewrite the eq. (2.28) as

$$
\mathbf{p}_n^{t+\Delta t/2} = \mathbf{p}_n^{t-\Delta t/2} + \Delta t q_n \left(\mathbf{E}^t + \frac{(\mathbf{p}_n^{t+\Delta t/2} + \mathbf{p}_n^{t-\Delta t/2}) \times \mathbf{B}^t}{m_n \gamma_n^t c} \right) , \qquad (2.29)
$$

The electric and magnetic fields are interpolated from the grid to particle's positions by using the same weight factor which is defined by eq. (2.12). We use the Buneman-Boris method [62, 63] to solve this eq. (2.29). This method solves the eq. (2.29) in four step. The first half acceleration of particle by electric field is

written as

$$\mathbf{p}_n^- = \mathbf{p}_n^{t-\Delta t/2} + \frac{\Delta t}{2} q_n \left(\mathbf{E}^t \right),$$

(2.30)

Then two-step rotation in magnetic field

$$\mathbf{p}_n^{'} = \mathbf{p}_n^- + \mathbf{p}_n^- \times \mathbf{t},$$
$$\mathbf{p}_n^+ = \mathbf{p}_n^- + \mathbf{p}_n^{'} \times \mathbf{s},$$

(2.31)

where $\mathbf{t} = \frac{q\Delta t \mathbf{B}}{2\gamma^t}$ and $\mathbf{s} = \frac{2\mathbf{t}}{(1+\mathbf{t}^2)}$. Finally, again a half acceleration by electric field is provided to obtain the evolved momenta of the particle

$$\mathbf{p}_n^{t+\Delta t/2} = \mathbf{p}_n^+ + \frac{\Delta t}{2} q_n \left(\mathbf{E}^t \right),$$

(2.32)

The new particle positions are obtained by integrating the momenta (eq. 2.7)in time

$$\mathbf{r}_n^{t+\Delta t} = \mathbf{r}_n^t + \frac{\mathbf{p}_n^{t+\Delta t/2} \Delta t}{m_n \gamma_n^{t+\Delta t/2}},$$

(2.33)

(2.34)

2.8   Evaluation of current density on the grid

The particles move continuously and generate currents. This current should be deposited on the grid where the fields are defined as mentioned in earlier section. The simple area weighting scheme to deposit the currents on the grid does not satisfy the continuity equation. Therefore, we need the solution of Poisson equation at each time step to use correct the electric field in simulation. There are other schemes also which do not need to solve the Poisson's equation as these satisfy the continuity equation of charge flow. These schemes are known as "charge conservation scheme". One of them is "zigzag scheme" which is proposed by Umeda

et al. [64]. In all other schemes, the particle trajectory is assumed to be that of a straight line during one-time step. In reality, the particle would take any curved path depending on the kind of forces acting on it. Umeda realized it in computation by making the zigzag trajectory of the particle. We use this method in our code to compute the current density.

We assume that the point (y_1, z_1) belongs to the cell with coordinates (j_1, k_1) and (y_2, z_2) belongs to the cell with coordinates (j_2, k_2). A particle moves from a starting point ($y_1,\ z_1$) to point ($y_2,\ z_2$) in one-time step. We can decompose this movement of particle in a special pattern as shown in Fig. 2.5 and Fig. 2.6. Depending on particle movement only four cases are possible which are following:
(a)$j1 \neq j2;\ k1 \neq k2$ (b)$j1 = j2;\ k1 \neq k2$
(c)$j1 \neq j2;\ k1 = k2$ (d)$j1 = j2;\ k1 = k2$

(a) In this case ($j1 \neq j2$ and $k1 \neq k2$), the particle moves across two cell meshes one is along y direction and second one is along z direction. As shown in Fig. 2.5, the straight line trajectory of the particle cross the cell meshes two times. While in zigzag scheme, we assume that the movement of the particle from ($y1, z1$) to ($y2, z2$) is described as movements of two particles. One particle moves from ($y1, z1$) to (($j1 + 1)\Delta y, (k1 + 1)\Delta z) =(j2\Delta y, k2\Delta z)$, and another particle moves from ($j2\Delta y, k2\Delta z$) to ($y2, z2$) during the time from t to t + Δt. Therefore, the particle trajectory becomes a "zigzag" line. Since we compute only one cross-points of the particle trajectory and cell meshes, computation becomes much easier and faster.

(b) In case of $j1 = j2;\ k1 \neq k2$, the particle moves to one of the adjacent cells in the z direction. We assume here also the movement of two particles. one particle moves from ($y1, z1$) to ($\frac{y1+y2}{2}, (k1 + 1)\Delta z) = (\frac{y1+y2}{2}, k2\Delta z)$, and another particle moves from ($\frac{y1+y2}{2}, k2\Delta z$) to ($y2, z2$) during the time from t to t + Δt. The particle trajectory also becomes a zigzag line as shown in Fig. 2.6.

(c) When $j1 \neq j2;\ k1 = k2$, the particle moves to one of the adjacent cells in the y direction. Thus the particle trajectory becomes very similar to that in Case (b).

(d) When $j1 = j2$ and $k1 = k2$, the particle does not cross the cell meshes. However, we assume that the movement of a particle from ($y1, z1$) to ($y2, z2$) is described as movements of two particles. That is, one particle moves from ($y1, z1$) to ($\frac{y1+y2}{2}, \frac{z1+z2}{2}$) and another particle moves from ($\frac{y1+y2}{2}, \frac{z1+z2}{2}$) to ($y2, z2$) during

the time from t to t + Δt.
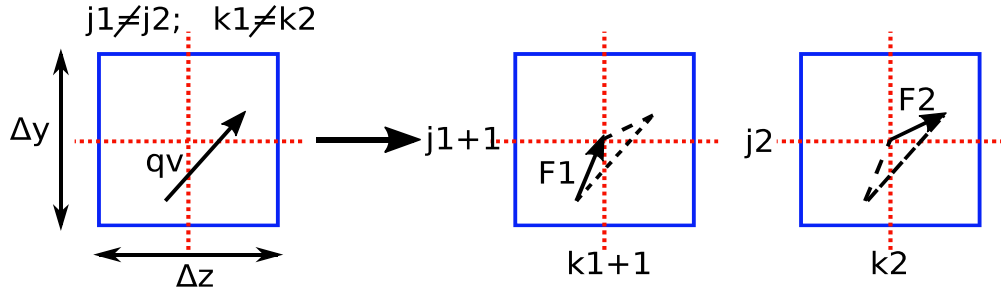
Figure 2.5: Particle trajectory of the two-dimensional zigzag scheme for $j1 \neq j2$ and $k1 \neq k2$ (case a). One particle moves from $(y1, z1)$ to $((j1 + 1)\Delta y, (k1 + 1)\Delta z) = (j2\Delta y, k2\Delta z)$, and another particle moves from $(j2\Delta y, k2\Delta z)$ to $(y2, z2)$ during the time from t to t $+\Delta t$. The solid arrows represent particle trajectories. The dashed red color lines represent cell meshes.
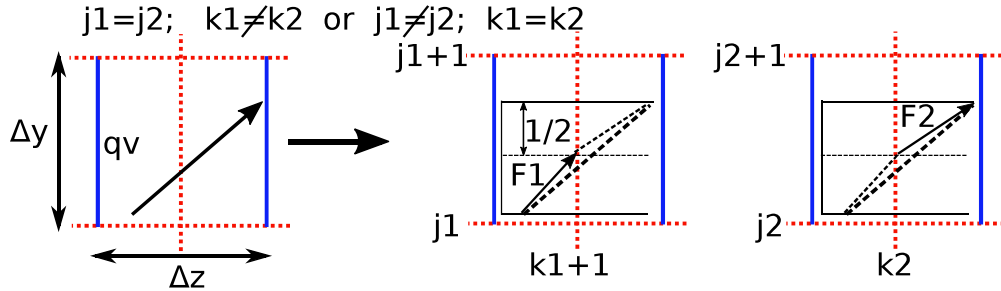
Figure 2.6: Particle trajectory of the two-dimensional zigzag scheme for $j1 = j2$, $k1 \neq k2$ (case b). One particle moves from $(y1, z1)$ to $(\frac{y1+y2}{2}, k2\Delta z)$, and another particle moves from $(\frac{y1+y2}{2}, k2\Delta z)$ to $(y2, z2)$ during the time from t to t + Δt. The solid arrows represent particle trajectories. The dashed red color lines represent cell meshes. By interchanging y and z, the case (b) is transformed into the case (c).

To realize all four cases as describe above in computation, we introduce a relay point (y_r, z_r) as proposed by Umeda and redefine the movement of the particle from (y_1, z_1) to (y_r, z_r) and another particle moves from (y_r, z_r) to (y_2, z_2) in Δt

time step. The relay point is defined as

$$y_r = min \left[min \left(j_1 \Delta y, j_2 \Delta y \right) + \Delta y, max \left(max \left(j_1 \Delta y, j_2 \Delta y \right), \frac{y_1 + y_2}{2} \right) \right] \quad (2.35)$$

$$z_r = min \left[min \left(k_1 \Delta z, k_2 \Delta z \right) + \Delta z, max \left(max \left(k_1 \Delta z, k_2 \Delta z \right), \frac{z_1 + z_2}{2} \right) \right] \quad (2.36)$$

By using (y_r, z_r), a charge flux $qv = q(vy, vz)$ is decomposed into $F1 = (Fy1, Fz1)$ and $F2 = (Fy2, Fz2)$ as follows:

$$F_{y1} = q_n \frac{y_r - y1}{\Delta t}, F_{y2} = q_n \frac{y_r - y2}{\Delta t},$$
$$F_{z1} = q_n \frac{z_r - z1}{\Delta t}, F_{z2} = q_n \frac{z_r - z2}{\Delta t}, \quad (2.37)$$

The weight factor for first-order shape function is given as follow:

$$W_{y1} = \frac{y_1 + y_r}{2\Delta y} - j1, W_{z1} = \frac{z_1 + z_r}{2\Delta z} - k1,$$
$$W_{y2} = \frac{y_1 + y_r}{2\Delta y} - j2, W_{z2} = \frac{z_1 + z_r}{2\Delta z} - k2, \quad (2.38)$$

The segments of the charge flux assigned to 8 grid points are obtained by the following procedure

$$J_y(j1 + \frac{1}{2}, k1) = \frac{1}{\Delta y \Delta z} F_{y1} \left(1 - W_{z1} \right), J_y(j1 + \frac{1}{2}, k1 + 1) = \frac{1}{\Delta y \Delta z} F_{y1} W_{z1},$$
$$J_y(j2 + \frac{1}{2}, k2) = \frac{1}{\Delta y \Delta z} F_{y2} \left(1 - W_{z2} \right), J_y(j2 + \frac{1}{2}, k2 + 1) = \frac{1}{\Delta y \Delta z} F_{y2} W_{z2}, (2.39)$$
$$J_z(j1, k1 + \frac{1}{2}) = \frac{1}{\Delta y \Delta z} F_{z1} \left(1 - W_{y1} \right), J_z(j1 + 1, k1 + \frac{1}{2}) = \frac{1}{\Delta y \Delta z} F_{z1} W_{y1},$$
$$J_z(j2, k2 + \frac{1}{2}) = \frac{1}{\Delta y \Delta z} F_{z2} \left(1 - W_{y2} \right), J_z(j2 + 1, k2 + \frac{1}{2}) = \frac{1}{\Delta y \Delta z} F_{z2} W_{y2},$$
$$(2.40)$$

The x-component of current density J_x is free from the charge continuity equation. Therefore, we compute J_x in two-dimension by apply the simple area-weighting scheme (2.12). The J_x assigned on grid points corresponding to their

indices are following:

$$J_x(j, k) = qv_x W_j W_k, J_x(j + 1, k) = qv_x W_{j+1} W_k,$$
$$J_x(j, k + 1) = qv_x W_j W_{k+1}, J_x(j + 1, k + 1) = qv_x W_{j+1} W_{k+1},$$

$$(2.41)$$

2.9   Summary

In this Chapter, we have provided a brief description of Particle-In-Cell simulation technique which has been adopted for our studies in this thesis.

3

Short-pulse intense laser interaction with overdense plasmas

The production of high energetic charge particles during the interactions between the intense, short pulse laser with overdense plasma and subsequently, its collimated propagation inside the target are important for many application such as fast ignition scheme of inertial confinement fusion (ICF) [1], generation of energetic charged particle beams [65–67], bright source of X-rays [68,69], generation of high-order harmonic [70] etc. Therefore, the basic understanding of absorption of laser radiation into overdense plasma and manipulation of the same by controlling the laser and plasma parameters are highly desired. In conventional, intense laser-solid interactions, the laser radiation are absorbed by collisionless processes viz vacuum heating [3], resonance absorption [33] and $\vec{J} \times \vec{B}$ heating [34] etc. However, for short femtosecond (fs) laser pulses and steep density profile of plasma, the laser radiation is absorbed by vacuum heating and $\vec{J} \times \vec{B}$ mechanism. In the case of vacuum heating, a p-polarized laser obliquely incident on a plasma surface has an electric field component normal to plasma surface. This normal component of electric field pulls the electrons into the vacuum during one half of the laser cycle and then returns them back into the target with a quiver velocity in next half laser cycle. However, at normal incidence, vacuum heating would be absent as there would be no component of the electric field vector normal to the plasma surface. The absorption process will then take place entirely through $\vec{J} \times \vec{B}$ mechanism. The absorption rate is typically small [71] for this case.

Recently, there have been indications that the laser absorption improves when

structured targets are employed. We explore this question with the help of PIC studies in this chapter.

3.1 Introduction

The amplification of ultrashort pulses to extremely high power levels became possible due to the introduction of chirped-pulse amplification technique (CPA). In a CPA laser system, an ultrashort tiny laser pulse is first stretched in time by a factor of 10^3 to 10^5 by means of a strongly dispersive element, the stretcher (e.g. a grating pair). The stretched pulse has sufficiently low power and is used for amplification in gain media. After the gain medium, the amplified pulse passes through a dispersive compressor, which removes the chirp and re-compresses the pulse in time.

Most of the energy of an intense short CPA laser pulse is concentrated in the main pulse. However, a short laser pulse generated by chirped pulse amplification (CPA) technique is inevitably accompanied by a long pre-pulse typically of the order of $\sim$ ns of amplified spontaneous emission (ASE) [72,73]. The ASE pulse comes from the amplifier chain. The intensity contrast ratio which is a ratio of the intensity of main peak pulse to ASE pre-pulse is typical of the order of 10^{-6}. Thus even for a short laser pulse at moderate intensity $10^{18}W/cm^2$, the ASE pulse alone would have an intensity corresponding to $10^{13}W/cm^2$ which is sufficient to create a pre-plasma in laser-solid interaction, for the main pulse. A number of techniques have been proposed to clean away pre-pulses [74,75] but, most of these techniques are still in developmental stage.

The intensity of laser pre-pulse is lower than $10^{15}W/cm^2$, therefore the pre-pulse energy transfers its electromagnetic energy to pre-plasma by collisional processes. The electrons of pre-plasma start to expand toward vacuum with thermal energy and generate the space charge related electric field. The ions follow the electrons to maintain the quasineutrality. The simplest model to describe a freely expanding plasma is the isothermal model [76,77]. In this model, it is assumed that plasma maintains the constant temperature by transferring the electromagnetic energy of pre-pulse to electrons, and electrons utilize it to accelerate ions. At temporal scale of pre-pulse, the electrons, and ions in pre-plasma have sufficient time to achieve

the thermal equilibrium. According to isothermal expansion model, pre-plasma results in an exponential plasma density profile on the target surface with the characteristic length L $= c_s$ t , where $c_s = \sqrt{\frac{ZT_e}{m_i}}$ is the ion sound speed, Z is ion charge, m_i is ion mass, T_e is electron temperature, and t is the expansion time.

Thus, when a short pulse high intensity laser interacts with a solid target, which is already ionized and in the form of a plasma when the main pulse interacts with it. In the case of structured targets, it is interesting as the plasma that gets formed before the arrival of the main pulse has the inhomogeneity of the target structure embedded in its spatial profile. Plasma expansion being limited by the acoustic speed, this preformed plasma does not get sufficient time for expansion before the arrival of the main pulse. Thus the main pulse gets to see an overdense inhomogeneous plasma profile.

For our numerical study, we consider the interaction of the main laser pulse with both homogeneous and inhomogeneous plasma targets and show conclusively that in the latter case the heating /absorption is considerably increased. It is shown that a novel vacuum heating mechanism is operative in the case of the rippled targets which is responsible for this enhancement.

3.2 Simulations of the interaction of laser with overdense plasma

The simulation set up has been shown in Fig. 3.1(a). We choose the right-handed rectangular 2-D simulation box depicting the $Y \times Z$ plane as shown in Fig. 3.1(a). A Gaussian laser beam with FWHM(full-width half maximum) of 3μm and an intensity of $1 \times 10^{19} W/cm^2$ enters from the left boundary and propagates in the Z-direction as depicted by the propagation vector k in Fig. 3.1(a) for the normal incidence. Uniform plasma has been depicted by the orange shaded region in Fig. 3.1(a). The left and right unshaded regions correspond to vacuum. The laser field is p-polarized with the electric field in the Y-direction and the magnetic field in the "-ve" X-direction. The laser beam has top-hat temporal profile of 30 femtoseconds (fs) and interacts with plasma at normal incidence. In the simulation geometry, the size of plasma slab (shown by orange color shaded region) has been chosen to be $6\lambda_L$ in the transverse direction and $9\lambda_L$ in the longitudinal direction
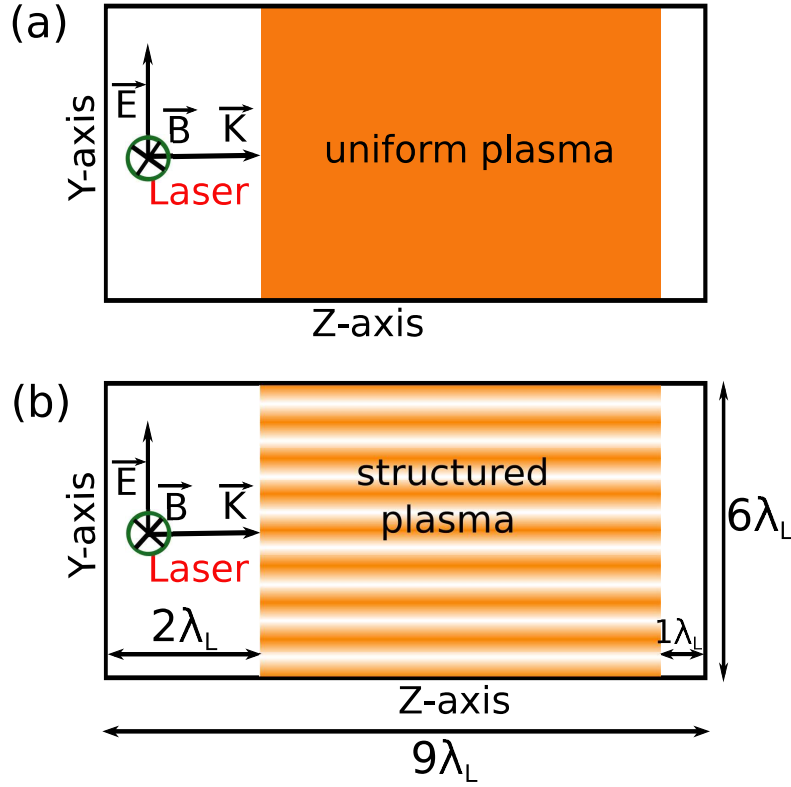
Figure 3.1: 2D PIC simulation setup: (a)p-polarized laser is irradiated on uniform plasma target (b)p-polarized laser is irradiated on structured plasma target

where $\lambda_L = 1\mu m$ is the laser wavelength. There is a vacuum region of $2\lambda_L$ in front of plasma slab and $1\lambda_L$ behind the plasma slab. The absorbing boundary conditions have been used for field, and reflecting boundary conditions have been used for particles.

The conventional laser-plasma interaction with uniform plasma targets assumes a plasma density $n_0 = 10n_c$, where n_c is critical density. The second set of simulations are performed on corrugated plasma targets (representing embedded nanowires on a flat surface) with plasma density of the form of $n_{0i}(y) = n_{0e}(y) = n_0[1 + \varepsilon cos(k_s y)]$. Thus there is a variation in plasma density along y transverse to the laser propagation direction. The schematic diagram of simulation set up for this case in shown in Fig. 3.1(b). Here, n_{0i} is ion density, n_{0e} is electron density in plasma. The wave number k_s for the plasma density variation is $2\pi m/l_s$; where l_s is scale length of inhomogeneity and ε is the amplitude of density variation. The

mesh size is chosen to be fine as $\delta z = \delta y = 0.02c/\omega_p$ to resolve the density scale length. Here $\omega_p = \sqrt{4\pi n_0^2 e/m_e}$ is plasma frequency, m_e is rest mass of the electron, e is the electric charge, and $c/\omega_p = d_e = 5 \times 10^{-6} cm$ is electron skin depth. The ions, having charge and mass of the proton, are kept in rest during simulation. We use 4 particles per cell for each species (electron and proton).

As laser interacts with uniform plasma, the plasma surface gets modified by ponderomotive force. The ponderomotive force expels the electrons from higher laser intensity to lower intensity. The depletion of electrons from high intensity region forms a cavity. The formation of cavity in laser-plasma interaction can be seen in Fig. 3.2(b) (zoomed image of Fig. 3.2(a)) at time $t = 30.70$ fs where laser interacts with uniform plasma density. In conventional vacuum heating mechanism
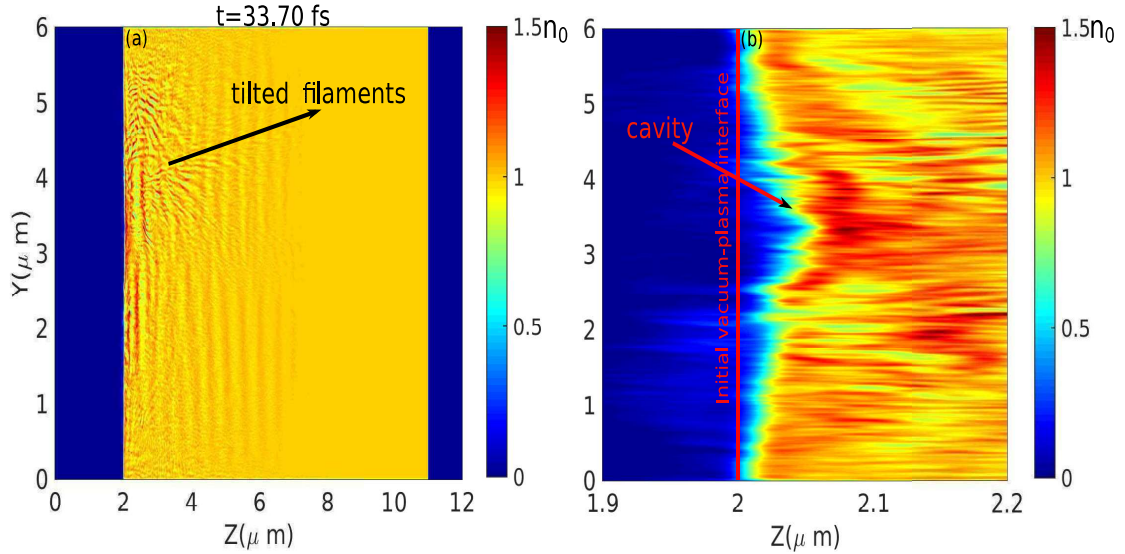
Figure 3.2: The electron density [in unit of n_0] for uniform plasma density target at time $t = 33.70$ fs: (a) The observation of tilted filaments in electron density as fast electrons propagate inside the target (highlighted by arrow) (b)Formation of cavity due to evacuation of electrons from high-intensity region to low intensity region (highlighted by arrow).

the laser electric field draws the electrons from the target in the vacuum during the half laser cycle. This requires that a laser electric field component normal to the target surface be present. The schematic diagram of conventional vacuum heating mechanism is shown in Fig. 3.3. For a p-polarized normal incident laser

there is no component of laser electric field normal to the surface. Thus, in this case, the conventional vacuum heating can not occur. The longitudinal phase
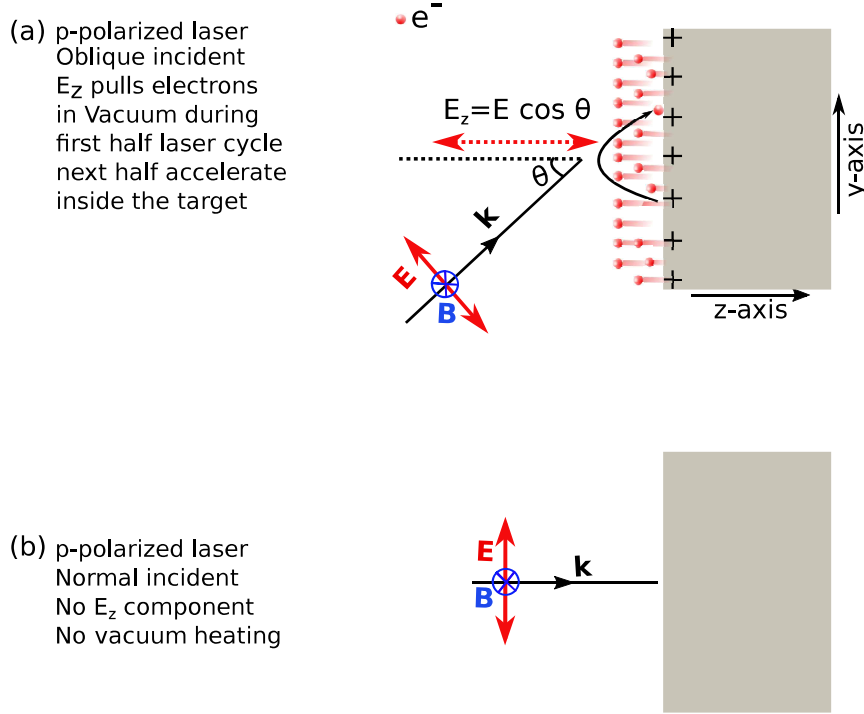
Figure 3.3: Sketch of conventional vacuum heating mechanism:(a) In oblique incidence, the electric field component, normal to plasma surface, pulls the electron in the vacuum in first half laser cycle and accelerates back into plasma target in next half laser cycle (b) In normal incidence, there is no electric field normal to plasma surface. Therefore, there is no vacuum heating (Brunel's mechanism).

space projection of electron phase space in Fig. 3.4 shows some energetic electron generating occurring in this case also. It appears that the $\vec{J} \times \vec{B}$ forces acting normal to the plasma surface are responsible for this energetic electron generation as they can even in this configuration accelerate the electrons inside the target. It is also likely that the dimpled cavity surface, created by the laser ponderomotive pressure, having modified the direction of surface normal now has laser electric field component normal to itself. This electric field can then contribute to the particle acceleration. This can be verified by purposely generation surface corrugations in the target, the surface normal of which would have an electric field component of similarly incident laser beam.
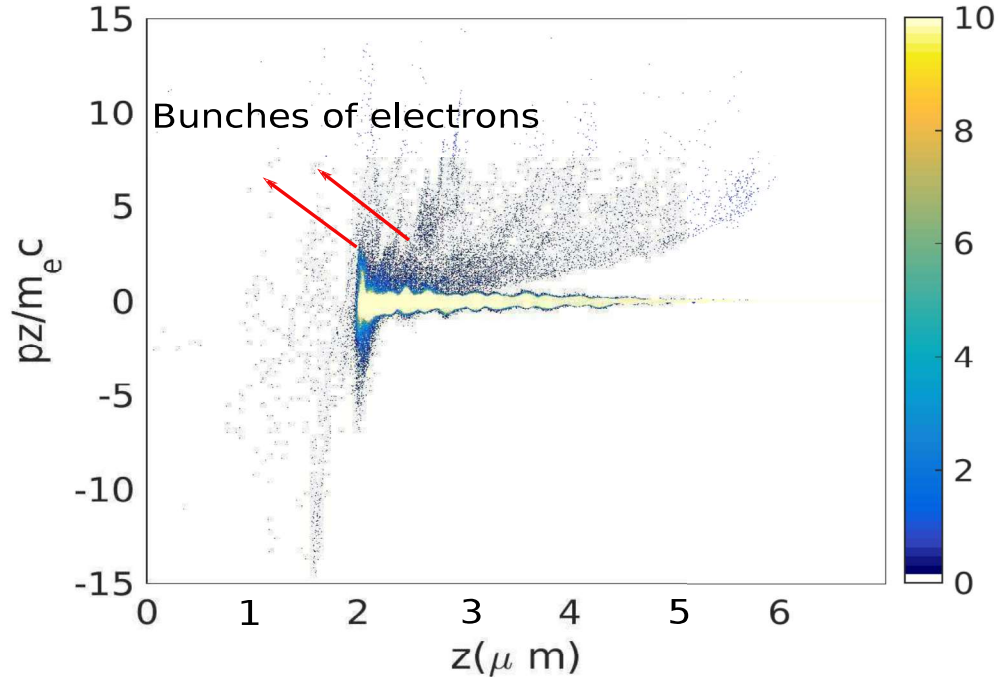
Figure 3.4: Phase-space projection of electronic distribution of longitudinal momentum along laser propagation direction for the uniform target at time $t = 26.48$ fs: the appearance of electron bunches are highlighted by arrows.

We, therefore, choose a target surface of the form shown in Fig. 3.1(b), which can essentially form as a result of nanowires embedded on the surface of a flat target. These nanowires, when exposed to the prepulse, generate a plasma profile of similar form. In the simulations, we have exposed this particular target profile again to the similar p-polarised laser propagating along Z direction.

In this case too, the front surface gets dimpled in a similar fashion (See Fig. 3.5) as that of Fig. 3.2(b). However, the density grooves due to nanostructuring can be clearly seen to persist. The phase space plot of Fig. 3.6, in this case, shows a much higher gain in electron energy compared to planar targets shown in Fig. 3.4, as the z component of electron momentum is considerably larger for many particles in this plot. In the case of corrugated target, the laser electric field component normal to the corrugations can draw the electron out of the surface as shown in the schematic drawing of Fig. 3.7. This leads to the mechanism of vacuum heating being operative. It should also be noted that the surface corrugations not only
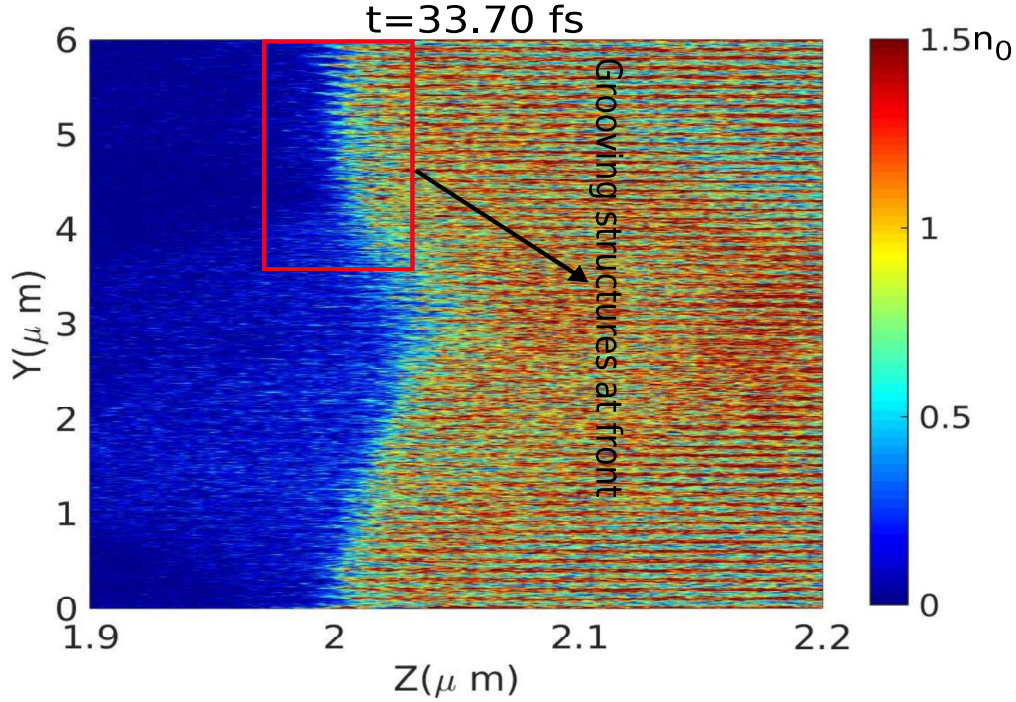
Figure 3.5: The electron density [in unit of n_0] for rippled case ($\varepsilon = 0.5$, $k_s = \pi$) at time $t = 33.70$ fs: the appearance of grooving structures at vacuum-plasma interface (highlighted by box).

lead to a geometry where the laser electric field is normal to the surface, it also enhances the overall surface area from which the electrons can get extracted. Thus the laser energy absorption in the case of corrugated targets gets amply enhanced. The spectral power in the Z component of the electric field in k_y-k_z plane in the system has been shown in Fig. 3.8. It shows that the maximum power appears at ripple scale length $k_s = \pi$ chosen for this particular case.

We use the definition of determining the absorption rate provided by Ren *et al.* [78] as the ratio of the electron kinetic energy gained to incoming laser power as follows:

$$\xi(t) = [KE(t+ \triangle t) - KE(t)]/(P_L \triangle t) \tag{3.1}$$

here P_L is the power of the incident laser pulse. We considered various inhomogeneity scale lengths and amplitude of the plasma density profile and estimated the absorption rate as the function of time. This has been shown in Fig. 3.9. This
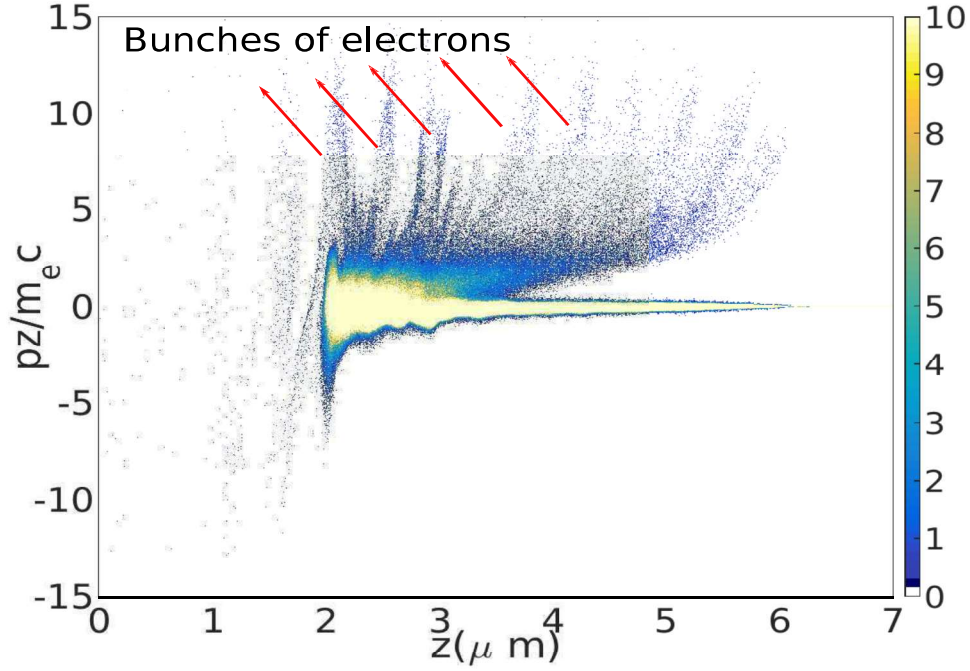
Figure 3.6: Phase-space projection of electronic distribution of longitudinal momentum along laser propagation direction for for ripple target ($\varepsilon = 0.5$, $k_s = \pi$) at time $t = 26.48$ fs: the appearance of electron bunches are highlighted by arrows.

figure clearly shows that the absorption is high only for some intermediate value of the inhomogeneity scale length. For both planar targets as well as when the scale length is much sharper than the skin depth, the absorption is almost comparable. However, at an intermediate value of the inhomogeneity scale the absorption seems to maximize. This can be understood by realising that one requires a certain vacuum/ low density space in between the corrugated high density plasma in which the electrons get sufficient time to be dragged. If this spacing is less there is overlapping between two high density regions and the vacuum heating mechanism is not applicable. It should also be noted from the figure that there is a amplitude dependence also in the absorption rate. A high amplitude of inhomogeneity seems to do better for absorption.

Fig. 3.9 shows that laser absorption rate increases with time for all parameters.

(a) P-polarized laser
   oblique incident
   E_z & E_y **both pulls**
   electrons in Vacuum
   during first half cycle
   next half accelerate
   inside the target

$E_y = E \sin \theta$

$E_z = E \cos \theta$

θ

k

E

B

(b) P-polarized laser
   Normal incident
   E_y **pulls electrons into**
   gap between the wires
   during first half laser cycle
   next half accelerate inside
   the target

$E_y = E$

E

B

k
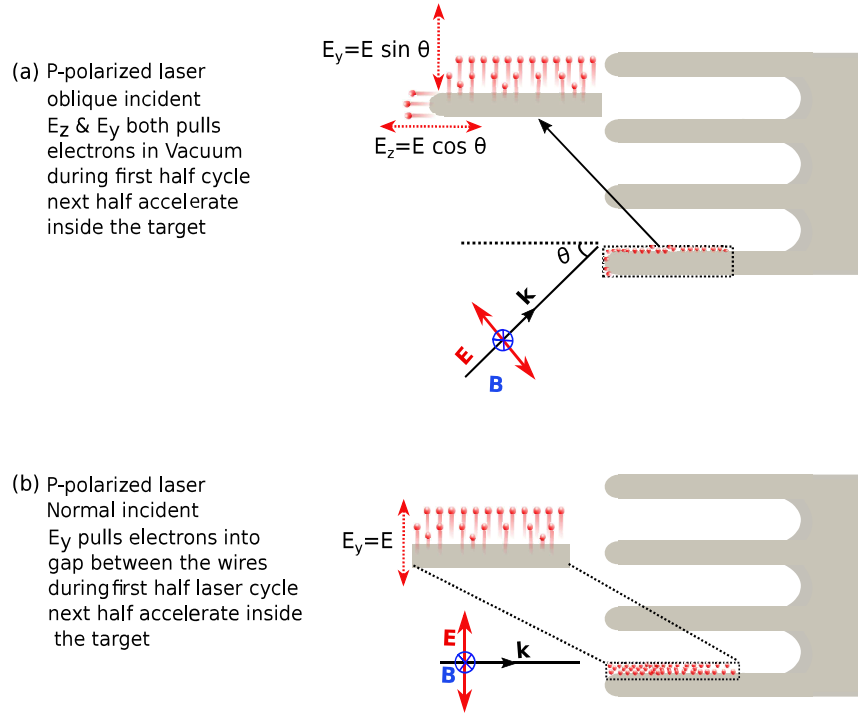
Figure 3.7: Sketch of vacuum heating mechanism in structured nano-wire target:(a) In oblique incidence, the E_z component of electric field is normal to front surface of plasma and E_y component of electric field is normal to the side surface of plasma. Both components satisfy the vacuum heating conditions. Therefore the absorption of laser radiation increases for structure target. (b) Even if in normal incidence case, there is electric field normal to side plasma surface which satisfies the vacuum heating condition and increases the absorption of laser radiation compare to conventional vacuum heating (Brunel's mechanism).
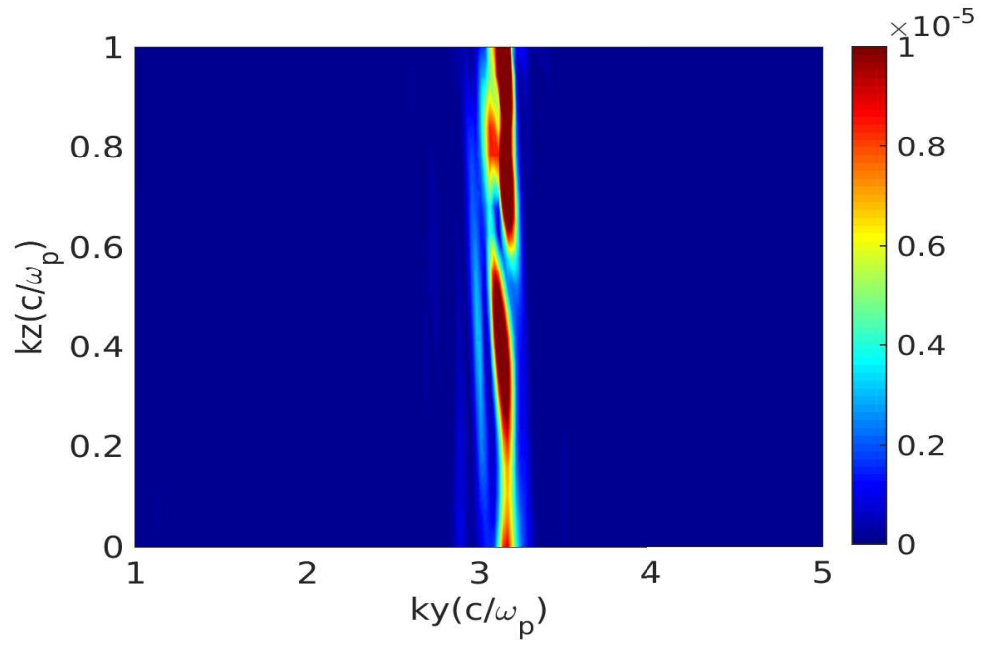
Figure 3.8: Two-dimensional fast Fourier transform (FFT) of Z-component of electric field energy E_z^2 [in units of $(m_e c \omega_p / e)^2$] for ripple parameters $\varepsilon = 0.5$, $k_s = \pi$: the maximum power appears at ripple wave number $k = \pi$.
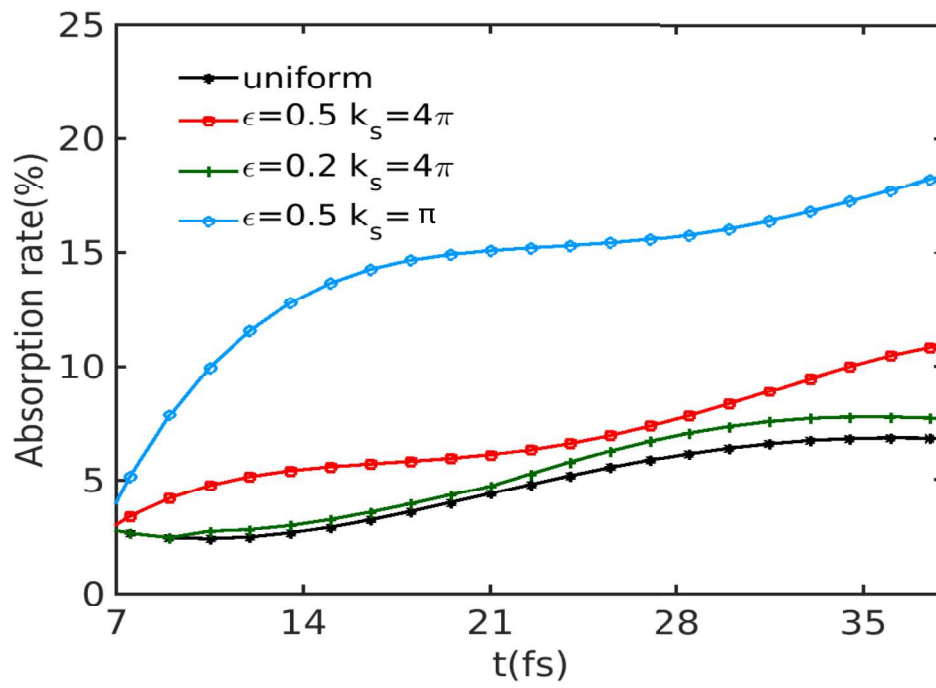
Figure 3.9: Fraction of laser energy absorbed by the electrons for various parameters of ripple.

3.3 Propagation of laser generated fast electrons inside the overdense plasma

The energetic electrons generated by the lasers are important as they have extracted energy from the laser which otherwise is unable to transport energy in the overdense region of the plasma. The question that is of importance now is how well to transport these energetic electrons in any desired plasma region.

The typical magnitude of electron currents generated by laser pulses with an intensity similar to $\sim 10^{18}W/cm^2$ is of the order of $\sim MAmps$. In the vacuum, the electron trajectories carrying this current would turn due to the self-generated magnetic field. Thus the maximum current that an electron beam can carry in the vacuum is given by the Alfvén current limit, which is $17\gamma v_e/c$ kAmps, where γ is the Lorentz factor. In the presence of plasma, the charge imbalance generated by the beam propagation causes the background plasma electrons to respond by generating current in the reverse direction. Thus a spatially overlapping current in the reverse direction flows which essentially annihilates the magnetic field of the beam current. The absence of the magnetic field then leads to an unhindered propagation of the fast electron in the plasma even though the beam current exceeds the Alfvén current limit. This scenario is, however, not stable. A small imbalance or perturbation in spatially overlapping forward and return current induces oscillating magnetic field in the transverse direction at short wavelengths ($\sim$ order of skin depth) through the mechanism of Weibel instability. The longitudinal two stream instability is also present in such a configuration. In fact, the oblique mode with the wave vector tilted to the current propagation direction is found to have a maximal growth rate. The Weibel instability spatially separates the beam and background electron currents into a large number of small-scale current filaments. As time progresses the like current filaments attract and coalesce with each other to form broader filaments. This leads to the generation and the growth of magnetic fields ultimately. The magnetic field then adversely influences the propagation of the beam current in the plasma.

The scenario described above has been observed in our present simulations. The observations for the planar target has been shown in Fig 3.10 where we have plotted the total current density produced by laser generated fast electrons propagation

as well as the induced background electron current at a time of $t = 33.70$ fs. The
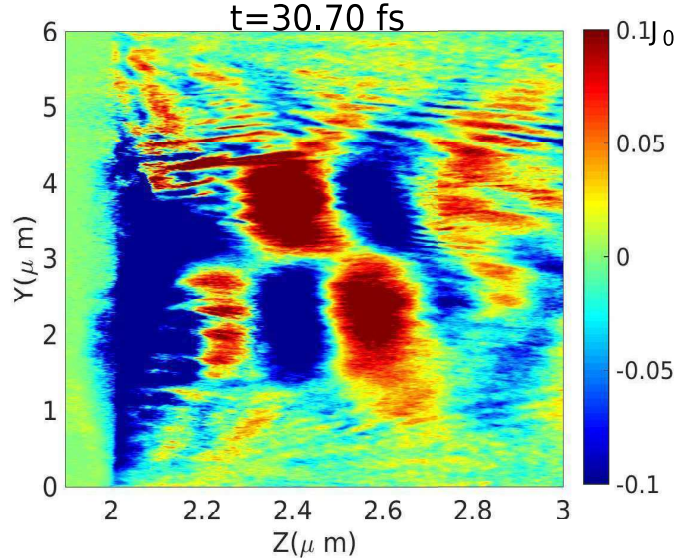
Figure 3.10: Current density J_z [in unit of $j_0 = n_0 ec$] at time $t = 33.70$ fs: for uniform plasma density target which shows the filamentation in current density due to Weibel instability.

oblique nature of the instability is clearly evident. Furthermore, the transverse scale length is typically much smaller, typically of the order of the electron skin depth as expected for the Weibel mode. The generation of the magnetic field can be clearly observed in Fig. 3.11 at time $t = 33.70$ fs. The magnetic fields are typically of the order of Mega Gauss. In simulations with the structured targets, we have observed the weaker development of the instability. It appears, therefore, even for the propagation of energetic electron beam through plasma the structured targets are better. In these simulations for the same laser intensity, since the electron energy for the structured target is higher compared to planar targets, a comparison of the two can not be made to conclude that the structured targets are better for electron propagation.

In the next chapters we, therefore, choose spatially overlapping electron current configurations with similar energies (depicting the forward and reverse shielding currents) both for the planar and structured targets. A comparison of the development of various instabilities have been provided for the two cases to discern the role played by the structured targets on the development of the beam-plasma
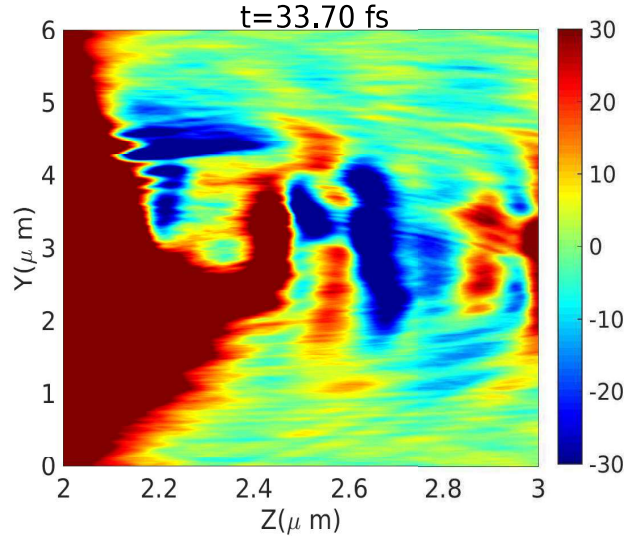
Figure 3.11: Magnetic field B_x [in unit of Mega gauss] at time $t = 33.70$ fs: for uniform plasma case, Figure shows the Weibel generated magnetic field structures with transverse scale of order of$\sim 2c/\omega_p$.

related instabilities.

It should be noted that studies with some simplified fluid models (Generalised Electron Magnetohydrodynamic (G-EMHD) model) have shown that better guided propagation of electron current is possible in the presence of density inhomogeneities [79, 80]. Some studies have also shown that targets with different materials producing tailored resistivity gradients can be helpful in maneuvering the electron current pulse through plasmas [81]. Here, in the subsequent chapters, we will illustrate the role of density inhomogeneity through PIC simulations on the propagation of energetic electrons through plasma.

3.4 Summary

In this chapter, we have carried out the 2D PIC simulations of the short pulse intense laser interaction with plasma. Both planar and rippled overdense pre-ionized plasma targets have been considered for the simulations. Such a configuration would arise when the prepulse of the intense laser would ionize a structured target (for instance nanowires embedded on a flat surface). Our simulations have

demonstrated that the structured targets are better suited for the laser energy absorption. This is understood by realising that the structured targets have an extended surface area. Furthermore, the surface normal is directed in different directions. Thus even for a normal incident p - polarised laser some portion of the surface would have laser electric field directed along the surface normal resulting in vacuum heating which otherwise is not permitted in a planar target.

In subsequent chapters, we will explore the role of inhomogeneous plasma density on the propagation of the energetic electrons through the plasma.

4

Beam-plasma system in one-dimensional geometry

In the previous chapter, we considered the interaction of laser field with overdense plasma medium which illustrated the absorption of laser light by the medium and the generation of energetic electrons. These energetic electrons move inside the plasma like a charged beam. The beam dynamics inside plasma is of interest and we focus upon this issue in considerable detail in this as well as subsequent chapters.

In this chapter, we consider the simplified case of beam plasma system with 1-D space variations orthogonal to the beam propagation direction. In this case, the beam-plasma system is susceptible to the filamentation or beam-Weibel instability which is detrimental to the beam transport through the plasma. We show that the presence of a rippled plasma density suppresses the instability. A detailed study of the influence of beam parameters and inhomogeneity scale length on the instability is performed. Theoretical descriptions of the observations are also provided.

4.1 Introduction

The propagation of relativistic electron beams (REB) generated through the interaction of a high power laser (I$\geq 10^{18}$W$/cm^2$) with a solid target, induces return currents in the background plasma. These return currents, ensure the propagation of high beam currents in the plasma. In vacuum currents exceeding the Alfven limit of $I = (mc^3/e)(v_b/c)\gamma_b = 17\gamma_b v_b/c$ kA, (m is the electron mass, e is the

electronic charge, v_b is beam velocity, c is the speed of light and γ_b is the Lorentz factor of the beam) is not permitted, as the self magnetic field of the high current are sufficient to turn the trajectory of the electrons completely. However, in the plasmas, a spatially overlapping return shielding current by the background electrons inhibits the magnetic field generation and permits the propagation of beams with such high forward beam currents. The combination of the forward and return currents in plasmas are, however, susceptible to several instabilities viz., two-stream [41], beam-Weibel [4]/filamentation [5] and oblique modes [42]. For relativistic flow, the beam-Weibel instability dominates over two-stream instability. Therefore, we do not study two-stream instability in the relativistic regime, and work only on beam-Weibel instability in this chapter by considering a 1-D space variation orthogonal to the beam propagation direction. The beam-Weibel instability generates a magnetic field in the unmagnetized plasma system [82]. This instability has a detrimental influence on the propagation of the relativistic energy electron beam through a plasma and hence puts practical constraints on the usage of the beam electrons deep in the plasma region. In order to suitably utilize the relativistic electron beams these constraints on the propagation of beam through a plasma needs to be overcome. A lot of experimental, theoretical and simulation work has been devoted to control and suppress this instability [83–85]. The effect of parameters such as beam density [86], beam velocity [86], transverse temperature [87], collisions [26] etc., on this instability has been extensively studied.

A recent experimental [24] result, has shown many fold improvement in the propagation of a hot relativistic electron beam through an array of carbon nanotubes (CNTs). An explanation of this has been put forth by Mishra *et al.* [56] suggesting that the inhomogeneous plasma created by the ionization of the CNTs by the front of the beam is responsible for the stabilization of transverse instabilities, thereby aiding the collimated propagation of the beam through longer distances compared to a homogeneous plasma. Our PIC simulations have been carried out for the system similar to that studied by Mishra *et al.* analytically by fluid theory.

This chapter has been organized as follows. Section II contains the details of the model configuration and governing equations. In section III, the analytical results are presented. The details of PIC simulations are given in section IV. The observation of results from PIC simulation are presented in section V and it's

interpretation are given in sec. VI. In the last sec. VII, we summarize our results.

4.2   Model configuration and governing equations

We consider a neutral, unmagnetized, collision-less, inhomogeneous beam-plasma system and we derive the general equation to study the linear response of the system in framework of two-fluid model wherein the fast electron beam and the background electrons are treated as separate fluids. In this framework, we assume that one species of counter-streaming plasma (fast electron beam) is moving in +z direction with drift velocity v_{0b}, density n_{0b} and temperature T_{0b}. Second species (returning background electron) is moving in -z direction with drift velocity v_{0p}, density n_{0p} and temperature T_{0p}. The ions are heavier than electrons, therefore they do not respond at electron time scale. Keeping this in view, we consider the static background of ions to provides only the neutrality in system. The inhomogeneity in plasma density is introduced, transverse to beam propagation, along the Y-axis. The dynamical evolution this system can typically be understood by the help of continuity and momentum equations coupled with the Maxwell's equation. The considered system can be described by following set of dimensionless governing equations:

$$\frac{\partial n_\alpha}{\partial t} + \nabla \cdot (n_\alpha \vec{v_\alpha}) = 0 \tag{4.1}$$

$$\frac{\partial \vec{p_\alpha}}{\partial t} + \vec{v_\alpha} \cdot \nabla \vec{p_\alpha} = -\left(\vec{E} + \vec{v_\alpha} \times \vec{B} \right) - \frac{\nabla P_\alpha}{n_\alpha} \tag{4.2}$$

$$\frac{\partial \vec{B}}{\partial t} = -\nabla \times \vec{E} \tag{4.3}$$

$$\frac{\partial \vec{E}}{\partial t} = \nabla \times \vec{B} - \Sigma_\alpha \vec{J_\alpha} \tag{4.4}$$

where momentum vector $\vec{p_\alpha} = \gamma_\alpha \vec{v_\alpha}$, and Lorentz factor $\gamma_\alpha = (1 + p_\alpha^2/m_e^2 c^2)^{1/2}$. The current density is defined as $\vec{J_\alpha} = -n_\alpha \vec{v_\alpha}$. The pressure P_α is provided by the equation of state. In the above equations, velocity is normalized by the speed of light c, density by n_0 (the spatially average ion density), frequency by $\omega_0 = \sqrt{4\pi n_0^2 e/m_e}$, length by electron skin depth $d_e = c/\omega_0$ and electric and magnetic field by $E_0 = B_0 = m_e c \omega_0/e$ where m_e is rest mass of electron and e is the electronic

charge. The subscript α is $'b'$ for beam and $'p'$ for plasma.

In the equilibrium, there is no electric and magnetic field in the system. It means that there is complete charge as well as current neutralization. In system, charge neutralization is achieved by imposing the quasi-neutral condition, and the current neutralization is achieved by balancing the forward and return electron currents at each spatial location. For simplicity of treatment, we choose the profile of transverse temperature T_α in such a way that gradient of pressure is zero in equilibrium. Generally, the electron beam, generated in laser-solid interaction, has the much lower temperature in propagation direction compare to transverse. Therefore, we chose the temperature parallel to beam propagation direction to be negligible. Thus, for an inhomogeneous case considered by us, we have the following conditions for equilibrium:

$$n_{0i}(y) = n_{0b}(y) + n_{0p}(y) \tag{4.5}$$

$$\Sigma_\alpha n_{0\alpha}(y)\vec{v_{0\alpha}} = 0 \tag{4.6}$$

In equilibrium, beam pressure P_{0b} is chosen to be independent of y. This is achieved by choosing the beam temperature $T_{0b}(y)$ to be satisfying the following condition

$$P_{0b} = T_{0b}(y)n_{0b}(y) = constant = C. \tag{4.7}$$

$$T_{0b}(y) = C/n_{0b}(y) \tag{4.8}$$

The suffix 0 indicates the equilibrium fields. To study the linear instability of counter-streaming plasma, we linearize equations (4.1,4.2,4.3,4.4) and choose all the perturbed quantities to have the form of : $f_\alpha = f_\alpha(y)e^{i(k_z z - \omega t)}$. The coupled set of differential equations obtained after linearizing are following :

$$\Omega_\alpha \gamma_{0\alpha}^3 v_{l\alpha z}'' + \left(\omega^2 - k_z^2\right)\Omega_\alpha \gamma_{0\alpha}^3 v_{l\alpha z} +$$

$$\left(\omega^2 - k_z^2\right)\sum_\alpha \frac{n_{0\alpha}}{\Omega_\alpha}v_{l\alpha z} + \sum_\alpha \frac{k_z - \omega v_{0\alpha}}{\Omega_\alpha}\left(n_{0\alpha}v_{l\alpha z}\right)' = 0 \tag{4.9}$$

$$\frac{(\omega^2 - k_z^2)}{\Omega_\alpha}\eta T_{0\alpha}v_{l\alpha y}'' - \frac{(\omega^2 - k_z^2)}{\Omega_\alpha}\eta T_{0\alpha}'v_{l\alpha y}' + \left(\frac{(\omega^2 - k_z^2)}{n_{0\alpha}\Omega_\alpha}\eta T_{0\alpha}'n_{0\alpha}'' + (\omega^2 - k_z^2)\Omega_\alpha \gamma_{0\alpha}\right)v_{l\alpha y}$$

$$-\Omega_\alpha \sum_\alpha n_{0\alpha}v_{l\alpha y} + \left(i\frac{k_z}{\Omega_\alpha}(\omega^2 - k_z^2)\eta T_{0\alpha} - i\left(k_z - v_{0\alpha}\omega\right)\Omega_\alpha \gamma_{0\alpha}^3\right)v_{l\alpha z}' = 0 \tag{4.10}$$

Where $\Omega_\alpha = (\omega - k_z v_0 \alpha)$ and η is the ratio of specific heat. The superscript $'$ is used for $\partial/\partial y$ and $''$ is used for $\partial^2/\partial y^2$. We will use the equations (4.9, 4.10) in this and upcoming chapters to study the linear instability in counter-streaming plasma in various geometry for both homogeneous and inhomogeneous plasma density.

The model configuration chosen for 1-D studies has been shown in Fig. 4.1. The
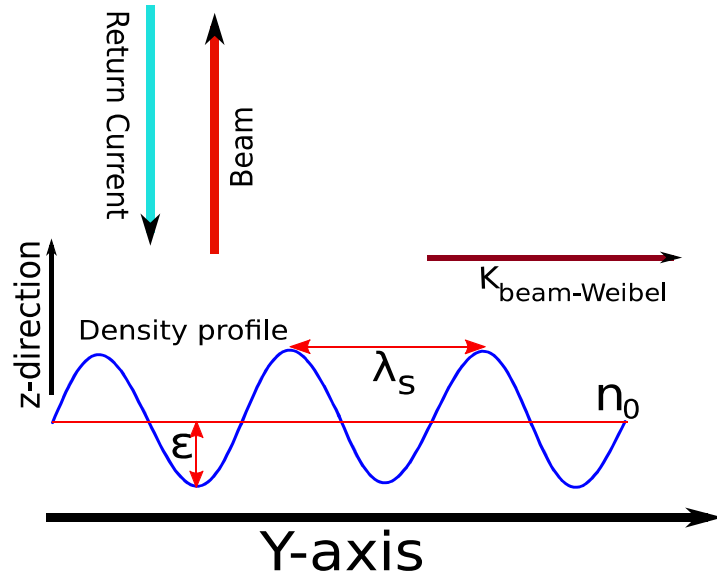
Figure 4.1: Schematic illustration of model configuration which shows the flow of the beam and plasma return in $\pm\hat{z}$ direction. The ripple in density is shown along $\pm\hat{y}$ with ripple scale length λ_s and amplitude ε and the wavevector of beam-Weibel instability in such configuration (along $\pm\hat{y}$ direction).

beam and the return current are chosen to flow along the $\pm\hat{z}$ respectively. The ion density is chosen to have sinusoidal ripple along $\hat{y}$ riding on a constant density of n_0. The amplitude of the ripple is ϵ and the spatial variations are characterized by a wavenumber $k_s = 2\pi/\lambda_s$ as shown in Fig. 4.1.

The linear analysis of beam-Weibel instability in this configuration can be studied by putting $\partial/\partial z = k_z = 0$, in equations (4.9, 4.10). After putting $\partial/\partial z = k_z = 0$, the equations represent the 1-D case which is considered by

us in this chapter, and are the following :

$$\omega\gamma_{0\alpha}v''_{l\alpha z} + \omega^3\gamma^3_{0\alpha}v_{l\alpha z} - \omega\Sigma_\alpha n_{0\alpha}v_{l\alpha z} + i\Sigma_\alpha v_{0\alpha z}(n_{0\alpha}v_{l\alpha y})' = 0, \qquad (4.11)$$

$$\eta T_{0\alpha}v''_{l\alpha y} + \left(2\frac{\eta T_{0\alpha}}{n_{0\alpha}}n'_{0\alpha} + \eta T'_{0\alpha}\right)v_{l\alpha y}' + \left(\frac{\eta T_{0\alpha}}{n_{0\alpha}}n''_{0\alpha} + \eta\frac{T'_{0\alpha}}{n_{0\alpha}}n'_{0\alpha} + \omega^2\gamma_{0\alpha}\right)v_{l\alpha y}$$

$$-\Sigma_\alpha n_{0\alpha}v_{l\alpha y} + i\omega\gamma^3_{0\alpha}v_{0\alpha y}v'_{l\alpha z} = 0, \qquad (4.12)$$

In the presence of density ripple the equations can not be Fourier analyzed in y. Therefore, the eigen value of ω has to be obtained numerically by solving the coupled set of differential equations (4.11, 4.12). For homogeneous plasma, however, eq. (4.11) and eq. (4.12) reduce to

$$\omega\gamma_{0\alpha}v''_{l\alpha z} + \omega^3\gamma^3_{0\alpha}v_{l\alpha z} - \omega\Sigma_\alpha n_{0\alpha}v_{l\alpha z} + i\Sigma_\alpha v_{0\alpha z}n_{0\alpha}v'_{l\alpha y} = 0, \qquad (4.13)$$

$$\eta T_{0\alpha}v''_{l\alpha y} + \omega^2\gamma_{0\alpha}v_{l\alpha y} - \Sigma_\alpha n_{0\alpha}v_{l\alpha y} + i\omega\gamma^3_{0\alpha}v_{0\alpha y}v'_{l\alpha z} = 0, \qquad (4.14)$$

By taking Fourier transform in y, we obtain the following standard dispersion relation for homogeneous plasma

$$\left(\omega^2 - k_y^2 - \sum_\alpha\frac{n_{0\alpha}}{\gamma^3_{0\alpha}}\right)\left(\omega^4\gamma_{0b}\gamma_{0p} - \omega^2\gamma_{0b}\gamma_{0p}\sum_\alpha\frac{n_{0\alpha}}{\gamma_{0\alpha}} - \eta T_{0b}k_y^2(\omega^2\gamma_{0p} - n_{0p})\right)$$

$$-k_y^2\left(\omega^2\gamma_{0b}\gamma_{0p}\sum_\alpha\frac{n_{0\alpha}v^2_{0\alpha}}{\gamma_{0\alpha}} - n_{0p}n_{0b}\sum_\alpha v^2_{0\alpha} + 2n_{0p}n_{0b}v_{0p}v_{0b} - \eta T_{0b}k_y^2 n_{0p}v^2_{0p}\right) = 0 \qquad (4.15)$$

This equation contains two oscillatory modes (Langmuir wave) and one purely growing electromagnetic mode which is known as beam-Weibel instability. For cold plasma, dispersion relation 4.15 further gets simplified and after rearrangement, takes the following form where we can easily figure out the oscillating and beam-Weibel instability mode:

$$\left(\omega^2 - \sum_\alpha\frac{n_{0\alpha}}{\gamma_{0\alpha}}\right)\left(\omega^4 - \omega^2\left(k_y^2 + \sum_\alpha\frac{n_{0\alpha}}{\gamma^3_{0\alpha}}\right) + k_y^2\sum_\alpha\frac{n_{0\alpha}v^2_{0\alpha}}{\gamma_{0\alpha}}\right)$$

$$-k_y^2\left(\sum_\alpha\frac{n_{0\alpha}v_{0\alpha}}{\gamma_{0\alpha}}\right)^2 = 0, \qquad (4.16)$$

The last term in the dispersion relation arises due to charge separation in plasma and is responsible for the coupling of Langmuir waves $\left(\omega^2 - \sum_\alpha \frac{n_{0\alpha}}{\gamma_{0\alpha}}\right)$ with the beam-Weibel instability and transverse oscillations.

4.3   Analytical studies

For analytical tractability of the inhomogeneous density problem a choice of sinusoidal variation riding on a homogeneous background density such as

$$n_{0i} = [1 + \varepsilon cos(k_s y)], \tag{4.17}$$

is chosen. Here ε is the amplitude of the density ripple and $k_s = 2\pi m/L_y$ (m= L_y/λ_s is an integer) is its wave number with L_y as the system length. To satisfy the quasi-neutrality condition, the equilibrium beam and plasma density are chosen as

$$
\begin{aligned}
n_{0b} &= \beta(1 + \varepsilon cos(k_s y)) \\
n_{0p} &= (1 - \beta)(1 + \varepsilon cos(k_s y)),
\end{aligned}
\tag{4.18}
$$

where β is a fraction. Now choosing the perturbed fields as

$$f_\alpha = \Sigma_j^{\dots,\pm 2,\pm 1,0} f_{\alpha j} e^{i((k_y + jk_s)y - \omega t)}$$

and assuming ε to be small so that retaining only the first order terms (as done in the paper by Mishra *et al.* [56]), we can evaluate the growth rate. We evaluate the growth rate Γ_{gr} as a function of k_y. Expanding the linear coupled set of differential equations (4.11, 4.12) corresponding to perturbed mode $j = 0, \pm 1$, and equating

the same exponent of right-hand side to left-hand side, we get following equations:

$$\Omega_\alpha \gamma_{0\alpha}^3 \left(\omega^2 - k_d^2\right) v_{d\alpha z} + \omega^2 \sum_\alpha \frac{\beta_\alpha}{\Omega_\alpha} v_{d\alpha z} + \omega^2 \sum_\alpha \frac{0.5\varepsilon\beta_\alpha}{\Omega_\alpha} v_{\alpha z} - i \sum_\alpha \frac{v_{0\alpha}\omega_\alpha}{\Omega_\alpha} \beta_\alpha k_d v_{d\alpha y}$$

$$-i \sum_\alpha \frac{v_{0\alpha}\omega_\alpha}{\Omega_\alpha} 0.5\varepsilon\beta_\alpha k_d v_{\alpha y} = 0, \tag{4.19}$$

$$\Omega_\alpha \gamma_{0\alpha}^3 \left(\omega^2 - k_o^2\right) v_{\alpha z} + \omega^2 \sum_\alpha \frac{\beta_\alpha}{\Omega_\alpha} v_{\alpha z} + \omega^2 \sum_\alpha \frac{0.5\varepsilon\beta_\alpha}{\Omega_\alpha} \left(v_{d\alpha z} + v_{a\alpha z}\right) - i \sum_\alpha \frac{v_{0\alpha}\omega_\alpha}{\Omega_\alpha} \beta_\alpha k_o v_{\alpha y}$$

$$-i \sum_\alpha \frac{v_{0\alpha}\omega_\alpha}{\Omega_\alpha} 0.5\varepsilon\beta_\alpha k_o \left(v_{d\alpha y} + v_{a\alpha y}\right) = 0, \tag{4.20}$$

$$\Omega_\alpha \gamma_{0\alpha}^3 \left(\omega^2 - k_a^2\right) v_{a\alpha z} + \omega^2 \sum_\alpha \frac{\beta_\alpha}{\Omega_\alpha} v_{a\alpha z} + \omega^2 \sum_\alpha \frac{0.5\varepsilon\beta_\alpha}{\Omega_\alpha} v_{\alpha z} - i \sum_\alpha \frac{v_{0\alpha}\omega_\alpha}{\Omega_\alpha} \beta_\alpha k_a v_{a\alpha y}$$

$$-i \sum_\alpha \frac{v_{0\alpha}\omega_\alpha}{\Omega_\alpha} 0.5\varepsilon\beta_\alpha k_a v_{\alpha y} = 0, \tag{4.21}$$

$$\left(\frac{\omega^2}{\Omega_\alpha\beta_\alpha}\eta c_\alpha k_d^2 - \omega^2\Omega_\alpha\gamma_{0\alpha}\right) v_{d\alpha y} + \Omega_\alpha \sum_\alpha \beta_\alpha v_{d\alpha y} + 0.5\varepsilon\frac{\omega^2}{\Omega_\alpha\beta_\alpha}\eta c_\alpha [k_d^2 - k_0(2k_0 - k_s)]v_{\alpha y}$$

$$+0.5\varepsilon\Omega_\alpha \sum_\alpha \beta_\alpha v_{\alpha y} - v_{0\alpha}\omega_\alpha\Omega_\alpha\gamma_{0\alpha}^3 k_d v_{d\alpha z} = 0, \tag{4.22}$$

$$\left(\frac{\omega^2}{\Omega_\alpha\beta_\alpha}\eta c_\alpha k_0^2 - \omega^2\Omega_\alpha\gamma_{0\alpha}\right) v_{\alpha y} + \Omega_\alpha \sum_\alpha \beta_\alpha v_{\alpha y} + 0.5\varepsilon\frac{\omega^2}{\Omega_\alpha\beta_\alpha}\eta c_\alpha [k_0^2 - k_d(2k_d + k_s)]v_{d\alpha y} +$$

$$0.5\varepsilon\frac{\omega^2}{\Omega_\alpha\beta_\alpha}\eta c_\alpha [k_0^2 - k_a(2k_a - k_s)]v_{a\alpha y} + 0.5\varepsilon\Omega_\alpha \sum_\alpha \beta_\alpha \left(v_{d\alpha y} + v_{a\alpha y}\right)$$

$$-v_{0\alpha}\omega_\alpha\Omega_\alpha\gamma_{0\alpha}^3 k_0 v_{\alpha z} = 0, \tag{4.23}$$

$$\left(\frac{\omega^2}{\Omega_\alpha\beta_\alpha}\eta c_\alpha k_a^2 - \omega^2\Omega_\alpha\gamma_{0\alpha}\right) v_{a\alpha y} + \Omega_\alpha \sum_\alpha \beta_\alpha v_{a\alpha y} + 0.5\varepsilon\frac{\omega^2}{\Omega_\alpha\beta_\alpha}\eta c_\alpha [k_a^2 - k_0(2k_0 + k_s)]v_{\alpha y}$$

$$+0.5\varepsilon\Omega_\alpha \sum_\alpha \beta_\alpha v_{\alpha y} - v_{0\alpha}\omega_\alpha\Omega_\alpha\gamma_{0\alpha}^3 k_a v_{a\alpha z} = 0, \tag{4.24}$$

where $k_d = (k_y - k_s)$, $k_0 = k_y$, and $k_a = (k_y + k_s)$.

Typically, for laser intensity I$= 1 \times 10^{19} W/cm^2$, the fast electrons are generated with average Lorentz factor $< \gamma_{0b} >\approx \sqrt{a_0^2/2 + 1} \approx 2.2$ which correspond to velocity $v_{0b} \approx 0.9c$. Therefore, in our studies, we choose the beam velocity $v_{0b} = 0.9c$. The plots are shown in Fig. 4.2 compare the growth rates for the homogeneous

case with rippled cases. In Fig. 4.2 (a), we plot the growth rate Γ_{gr} versus wave vector k_y for a homogeneous (black curve) and rippled cold beam plasma system for ε=0.1, for $k_s = \pi$(green curve), 2π(red curve) and 3π(blue curve). The other parameters are $n_{0b}/n_{0p} = 1/9$ or $n_{0b}/n_{0e} = 0.1$, $v_{0p} = -0.1c$, $T_{0b} = 0$, and $T_{0p} = 0$. From this plot, we can see that for the homogeneous case, the Γ_{gr} increases with k_y for small values of k_y and saturates at $k_y \simeq 3$. However, for the rippled case (ε=0.1) Γ_{gr} for small values of k_y is large compared to the homogeneous one. The increase in Γ_{gr} with k_y is very mild and ultimately there is a saturation at higher k_y values. It should be noted that even when k=0, the perturbed fields have variations of the scale of the k_s and its multiples. The maximum value of the growth rate Γ_{gr} increases with k_s for a cold system.

The effect of the transverse beam temperature ($T_{0b\perp} = 10$ keV) over the growth rate can be seen in Fig. 4.2(b). The growth rate Γ_{gr} of the homogeneous hot beam and cold background plasma system (black curve) increases with k_y for small values of k_y but starts decreasing after $k_y > 0.5$ and completely stabilizes at higher wave numbers ($k_y > 1$). The effect of ripple on the hot beam and cold background plasma can be seen in Fig. 4.2(b), Fig. 4.2(c) and Fig. 4.2(d). The Fig. 4.2(b) illustrate the effect of ripple scale length k_s on the Γ_{gr}. We see that for the ripple case, there appears two shifted additional unstable modes. The dependence on the amplitude ε and the ripple scale length k_s have been shown in Fig. 4.2(c) and Fig. 4.2(d). Thus the study shows that at finite transverse beam temperature the effect of increasing k_s as well as ε is to stabilize the beam-Weibel instability. In Table - I, we have tabulated the value of maximum growth rate for various cases.

TABLE I

The maximum growth rate of filamentation instability evaluated analytically considering the density ripple amplitude as weak.

$T_{0b\perp}(keV)$	ε	k_s	$\Gamma_{gr}(\text{max.})$
0.0	0.0	0.0	0.2006
0.0	0.1	π	0.2057
0.0	0.1	2π	0.2074
0.0	0.1	3π	0.2085
10.0	0.0	0.0	0.0840
10.0	0.1	π	0.0831
10.0	0.1	2π	0.0770
10.0	0.1	3π	0.0648
10.0	0.2	2π	0.0510
10.0	0.2	3π	0.0000

It is thus noted that for cold beam there is no significant difference between the growth rates of homogeneous and ripple cases except at long wavelengths. However, when the beam temperature is chosen as finite the growth rate for the ripple case significantly reduces with increasing k_s as well as ε. The analytical inference is further corroborated by Particle - In- Cell (PIC) simulations. The results of PIC studies are presented in the next section.
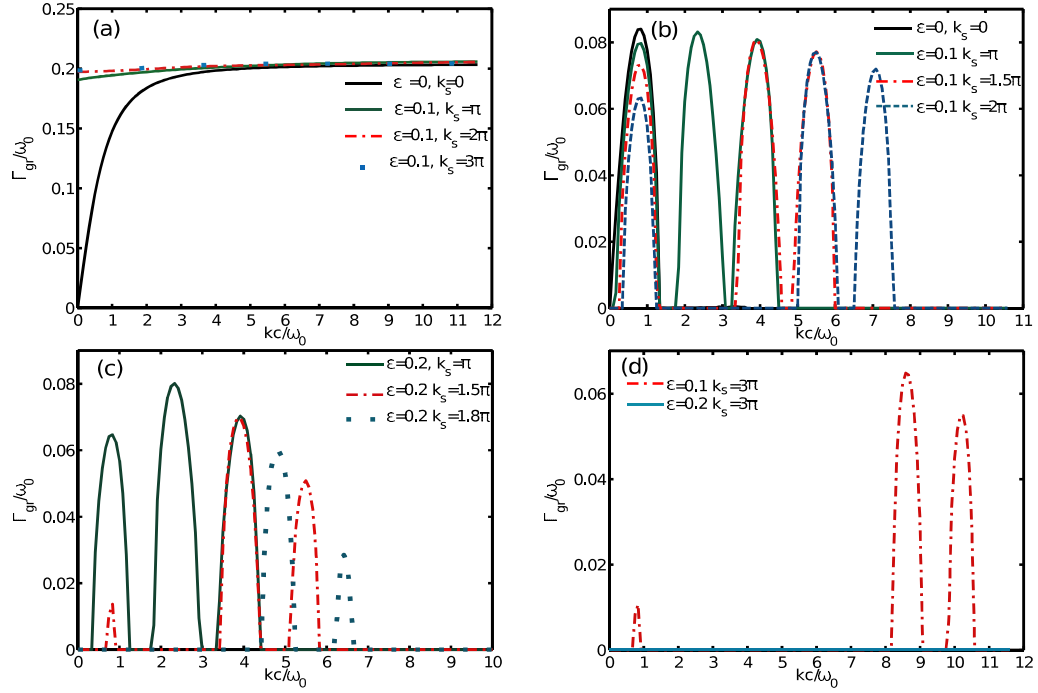
Figure 4.2: Linear growth rate of beam-Weibel instability as a function wavenumber $k = k_y$: (a) shows growth rate for cold homogeneous beam-plasma system (solid line black color), for parameters $n_{0b}/n_{0e} = 0.1$, $v_{0b} = 0.9c$, $v_{0p} = -0.1c$ and for rippled beam-plasma, ε=0.1 at k_s=π(solid line green color), k_s=2π (-.)and k_s=3π(.). (b) at the transverse beam temperature $T_{b0\perp}$=10 keV, homogeneous(solid black), rippled system with ε=0.1 at k_s=π(solid green), 1.5π(-.) and 2π(−) (c) at transverse beam temperature $T_{b0\perp}$=10 keV, rippled system with ε=0.2 at k_s=π(solid green), 1.5π(-.) and 1.8π(..) (d) at the transverse beam temperature $T_{b0\perp}$=10 keV, rippled system with k_s=3π for ε=0.1(-.-) and 0.2 (solid)

4.4   PIC simulation details

We have performed Particle-In-Cell simulation to study the propagation of the beam in both homogeneous and rippled plasma systems. Only one-dimensional variation in space (perpendicular to the beam propagation) has been chosen for our numerical studies here, for the purpose of comparison with linear analytical studies.

The ions are not allowed to move in the simulations and merely provide a neutralizing background for the plasma. This makes the simulation faster and is a valid approximation to study the fast electron time scale phenomena of interest. The uniform plasma density n_0 is chosen to be $10n_c$ where $n_c = 1.1 \times 10^{21} cm^{-3}$ is the critical density for a $1\mu m$ wavelength of laser light. The spatial simulation box length $L_y = 60\ c/\omega_0$, where $c/\omega_0 = d_e = 5.0 \times 10^{-2}\mu m$ is the skin depth corresponding to the density n_0. The one-dimensional simulation box is divided into 6000 cells. The grid size is, therefore, equal to $0.01\ d_e$. Thus, scales shorter than the skin depth can be resolved. The total number of electrons and ions chosen for the simulations are 1800000 each. This number represents the sum of background n_{0p} and beam n_{0b} electrons. The choice of rippled ion density and the separation between the two electron species of beam and background are made as per Eq.(4.17) and Eq.(4.18)

The beam temperature $T_{b0\perp}$ is chosen to be finite in the perpendicular direction according to Eq.(4.8). The time step is decided by the Courant condition. The charge neutrality, as well as the null value of total current density, is ensured initially. The considered system is also field free initially as required by equilibrium configuration.

4.5   Simulation observations

For the homogeneous plasma density case (e.g. $\epsilon = 0.0$, $k_s = 0.0$), the system is plagued by the usual beam-Weibel instability. This causes spatial separation between the forward and reverse electron currents. The separation leads to finite current density in space resulting in the growth of magnetic field energy. The evolution of box averaged magnetic field energy normalized by $E_0^2 = (m_e c \omega_0 / e)^2$

energy of the system is shown in Fig. 4.3 (b), Fig. 4.4 (b) and Fig. 4.5 (b). After an initial transient, the curve settles down to a linear regime and subsequently shows saturation.   The slope of the linear portion of the main curve has been
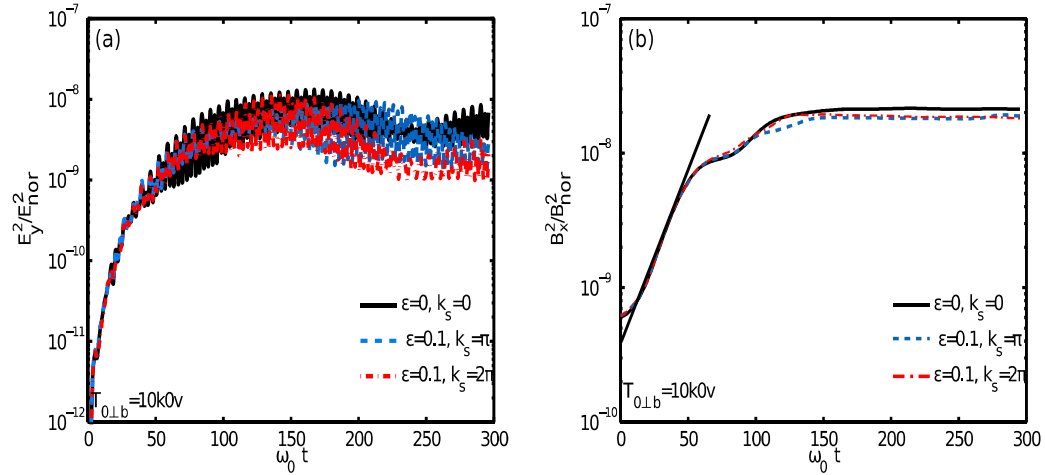
Figure 4.3: Temporal evolution of the field energy densities for cold homogeneous and rippled beam-plasma simulation. (a) normalized electrostatic y-component of electric field energy (b) normalized x-component of magnetic field energy

employed for the evaluation of the growth rate of the maximally unstable mode in the simulation. The growth rate has been tabulated in Table - II for various cases of parameters.

TABLE II:

The maximum growth rate of beam-Weibel instability calculated from PIC simulation.

$T_{0b\perp}(keV)$	ε	k_s	$\Gamma_{gr}(\text{max.})$
0.0	0.0	0.0	0.2000
0.0	0.1	2π	0.2000
0.0	0.1	3π	0.2000
10.0	0.0	0.0	0.0508
10.0	0.1	2π	0.0349
10.0	0.1	3π	0.0333
10.0	0.2	2π	0.0173
10.0	0.2	3π	0.0109
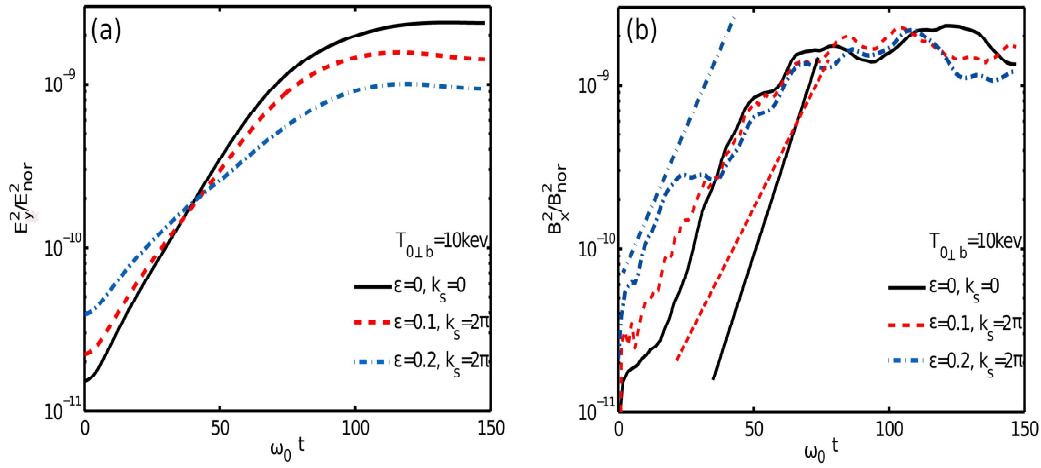
Figure 4.4: Temporal evolution of the field energy densities for hot ($T_{b0\perp}$=10 keV) homogeneous and rippled beam-plasma simulation. (a) normalized electrostatic y-component of electric field energy for ε=0, k_s=0 and ε=0.1 and 0.2 for k_s=2π (b) normalized x-component of magnetic field energy for ε=0, k_s=0 and ε=0.1 and 0.2 for k_s=2π

From the table as well as by following the complete evolution it is evident that when the transverse temperature of the beam electrons is zero the rippled density causes no change. With increasing value of ϵ and k_s the growth rate decreases when the temperature of the beam and background electrons is finite. This trend is similar to the behavior of growth rate evaluated analytically, shown in Table - I. When the plasma density is homogeneous the value of the growth rates evaluated analytically and through simulations are in good agreement. However, in the presence of ripple, there is a small disagreement between the quantitative values. This can be attributed to the approximate nature of the analytical treatment, wherein the amplitude of ripple was assumed to be weak.

From Figures 4.3 (a), 4.4 (a) and 4.5 (a) it can also be seen that along with the growth of magnetic field energy, electrostatic field energy also grows. The development of an electric field directed along y during the course of simulation is responsible for this electrostatic energy. This electrostatic field develops as a result of the redistribution and bunching of electron charges in physical y space. It can be seen from the phase space plots of Fig. 4.6 that the electrons do reorganize in physical space. Furthermore, the locations where these electrons get accumu-
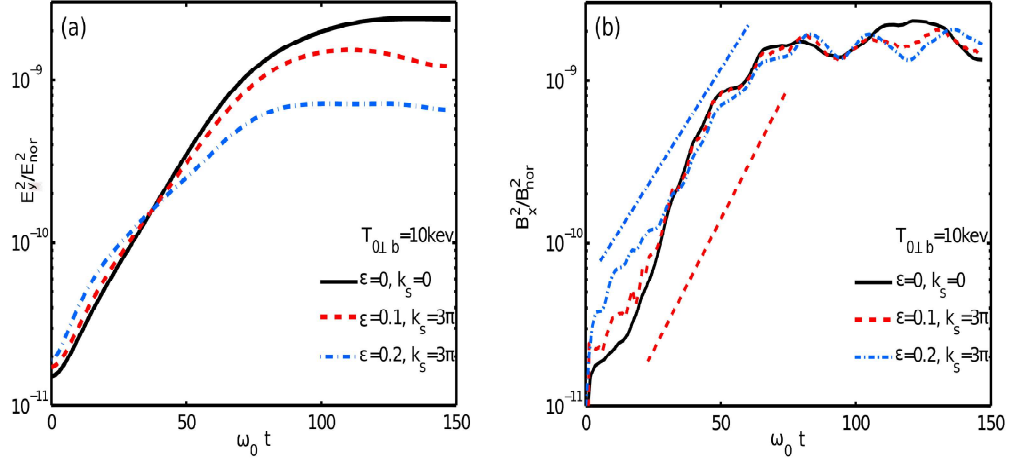
Figure 4.5: Temporal evolution of the field energy densities for hot ($T_{b0\perp}$=10 keV) homogeneous and rippled beam-plasma simulation. (a) normalized electrostatic y-component of electric field energy for ε=0, k_s=0 and ε=0.1 and 0.2 for k_s=3π (b) normalized x-component of magnetic field energy for ε=0, k_s=0 and ε=0.1 and 0.2 for k_s=3π

lated are the regions with maximal currents and negligible magnetic and electric field as can be seen from Fig. 4.7 Finally we provide a comparison between the cases of homogeneous and rippled plasmas. It should be noted that the typical scale length of the magnetic field developed during the initial phase in the homogeneous case (Fig. 4.8 (a)) is of the order of the background plasma skin depth (e.g. $5.33 \times 10^{-2} \mu m$). For the rippled case, the scale length of the magnetic field matches initially with the ripple scale length defined by the choice of k_s (Fig. 4.8 (b))(provided the scale length of ripple is smaller than the skin depth) else it is determined by the typical value of skin depth. At later stages (the nonlinear phase of the instability), however, the magnetic structures coalesce and acquire long scales typically comparable to simulation box size in both homogeneous (Fig. 4.8 (c)) and rippled (Fig. 4.8 (d)) (provided the growth rate remains finite in this case) cases. To summarize the main observations are: (i) the rippled density causes no significant difference in the growth rate when the transverse temperature is chosen to be zero. (ii) the growth rate of the beam-Weibel instability in the rippled density case is reduced compared to the homogeneous case when the transverse beam temperature is finite, (iii) The momentum p_y is typically quite large for beam electrons
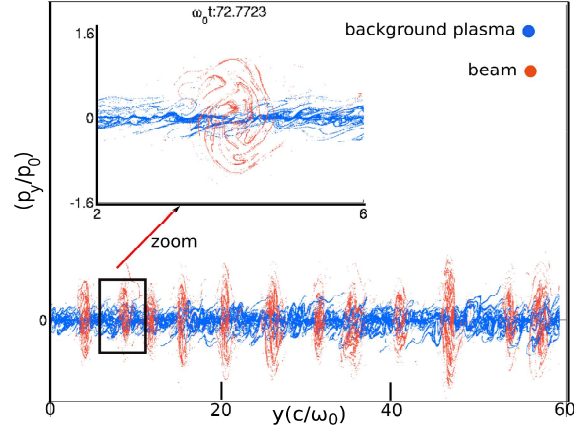
Figure 4.6: Phase space plot for homogeneous cold beam plasma at $\omega_0 t = 74.0555$

compared to the background plasma electrons. (iv) in the nonlinear regime the typical profile of electrostatic field created due to electron bunching in y is similar to that of the magnetic field. The zeros of both the fields coincide with each other in space and it is these very locations where electron bunching is observed.
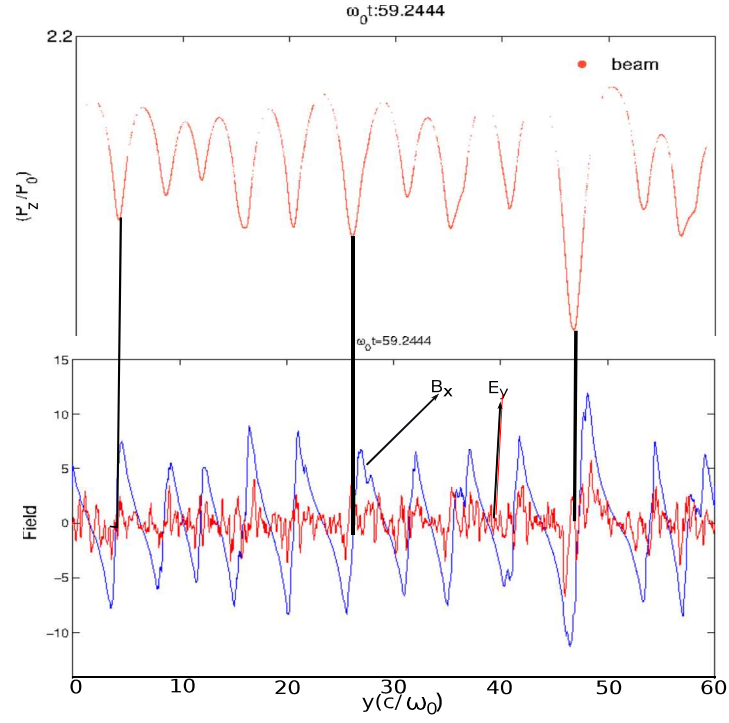
Figure 4.7: The accumulation of electrons in the regions of maximal currents and negligible magnetic and electric field
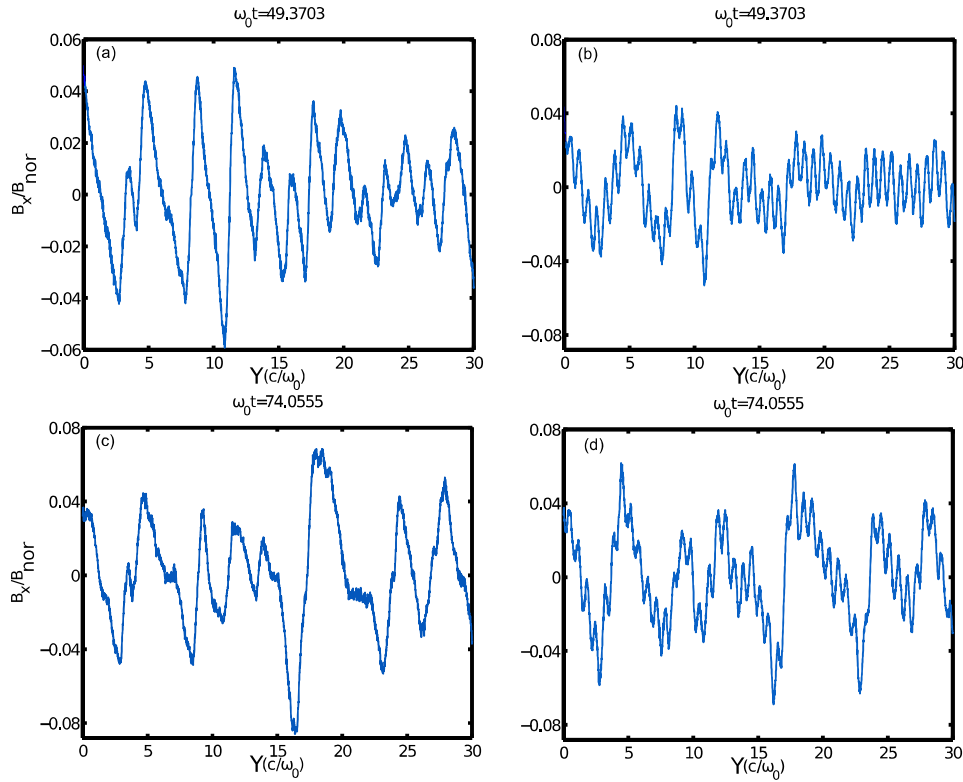
Figure 4.8: Spatial configuration of normalized magnetic field homogeneous and rippled hot beam plasma (a) $\varepsilon=0.0$, $k_s=0$ at $\omega_0 t=49.3703$ (b) $\varepsilon=0.2$, $k_s=3\pi$ at $\omega_0 t=49.3703$ (c) $\varepsilon=0.0$, $k_s=0$ at $\omega_0 t=74.0555$ (d) $\varepsilon=0.2$, $k_s=3\pi$ at $\omega_0 t=74.0555$

4.6   Interpretation of numerical observations

We now provide a simplified understanding of the observations made by PIC simulations listed out in the previous section. In order to understand these results we consider the 1-D limit (with only variations along y being permitted) of the two fluid system of beam and background electrons described in section II. In 1-D the momentum equations of the two electron species from Eqs.(1) are:

$$\frac{dp_{yb}}{dt} = -\left[-\frac{\partial \phi}{\partial y} + v_{zb}B_x\right] - \frac{1}{n_b}\frac{\partial P_b}{\partial y} \tag{4.25}$$

$$\frac{dp_{yp}}{dt} = -\left[-\frac{\partial \phi}{\partial y} + v_{zp}B_x\right] \tag{4.26}$$

$$\frac{dp_{zb}}{dt} = -\left[-\frac{\partial A_z}{\partial t} - v_{yb}B_x\right] \tag{4.27}$$

$$\frac{dp_{zp}}{dt} = -\left[-\frac{\partial A_z}{\partial t} - v_{yp}B_x\right] \tag{4.28}$$

$$\tag{4.29}$$

Here $p_{i\alpha}$ for $i = y$ and $i = z$ corresponds to the y and z component of momentum respectively for the beam $\alpha = b$ or plasma $\alpha = p$ electrons. Also $v_{i\alpha} = p_{i\alpha}/\gamma_\alpha$ (with γ_α being the relativistic factor) is the corresponding velocity. Here P_b represents the transverse pressure which is zero for the case when the system is cold. The scalar and vector potentials are represented by ϕ and $\vec{A}$ respectively. In 1-D only A_z component is finite. Thus the only finite component of magnetic field is along $\hat{x}$ and $B_x = \partial A_z/\partial y$.

The continuity equation can be written as

$$\frac{\partial n_\alpha}{\partial t} + \vec{v}_{y\alpha}\frac{\partial n_\alpha}{\partial y} + n_\alpha\frac{\partial v_{y\alpha}}{\partial y} = 0 \tag{4.30}$$

The Maxwell's equation become

$$\frac{\partial^2 \phi}{\partial y^2} = (\delta n_b + \delta n_p) \tag{4.31}$$

$$\frac{\partial^2 A_z}{\partial t^2} = \frac{\partial B_x}{\partial y} - [n_b v_{yb} + n_p v_{yp}] \tag{4.32}$$

Here n_b and n_p are the total densities of the beam and plasma electrons and δn_b and δn_p is the difference between the total and equilibrium densities respectively. If one considers the transverse temperature to be zero, the linearization of the above set of equations has no other term dependent on the electron densities except for $E_y = -\partial\phi/\partial y$ in the momentum equation. However, beam-Weibel being primarily an electromagnetic instability the electrostatic field is very weak. Thus, the predominant term in the momentum equation is due to the second term of $v_{y0b}B_z$, which is not influenced by the electron density. Thus, in the limit of zero temperature the homogeneous and inhomogeneous(ripple) cases do not show any significant difference.

When the transverse temperature is finite our simulations show the reduction in the beam-Weibel growth rate. In this case the pressure term in Eq. (4.8) is effective and depends on the density inhomogeneity. It has been shown by approximate analytical studies in [56] repeated and presented by us in Fig. 4.2 that the growth rate indeed decreases in the inhomogeneous case. This is the main result of our simulations which qualitatively verifies the approximate results of [56].

As we have stated earlier along with the development of magnetic field an electrostatic field also develops. This happens due to the bunching of electron densities at the location of zero magnetic field as shown in Fig. 4.7. At the location of zero magnetic fields, the perturbed density shows a maxima and the electric field also passes through zero. This arrangement is self-consistent. The Lorentz force at these locations vanishes and hence a particle has a greater probability to accumulate over there. The location of maximum accumulation of electron density, in turn, results in the vanishing of the second derivative of the electric field and for a Fourier spectrum, this location should correspond to the zero of electric field.

4.7   Summary

We have shown through 1D3V PIC simulations that the growth rate of beam-Weibel instability gets reduced in the presence of ripple in density. A detailed study on the dependence of scale length, plasma temperature etc., have been carried out. It is known that the transverse electromagnetic perturbation in an un-magnetized plasma with scale length shorter than the skin depth ($c/\omega_0 > 2\pi/k_s$) are typically

damped. The ripple in plasma density perpendicular to the flow direction with scale length shorter than skin depth provides a coupling between the growing electromagnetic mode and the short scale perturbations. Thus the inhomogeneity (ripple) acts as a conduit for the transfer of the energy of the growing mode to short scale damped perturbations resulting in the suppression of the mode.

This beam-Weibel instability analysis for the inhomogeneous medium was studied analytically earlier by Mishra *et al.* [56] wherein it was shown analytically using two fluid description that the beam-Weibel instability gets suppressed. The present work supplements it with PIC studies. Our PIC simulations support the analytical observations qualitatively. The quantitative values of the growth rate, however, shows significant differences in certain cases. For instance, the growth rate for 2π and 3π (for ϵ=0.1 and $T_{0b\perp}$=10Kev) differ by an order of magnitude, whereas the PIC results show the minor difference in the growth rate. The differences between fluid and PIC results seem to be significant for finite temperature cases, for which fluid treatment can be approximate. This relevance to a recent experimental observation of efficient transport of mega ampere of electron currents through aligned carbon nanotube arrays. The ionization of the carbon nanotubes by the front of laser pulse produces the plasma which has inhomogeneous(ripple) density. Since the beam-Weibel instability gets suppressed in such an inhomogeneous(ripple) plasma, the current separation could get reduced leading to the propagation of beam electrons over large distances.

In the present work full $1D3V$ Particle-in-Cell (PIC) simulations have been carried out for the propagation of relativistic electron beams (REB) through an inhomogeneous background plasma. The suppression of the filamentation instability, responsible for beam divergence, is shown. The simulation also confirms that in the nonlinear regime, the REB propagation is better when it propagates through a plasma whose density is inhomogeneous transverse to the beam. The role of inhomogeneity scale length, its amplitude, and the transverse beam temperature etc., in the suppression of the instability, is studied in detail.

5

Two-dimensional study of beam-plasma system

In this chapter, we present 2-D PIC simulation of beam-plasma system. Two different simulation geometries were considered. In the first case, beam is chosen to flow out of the simulation plane. Thus, in this case, only those instabilities which are transverse to the flow direction such as (beam - Weibel) mode can be observed. The longitudinal two stream mode are absent in this system as they require variations along beam propagation direction. In the second case, we consider one of the dimensions of the simulation box to be along the beam propagation direction. In this geometry, the longitudinal, two stream, beam Weibel as well as oblique modes can get excited. The role of inhomogeneous plasma transverse to the propagation direction is investigated in detail.

5.1 Introduction

As mentioned in chapter 1, the interactions of high power laser with a solid target and /or dense plasma generates relativistic electron beam. The generated relativistic electron beam propagates inside the plasma and induces return current in the background plasma to overcome the space charge effects. If the size of beam radius is much bigger than the skin depth of background electron plasma, spatially overlapping return currents flow in opposite direction of the beam. Such configuration of beam-plasma system is highly susceptible to beam-Weibel and coupled two stream beam-Weibel instabilities. These instabilities break-up the relativistic

electron beam into a large number of current filaments. As time evolves, the like current filaments attract each other and finally coalescence.

In the next section of this chapter, we study the propagation of relativistic electron beam in a simulation plane transverse to the beam propagation direction. The benefit of choosing such a geometry is that only the beam Weibel instability can get excited in this case. Thus the exclusive role of beam-Weibel instability in the evolution of the beam leading to magnetic field generation in an unmagnetized plasma can be understood in considerable detail.

In section 5.3, one dimension of the 2-D simulation plane contains the propagation direction of the relativistic electron beam. In this case, all the modes, viz., beam-Weibel instability, two-stream and oblique modes can get excited. The combined role of all these instabilities lead to the break up of beam into tilted current filaments. We also choose to consider the role of an inhomogeneous plasma density transverse to the flow direction of the evolution.

5.2 Case I: Dynamics in the 2-D plane transverse to beam propagation

5.2.1 Geometry and governing equations

We consider a spatially infinite (in simulation periodic boundary conditions are employed), collisionless, quasi-neutral and unmagnetized electron beam-plasma system. The electron beam propagates with density n_b, mean velocity v_b, charge q_b, and temperature T_b in X-direction, and induces a return current in background electrons of plasma in negative X-direction with density n_p, mean velocity v_p and temperature T_p. The background ions do not respond at electron plasma frequency time scale because of its large inertia. Therefore, we keep ions at rest. Furthermore, we consider a charge and current neutralized system initially. So initially the system is in equilibrium with no electromagnetic fields. In such model, we describe each species by choosing the proper initial distribution function f_s^0, the suffix s stands b for beam and p for plasma. This system can be described by the following

set of Maxwell-Vlasov equations.

$$\frac{\partial f_s}{\partial t} + \vec{v} \cdot \frac{\partial f_s}{\partial \vec{r}} + q_s \left(\vec{E} + \frac{\vec{v} \times \vec{B}}{c} \right) \frac{\partial f_s}{\partial \vec{p}} = 0 \tag{5.1}$$

$$\frac{1}{c} \frac{\partial \vec{B}}{\partial t} = -\nabla \times \vec{E} \tag{5.2}$$

$$\frac{1}{c} \frac{\partial \vec{E}}{\partial t} = \nabla \times \vec{B} - \frac{4\pi}{c} \Sigma_s \vec{J_s} \tag{5.3}$$

5.2.2 Kinetic theory of linear beam-Weibel instability

We linearize the coupled Vlasov Poisson equation and take Fourier transform in space and time. Furthermore, we use quasi-neutrality condition ($\Sigma_s q_s n_{0s} = 0$), and current neutrality condition ($\Sigma_s q_s n_{0s} \vec{v_{0s}} = 0$) in Maxwell-Vlasov equation to obtain well known linear dispersion relation

$$\left(\varepsilon_{xx} - \frac{k^2 c^2}{\omega^2} \right) \varepsilon_{yy} = \varepsilon_{yx} \varepsilon_{xy} \tag{5.4}$$

The form of dielectric tensor is defined as

$$\varepsilon_{ij} = \omega^2 \delta_{ij} + \sum_s \frac{\omega_s^2}{n_s} \int d^3 \vec{p_s} \frac{p_{si} p_{sj}}{\gamma_{0s}} \frac{\vec{k} \cdot \frac{\partial f_s}{\partial \vec{p_s}}}{m_s \gamma_{0s} \omega - \vec{k} \cdot \vec{p_s}} + \sum_s \frac{\omega_s^2}{n_s} \int d^3 \vec{p_s} \frac{p_{si}}{\gamma_{0s}} \frac{\partial f_s}{\partial p_{sj}} \tag{5.5}$$

where $\gamma_{0s} = (1 + \frac{\vec{p_{0s}^2}}{m_s c^2})^{1/2}$ is the Lorentz factor, $\omega_s = 4\pi n_s q_s^2 / m_s$ is s species plasma frequency, and $\omega_0^2 = \Sigma_s \omega_s^2$. For analytical tractability, we choose relativistic drifting Maxwellian distribution function.

$$f_{0s}(p_x, py) = \frac{n_s}{2\pi m_s \gamma_{0s}^2 \sqrt{T_{\perp s} T_{\parallel s}}} exp \left[-\frac{p_y^2}{2m_s \gamma_{0s} T_{\perp s}} - \frac{(p_x - p_s)^2}{2m_s \gamma_{0s}^3 T_{\parallel s}} \right] \tag{5.6}$$

where p_s is drift momentum. The dielectric tensor components can be obtained from eq. (5.5) as follow

$$\varepsilon_{xx} = 1 - \sum_s \frac{\omega_s^2}{\gamma_{0s}^3 \omega^2} - \sum_s \frac{\omega_s^2}{\gamma_{0s} \omega^2} \frac{p_s^2 + m_s \gamma_{0s}^3 T_{\parallel s}}{2m_s \gamma_{0s} T_{\perp s}} Z'(\xi_s) \tag{5.7}$$

$$\varepsilon_{zz} = 1 - \sum_s \frac{\omega_s^2}{\gamma_{0s}} \frac{Z'(\xi_s)}{k^2 \zeta_s^2} \qquad (5.8)$$

$$\varepsilon_{yx} = -\sum_s \frac{\omega_s^2}{\gamma_{0s}\omega^2} \frac{p_s}{\sqrt{2m_s\gamma_{0s}T_{\perp s}}} \left(Z(\xi_s) + \frac{Z''(\xi_s)}{2} \right) \qquad (5.9)$$

where $\zeta_s = \sqrt{2T_{\perp s}/\gamma_{0s}m_s}$, $\eta_s = \omega/k\zeta_s$, $Z(\xi_s) = \pi^{-1/2}\int_{-\infty}^{\infty}\frac{e^{-t^2}}{t-\xi_s}dt$ is plasma dispersion function and the $\prime$ indicates derivative. For cold beam-plasma system, we consider only drifting distribution function, and in this case, the growth rate of beam-Weibel instability calculated from the dispersion relation is

$$\Gamma_{gr} = \frac{\omega_b v_{0b}}{c} \left(\frac{k^2}{\gamma_{0b}\left(k^2 + \omega_p^2/c^2\right)} \right)^{1/2} \qquad (5.10)$$

and the maximum growth is

$$\Gamma_{gr}^{cold}(max.) \sim \frac{\omega_0 v_{0b}}{c} \left(\frac{n_{0b}}{\gamma_{0b}n_{0p}} \right)^{1/2} \qquad (5.11)$$

For warm case, the growth rate obtained from dispersion relation is given by

$$\Gamma_{gr} \simeq \frac{\omega_b^4 v_{0b}^2 \left(\sqrt{\frac{n_b}{n_p}} + \sqrt{\frac{n_p}{n_b}} \right)^2}{k^2 T_{\perp p} T_{\perp b} BD/m^2} + \frac{\omega_b^2(\gamma_{0b} - 1/\gamma_{0b}^3) - k^2 c^2)}{D} \qquad (5.12)$$

where $B = \sum_s \omega_s^2 m_s/k^2 T_{\perp s}$ and $D = \frac{\sqrt{\pi}}{\sqrt{2}k}\left[\sum_s \omega_s \frac{v_{0s}^2 + \gamma_{0s}T_{\parallel s}/m_s}{\gamma_{0s}\sqrt{(T_{\perp s}/\gamma_{0s}m_s)^3}} \right]$. The maximum growth rate for isotropic distribution ($T_{\parallel s} = T_{\perp s}$) and $T_b \gg T_p$ can be given by

$$\Gamma_{gr}(max.) \sim \frac{2\sqrt{6}}{9\sqrt{\pi}} \frac{[\omega_b^2 v_{0b}^2 m_e/T_b + \omega_b^2(\gamma_{0b} - 1/\gamma_{0b}^3)]}{\omega_p^2(v_{0p}^2 + T_p/m_e)c}(T_p/m_e)^{3/2} \qquad (5.13)$$

Where m_e is the rest mass of an electron. We evaluate the linear growth rate Γ_{gr}(normalized by ω_0) of beam-Weibel instability as function of wave number k (k is normalized by $(c/\omega_0)^{-1}$) for two set of parameters (I) $v_{0b} = 0.9c$, $T_{0b} = T_{0p} = 0$ (cold beam-plasma system) (II) $v_{0b} = 0.9c$, $T_{0b} = T_{0p} = 0.1$ keV (warm beam-plasma system). The plot, shown in Fig. 5.1, compares the growth rates of the cold beam-plasma system to the warm beam-plasma. We can see from Fig. 5.1, for cold system the Γ_{gr} increases with k for small values of k and saturates at $k \simeq 4$.
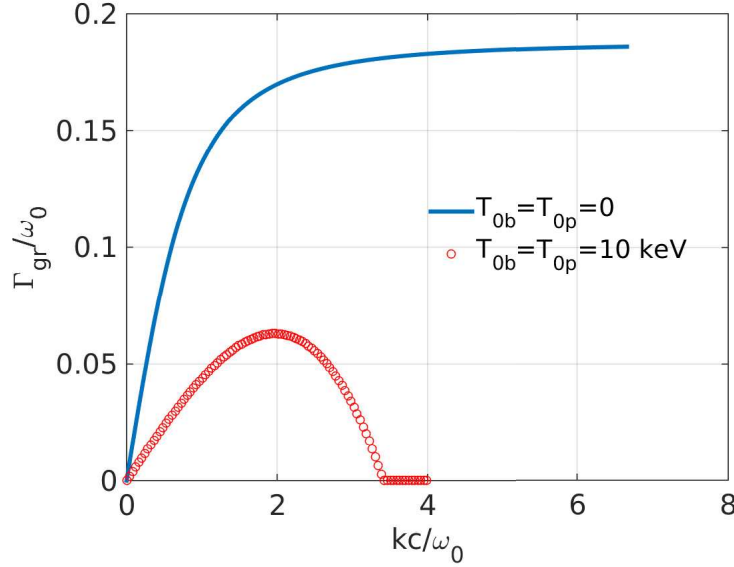
Figure 5.1: The growth rate of beam-Weibel instability as a function wave number k for cold beam-plasma and warm beam-plasma system. This plot shows the reduction in growth rate of instability for lower k and for higher k, it is completely suppressed in the case of warm beam-plasma system.

However, for the warm system Γ_{gr} increases with k for small values of k but starts decreasing after $k > 2$ and completely stabilizes at higher wave numbers ($k > 3.8$). The maximum growth rate $\Gamma_{gr}(max.)$ of warm system is also less compare to cold system.

In next section, we present the study of the linear and non-linear stage of beam-Weibel instability in this 2-D configuration by 2D PIC simulation.

5.3   PIC simulation

For simulation, we choose (y×z) Cartesian plane transverse to the beam propagation direction $\hat{x}$ with periodic boundary condition for both the electromagnetic field and charged particles in all direction. The area of the simulation box R is $12.5 \times 12.5 \ (c/\omega_0)^2$ corresponding to 256×256 cells where $c/\omega_0 = 5 \times 10^{-6} cm$. The time step is chosen by Courant condition and it is 0.003 fsec in this simulation. The total number of electrons and ions per cell are 32 each. The background plasma

electrons flow opposite to the beam with a velocity of v_{0p}. The ions have mass and charge of a proton, and we keep them at rest during the simulation. The quasi-neutrality is maintained in the system by choosing equal number of electrons and ions uniformly distributed in space and the current neutrality is also ascertained by choosing appropriate conditions for the velocity and the density of background electrons. The uniform plasma density n_0 is taken as $1.1 \times 10^{22} cm^{-3} (10 n_c)$ and the ratio of electron beam density to background electron density is chosen as $n_{0b}/n_{0p} = 1/9$. We record the evolution of box averaged field energy normalized by $B_{nor}^2 = E_{nor}^2 = (m_e c \omega_0/e)^2$ at each time step. The role of beam temperature on linear and nonlinear stage of beam-Weibel instability was investigated. We present here two cases with following parameters: (I) $v_{0b} = 0.9c$, $T_{0b} = T_{0p} = 0$ (II) $v_{0b} = 0.9c$, $T_{0b} = T_{0p} = 0.1$ keV.

5.3.1   Linear stage of beam-Weibel instability

The initial overlapping beam plasma current system is susceptible to the beam Weibel instability which causes the spatial separation of the forward and returns background currents. This increases the magnetic field in the system. The evolution of magnetic field energy with time for both run(I) and run(II) is shown in Fig. 5.2(a) where we can see the exponential growth of the magnetic field energy during initial stage and its saturation subsequently for both cases. The linear evolution of magnetic field energy is zoomed and shown in Fig. 5.2(b), the slope of which is utilized for the evaluation of growth rate in simulations. We find from the slope of the curve that the beam temperature suppresses the linear growth of beam-Weibel instability which is consistent with the observations of the linear analysis of kinetic beam-Weibel instability. The maximum linear growth of beam-Weibel instability estimated by theory and calculated from PIC simulation are compared in Table No.III. which shows there is a good agreement in theory and simulation.

TABLE III: The maximum linear growth rate of beam-Weibel instability calculated from kinetic theory and PIC simulation.

T_{0b}	T_{0p}	$\Gamma_{grAnal.}(\text{max.})/\omega_p$	$\Gamma_{grPIC}(\text{max.})/\omega_p$
0	0	0.18	0.16
0.1keV	0.1keV	0.06	0.07
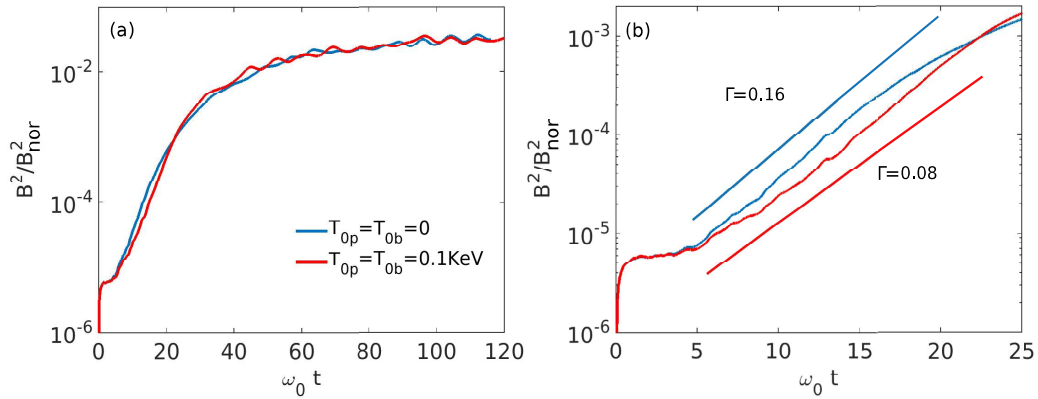
Figure 5.2: Time evolution of magnetic field energy (a) cold system (blue curve),warm system (red curve) (b) the zoom of the linear regime in which we can see the reduction in growth rate of instability for warm system compare from that of the cold system

The spatial distribution of magnetic field ($B = \sqrt{B_z^2 + B_y^2}/B_{nor}$) has been shown in Fig. 5.3 at time $\omega_0 t = 17.6$ for both cold and warm beam-plasma system. As predicted by kinetic theory, we can observe the formation of magnetic field structure of the order of skin depth (c/ω_{0p}) for the cold system (run(I)) while for warm beam-plasma system (run(II)) the structures are somewhat of longer scale. It turns out that here they correspond to about 1.5 times skin depth. The amplitude of the magnetic field in the warm case is observed to be smaller compared to the cold system in Fig. 5.3.

5.3.2   Non-linear dynamics of beam-Weibel instability

The magnetic field energy saturation at later times is observed in Fig. 5.2 due to non-linear interaction. After the linear phase of instability, the current filaments which flow in the same direction attract each other while opposite flowing current filaments repel to each other. In this non-linear regime of beam-Weibel instability, the filaments of the currents flowing in the same direction merge with each other and make a larger structure. It is believed that particles are trapped in the magnetic field of current filaments structure in non-linear regime, and it is the cause of the saturation of the field energy. The temporal evolution of x-component of current density in the z-y plane has been shown in Fig. 5.4 for cold beam-plasma
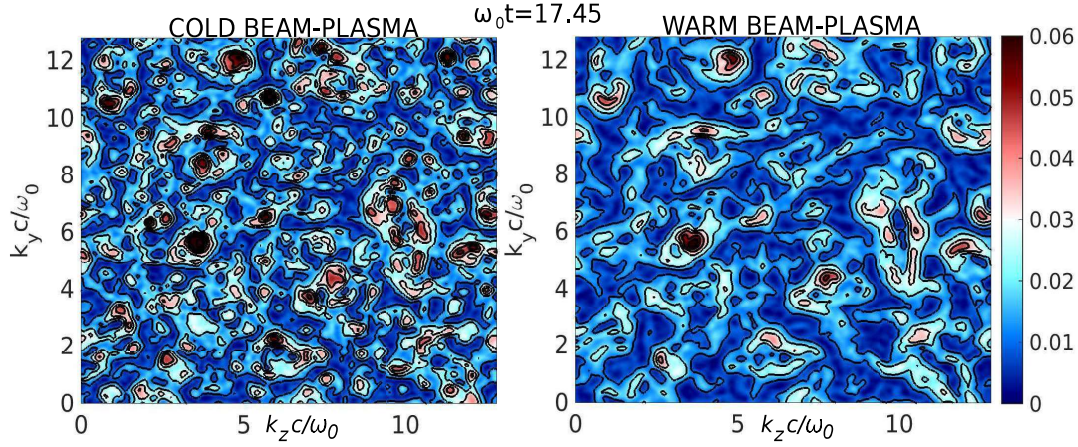
Figure 5.3: The spatial distribution of magnetic field ($B = \sqrt{B_z^2 + B_y^2}/B_{nor}$) at $\omega_0 t = 17.6$ for both cold and warm beam-plasma system.

system, and in Fig. 5.5 for warm beam-plasma system respectively. In Fig. 5.4, we can see the formation of small scale current filaments during the linear stage of instability ($\omega_0 t = 17.45$). The like sized current filaments merge with each other with time and organize as bigger current filament structures (shown in Figure 5.4 at $\omega_0 t = 52.36$). In the case of warm beam-plasma, lesser number of current filaments with reduced strength form during the linear phase (see Fig. 5.5 at time $\omega_0 t = 17.45$) which consistent with the theoretical result. In non-linear regime ($\omega_0 t = 52.36$), there does not appear much of a difference between cold and hot beam-plasma systems.

A rough saturation criteria of instability can be obtained by considering a model spatial profile of magnetic field in 2-D, mimicking the magnetic field of the current filaments. The amplitude of the magnetic field is chosen so as to significantly deflect the trajectory of an electron. The transverse motion of an electron in this magnetic field is given by

$$\frac{d^2 r}{dt^2} = \frac{e v_z}{m c \gamma_{0b}} B_0 sin(kr) \tag{5.14}$$

The bounce frequency of a magnetically trapped electron is given by

$$\omega_m^2 = \frac{e v_{0b} k B_0}{m_e c \gamma_{0b}} \tag{5.15}$$
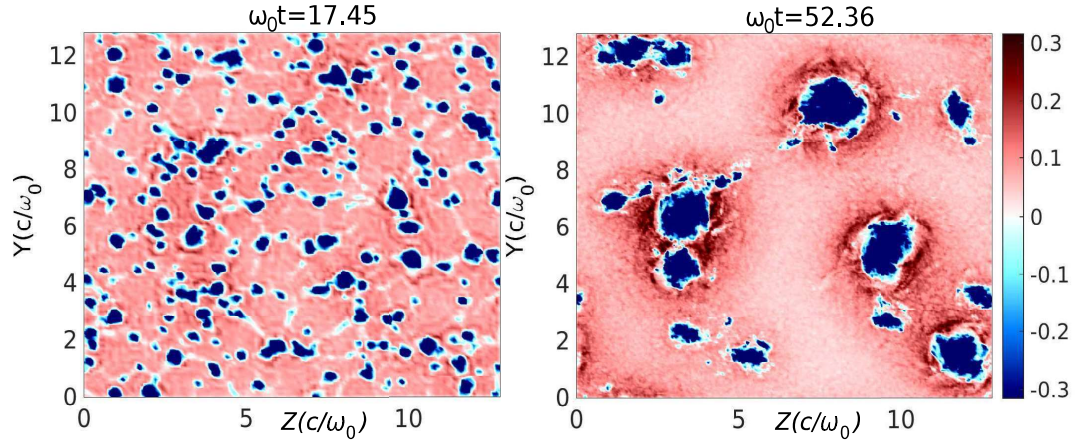
Figure 5.4: The spatial distribution of current density (J_x/n_0qc) at $\omega_0 t = 17.45$, 52.36 for cold beam-plasma system which shows the formation small scale current filaments in linear regime, and due to the merging of like current filaments, the larger structures of current filaments at time $\omega_0 t = 52.36$.

Roughly it can be assumed that the instability saturates at a point where bounce frequency becomes equal to the maximum linear growth rate of instability. Therefore, the saturated magnetic field B_{sat} can be estimated by comparing the linear growth of beam-Weibel instability to the bounce frequency ($\omega_m = \Gamma gr(max.)$). So, The saturated magnetic field is

$$B_{sat} \sim \left(\frac{m_e c \gamma_{0b}}{e v_{0b} k} \right) \left[\left(\frac{2\sqrt{6}}{9\sqrt{\pi}} \right)^2 \frac{[\omega_b^2 v_{0b}^2 m_e / T_b + \omega_b^2 (\gamma_{0b} - 1/\gamma_{0b}^3)]^3}{\left(\omega_p^2 (v_{0p}^2 + T_p/m_e)c \right)^2} \right] (T_p/m_e)^3 \quad (5.16)$$

From eq. (5.16), we get $B_{sat}/B_{nor} \sim 0.2$ for warm beam-plasma system, and from PIC simulation also, we get $B_{sat}/B_{nor} \sim 0.2$. Thus we see that the saturated magnetic field under this assumption matches well with the results of the PIC simulations.

In next section, we discuss the case of a 2-D geometry for which the beam propagates along one of its axis. In this geometry all the longitudinal and transverse instabilities can get excited.
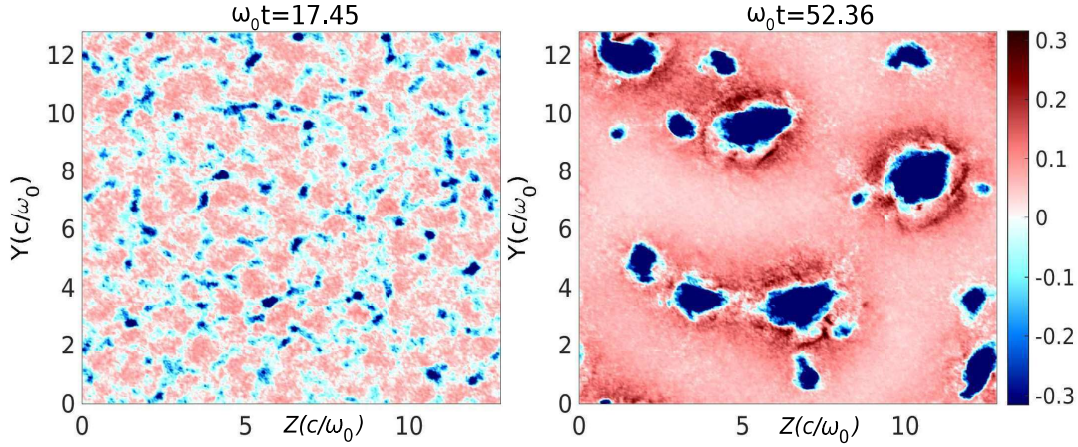
Figure 5.5: The spatial distribution of current density (J_x/n_0qc) at $\omega_0 t = 17.45$, 52.36 for warm beam-plasma system. In this we see less no. of current filaments than the cold beam-plasma system in the linear regime at time $\omega_0 t = 17.45$. However, there is no much difference in the non-linear regime ($\omega_0 t = 52.36$)

5.4   Case II: Beam propagation in the 2-D plane under consideration

We present theoretical and numerical study of beam-plasma system in two-dimensional spatial configuration, where beam flows along the 2-D plane under consideration. In this configuration all the longitudinal and transverse modes are permissible. Thus the coupling of beam-Weibel instability with two-stream (TSF) is possible. We explore the nature of this coupled TSF instability with two-fluid theory and with PIC simulation in uniform, as well as an inhomogeneous plasma with ripple in the background plasma density.

5.4.1   Analytical study of coupled two-stream filamentation instability in beam-plasma system

We consider a collision-less, quasi-neutral and un-magnetized electron beam- plasma system. The electron beam with density n_{0b}, and temperature T_{0b} drifts with velocity v_{0z} in the $\hat{z}$ direction inducing a return current with density n_{0p}, and velocity v_{0p} in cold background plasma electrons. We have considered both uniform as well as an inhomogeneous plasma density with a sinusoidal ripple in ion density

transverse to the propagation direction of the beam. The amplitude of the ripple is ϵ and the spatial variations are characterized by the wave number $k_s = 2\pi/\lambda_s$ as shown in the sketch of the system considered for this study in Fig. 5.6. We assume the ions having proton charge to be massive, thereby treat them as static neutralizing background. We use a two fluid description wherein the relativistic
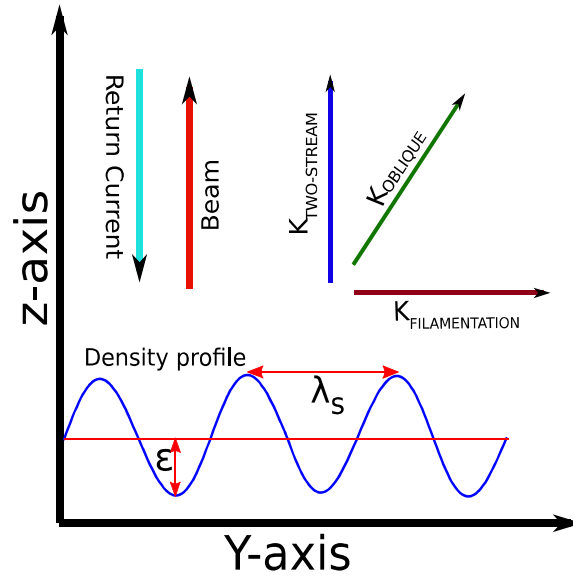
Figure 5.6: Schematic illustration of intense laser-solid interaction

electron beam (REB) and the background electrons are treated as separate fluids. This model can be realized by a set of coupled Maxwell equations with continuity and momentum equation. We have already derived a generalized set of coupled differential equations (4.9, 4.10) in presence of plasma inhomogeneity in transverse direction of beam propagation by the two fluid model in the linear regime in chapter 4. We use that generalized equations (4.9, 4.10) to study the linear response of the considered system. The equations (4.9, 4.10) in normalized (in chapter 4)

form are following:

$$\Omega_\alpha \gamma_{0\alpha}^3 v_{l\alpha z}'' + \left(\omega^2 - k_z^2\right)\Omega_\alpha \gamma_{0\alpha}^3 v_{l\alpha z} + \left(\omega^2 - k_z^2\right)\sum_\alpha \frac{n_{0\alpha}}{\Omega_\alpha} v_{l\alpha z}$$

$$+ \sum_\alpha \frac{k_z - \omega v_{0\alpha}}{\Omega_\alpha} n_{0\alpha} v_{l\alpha z}' = 0 \qquad (5.17)$$

$$\frac{(\omega^2 - k_z^2)}{\Omega_\alpha}\eta T_{0\alpha} v_{l\alpha y}'' + \left(\omega^2 - k_z^2\right)\Omega_\alpha \gamma_{0\alpha} v_{l\alpha y} - \Omega_\alpha \sum_\alpha n_{0\alpha} v_{l\alpha y}$$

$$+ \left(i\frac{k_z}{\Omega_\alpha}(\omega^2 - k_z^2)\eta T_{0\alpha} - i\left(k_z - v_{0\alpha}\omega\right)\Omega_\alpha \gamma_{0\alpha}^3\right)v_{l\alpha z}' = 0 \qquad (5.18)$$

For uniform beam-plasma system, the coupled equations (5.17, 5.18) reduce to the following :

$$k_y^2 \Omega_\alpha \gamma_{0\alpha}^3 v_{l\alpha z} - \left(\omega^2 - k_z^2\right)\Omega_\alpha \gamma_{0\alpha}^3 v_{l\alpha z} - \left(\omega^2 - k_z^2\right)\sum_\alpha \frac{n_{0\alpha}}{\Omega_\alpha} v_{l\alpha z}$$

$$-ik_y \sum_\alpha \frac{k_z - \omega v_{0\alpha}}{\Omega_\alpha} n_{0\alpha} v_{l\alpha z} = 0 \qquad (5.19)$$

$$k_y^2 \frac{(\omega^2 - k_z^2)}{\Omega_\alpha}\eta T_{0\alpha} v_{l\alpha y} - \left(\omega^2 - k_z^2\right)\Omega_\alpha \gamma_{0\alpha} v_{l\alpha y} + \Omega_\alpha \sum_\alpha n_{0\alpha} v_{l\alpha y}$$

$$+ \left(\frac{k_z}{\Omega_\alpha}(\omega^2 - k_z^2)\eta T_{0\alpha} - \left(k_z - v_{0\alpha}\omega\right)\Omega_\alpha \gamma_{0\alpha}^3\right)v_{l\alpha z} = 0 \qquad (5.20)$$

We obtain the linear dispersion relation for a uniform beam-plasma system, by solving the equations (5.19, 5.20) given by

$$\left(\omega^2 \varepsilon_{zz} - k_y^2\right)\left(\omega^2 \varepsilon_{yy} - k_z^2\right) = \left(\omega^2 \varepsilon_{yz} + k_z k_y\right)\left(\omega^2 \varepsilon_{zy} + k_z k_y\right), \qquad (5.21)$$

Where dielectric tensor elements ε_{yy}, ε_{zz}, ε_{yz}, and ε_{zy} are following,

$$\varepsilon_{yy} = 1 - \frac{in_{0\alpha}\Omega_\alpha}{\omega^2 \phi_\alpha}, \qquad (5.22)$$

$$\varepsilon_{zy} = -\frac{ik_y n_{0\alpha}}{\omega \phi_\alpha}\left(\frac{v_{0\alpha}}{\omega} + \frac{\Lambda_{\perp\alpha}}{k_y \psi_\alpha}\right), \qquad (5.23)$$

$$\varepsilon_{yz} = -\frac{in_{0\alpha}\Lambda_{\parallel\alpha}}{\omega\psi_\alpha\phi_\alpha} - \frac{in_{0\alpha}v_{0\alpha}k_y}{\omega^2\phi_\alpha}, \tag{5.24}$$

$$\varepsilon_{zz} = 1 - \frac{in_{0\alpha}}{\psi_\alpha} - \left(\frac{in_{0\alpha}\Lambda_{\parallel\alpha}k_y}{\omega\psi_\alpha\phi_\alpha} + \frac{in_{0\alpha}v_{0\alpha}k_y^2}{\omega\Lambda_{\perp\alpha}\phi_\alpha}\right)\left(\frac{v_{0\alpha}}{\omega} + \frac{\Lambda_{\perp\alpha}}{k_y\psi_\alpha}\right), \tag{5.25}$$

where $\Omega_\alpha = \omega - v_{0\alpha}k_z$, $\psi_\alpha = i\Omega_\alpha^2\gamma_\alpha^3 - in_{0\alpha}T_{\parallel\alpha}\eta k_z^2$, $\Lambda_{\parallel\alpha} = in_{0\alpha}T_{\parallel\alpha}\eta k_z k_y$, $\Lambda_{\perp\alpha} = in_{0\alpha}T_{\perp\alpha}\eta k_z k_y$, $\phi_\alpha = i\Omega_\alpha\gamma_\alpha - \frac{\Lambda_{\perp\alpha}}{k_z\Omega_\alpha\left(k_y + \frac{k_z\Lambda_{\parallel\alpha}}{\psi_\alpha}\right)}$, and η is the ratio of specific heat.

The linear evolution of inhomogeneous beam-plasma system is studied by choosing a sinusoidal form of the ion background density: $n_{0i} = n_0[1 + \varepsilon cos(k_s y)]$ where n_0 is constant normalized density, ε is ripple amplitude associated with the sinusoidal inhomogeneity in the density. The equilibrium beam and plasma density profile is taken as $n_{0b} = \beta_b n_0(1 + \varepsilon_b cos(k_s y))$, $n_{0p} = \beta_p n_0(1 + \varepsilon_p cos(k_s y))$. To maintain quasi-neutrality β_α satisfies $\sum_\alpha \beta_\alpha = 1$ condition. For simplicity, we choose $\varepsilon_b = \varepsilon_p = \varepsilon$ here. The suffix 0 indicates the equilibrium fields. The ripple being periodic along $'y'$ we choose all the perturbed quantities to have the form of $f_\alpha = \Sigma_j^{\dots,\pm2,\pm1,0} f_{\alpha j} e^{i((k_y + jk_s)y + k_z y - \omega t)}$. For small amplitude of ripple($\varepsilon < 1$), the terms corresponding to $j = 0, \pm1$ are the ones which are only retained. All higher order terms are neglected.

To evaluate the linear growth rate of oblique mode driven instability, we expand eq. (5.17) and eq. (5.18), and solve it by substituting for the Bloch wave function form of the perturbed fields in the periodic system. Retaining only the first order

terms, as mentioned earlier we obtain the following equations:

$$\Omega_\alpha \gamma_{0\alpha}^3 \left(\lambda^2 - k_d^2\right) v_{d\alpha z} + \lambda^2 \sum_\alpha \frac{\beta_\alpha}{\Omega_\alpha} v_{d\alpha z} + \lambda^2 \sum_\alpha \frac{0.5\varepsilon\beta_\alpha}{\Omega_\alpha} v_{\alpha z}$$

$$+i\sum_\alpha \frac{\zeta_\alpha}{\Omega_\alpha}\beta_\alpha k_d v_{d\alpha y} + i\sum_\alpha \frac{\zeta_\alpha}{\Omega_\alpha}0.5\varepsilon\beta_\alpha k_d v_{\alpha y} = 0 \qquad (5.26)$$

$$\Omega_\alpha \gamma_{0\alpha}^3 \left(\lambda^2 - k_o^2\right) v_{\alpha z} + \lambda^2 \sum_\alpha \frac{\beta_\alpha}{\Omega_\alpha} v_{\alpha z} + \lambda^2 \sum_\alpha \frac{0.5\varepsilon\beta_\alpha}{\Omega_\alpha} \left(v_{d\alpha z} + v_{a\alpha z}\right)$$

$$+i\sum_\alpha \frac{\zeta_\alpha}{\Omega_\alpha}\beta_\alpha k_o v_{\alpha y} + i\sum_\alpha \frac{\zeta_\alpha}{\Omega_\alpha}0.5\varepsilon\beta_\alpha k_o \left(v_{d\alpha y} + v_{a\alpha y}\right) = 0 \qquad (5.27)$$

$$\Omega_\alpha \gamma_{0\alpha}^3 \left(\lambda^2 - k_a^2\right) v_{a\alpha z} + \lambda^2 \sum_\alpha \frac{\beta_\alpha}{\Omega_\alpha} v_{a\alpha z} + \lambda^2 \sum_\alpha \frac{0.5\varepsilon\beta_\alpha}{\Omega_\alpha} v_{\alpha z}$$

$$+i\sum_\alpha \frac{\zeta_\alpha}{\Omega_\alpha}\beta_\alpha k_a v_{a\alpha y} + i\sum_\alpha \frac{\zeta_\alpha}{\Omega_\alpha}0.5\varepsilon\beta_\alpha k_a v_{\alpha y} = 0 \qquad (5.28)$$

$$\left(\frac{\lambda^2}{\Omega_\alpha\beta_\alpha}\eta c_\alpha k_d^2 - \lambda^2\Omega_\alpha\gamma_{0\alpha}\right) v_{d\alpha y} + \Omega_\alpha \sum_\alpha \beta_\alpha v_{d\alpha y} + 0.5\varepsilon\frac{\lambda^2}{\Omega_\alpha\beta_\alpha}\eta c_\alpha[k_d^2 - k_0(2k_0 - k_s)]v_{\alpha y}$$

$$+0.5\varepsilon\Omega_\alpha \sum_\alpha \beta_\alpha v_{\alpha y} + \left(k_z k_d\frac{\lambda^2}{\Omega_\alpha\beta_\alpha}\eta c_\alpha - \zeta_\alpha\Omega_\alpha\gamma_{0\alpha}^3 k_d\right) v_{d\alpha z} - 0.5\varepsilon\frac{\lambda^2}{\Omega_\alpha\beta_\alpha}\eta c_\alpha k_z k_0 v_{\alpha z} = 0 \;(5.29)$$

$$\left(\frac{\lambda^2}{\Omega_\alpha\beta_\alpha}\eta c_\alpha k_0^2 - \lambda^2\Omega_\alpha\gamma_{0\alpha}\right) v_{\alpha y} + \Omega_\alpha \sum_\alpha \beta_\alpha v_{\alpha y} + 0.5\varepsilon\frac{\lambda^2}{\Omega_\alpha\beta_\alpha}\eta c_\alpha[k_0^2 - k_d(2k_d + k_s)]v_{d\alpha y}$$

$$+ \quad 0.5\varepsilon\frac{\lambda^2}{\Omega_\alpha\beta_\alpha}\eta c_\alpha[k_0^2 - k_a(2k_a - k_s)]v_{a\alpha y} + 0.5\varepsilon\Omega_\alpha \sum_\alpha \beta_\alpha \left(v_{d\alpha y} + v_{a\alpha y}\right)$$

$$+ \quad \left(k_z k_0\frac{\lambda^2}{\Omega_\alpha\beta_\alpha}\eta c_\alpha - \zeta_\alpha\Omega_\alpha\gamma_{0\alpha}^3 k_0\right) v_{\alpha z} - 0.5\varepsilon\frac{\lambda^2}{\Omega_\alpha\beta_\alpha}\eta c_\alpha k_z \left(k_d v_{d\alpha z} + k_a v_{a\alpha z}\right) = 0 \qquad (5.30)$$

$$\left(\frac{\lambda^2}{\Omega_\alpha\beta_\alpha}\eta c_\alpha k_a^2 - \lambda^2\Omega_\alpha\gamma_{0\alpha}\right) v_{a\alpha y} + \Omega_\alpha \sum_\alpha \beta_\alpha v_{a\alpha y} + 0.5\varepsilon\frac{\lambda^2}{\Omega_\alpha\beta_\alpha}\eta c_\alpha[k_a^2 - k_0(2k_0 + k_s)]v_{\alpha y}$$

$$+0.5\varepsilon\Omega_\alpha \sum_\alpha \beta_\alpha v_{\alpha y} + \left(k_z k_d\frac{\lambda^2}{\Omega_\alpha\beta_\alpha}\eta c_\alpha - \zeta_\alpha\Omega_\alpha\gamma_{0\alpha}^3 k_a\right) v_{a\alpha z} - 0.5\varepsilon\frac{\lambda^2}{\Omega_\alpha\beta_\alpha}\eta c_\alpha k_z k_0 v_{\alpha z} = 0 \;(5.31)$$

where $\lambda^2 = (\omega^2 - k_z^2)$, $k_d = (k_y - k_s)$, $k_0 = k_y$, $k_a = (k_y + k_s)$ and $\zeta_\alpha = (k_z - v_{0\alpha}\omega)$.

Now, we study in detail the growth rate of the most unstable mode for the general case by using equations (5.26, 5.27, 5.28, 5.29, 5.30, 5.31). The growth rate

has been mapped in the parameter space of k_z and k_y for the uniform beam-plasma system in Fig. 5.7 for $n_{0b}/n_{0p} = 1/9$ or $n_{0b}/n_{0e} = 0.1$, $v_{0b} = 0.9c$, $v_{0p} = -0.1c$ and $T_{0b\perp} = 10 KeV$. This figure shows that for this particular set of parameters, the oblique mode with(k_y, k_z=(1.5,1)) has a maximum growth rate. Also, a narrow oblique strip of wave numbers extending up to $k_y = \infty$ is found to be unstable.
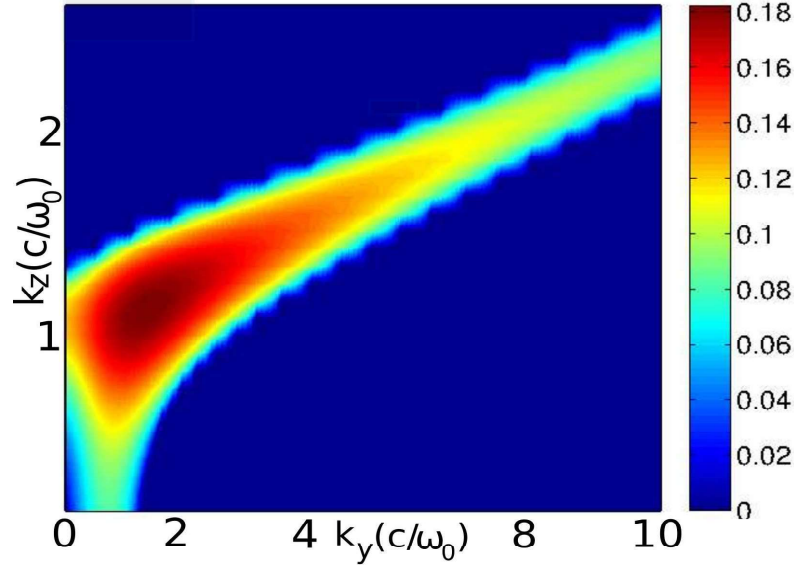
Figure 5.7: Growth rate map of the 2D oblique instability for a homogeneous beam-plasma at transverse beam temperature $T_{b0\perp}$=10 keV.

When the plasma density in chosen to be inhomogeneous and the scale length of the ripple is longer than the skin depth, i.e. $2\pi/k_s > c/\omega_0$ the growth rate of oblique mode driven instability is observed to increase with the amplitude ε of the inhomogeneity, as shown in Fig. 5.8 and 5.9. The unstable modes continue to stay around the oblique patch in the k_y vs. k_z plane. However, the growth rate is spread over a wider k_z domain compared to the uniform beam-plasma density case. Another feature is the appearance of several maxima along k_y in contrast to the single extrema for the uniform case. When the ripple scale length is sharper than the skin depth, i.e. for the case of $2\pi/k_s \leq c/\omega_0$, there is an overall reduction of the growth rates in the system in comparison to the uniform case. Furthermore, with increasing amplitude of density ripple also the growth rate reduces in this regime. This has been illustrated in the 2-D plot of the growth rate in Fig. 5.10 and 5.11. A detailed comparison of the growth rate Γ_{gr} of the maximally growing
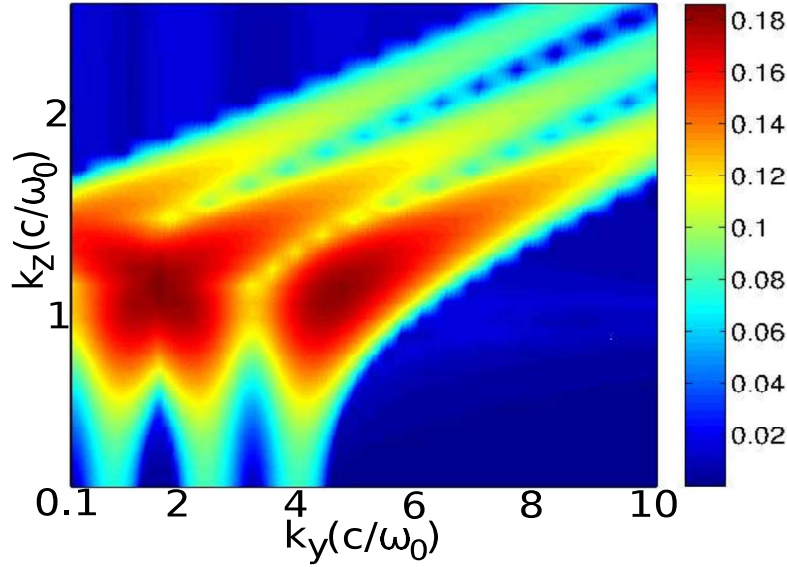
Figure 5.8: Growth rate map of the 2D oblique instability for a rippled beam-plasma at transverse beam temperature $T_{b0\perp}$=10 keV at $k_s = \pi$ and $\varepsilon = 0.1$.

mode for various different values of k_s and ε has been provided in TABLE IV.

TABLE IV

The maximum growth rate of oblique mode driven instability evaluated analytically under the approximation of weak ripple amplitude as well as from PIC simulation.

ε	k_s	Γ_{gr}(max.)	Γ_{pic}(max.)
0.0	0.0	0.1822	0.1823
0.1	π	0.1857	0.1827
0.1	2π	0.1811	0.1818
0.1	3π	0.1728	0.1813
0.2	π	0.1884	0.1830
0.2	3π	0.1475	0.1659
0.4	3π	0.1352	0.16

It is clear from the results that the growth rate drops when the amplitude, as well as the wave number of the plasma density ripple, is increased.
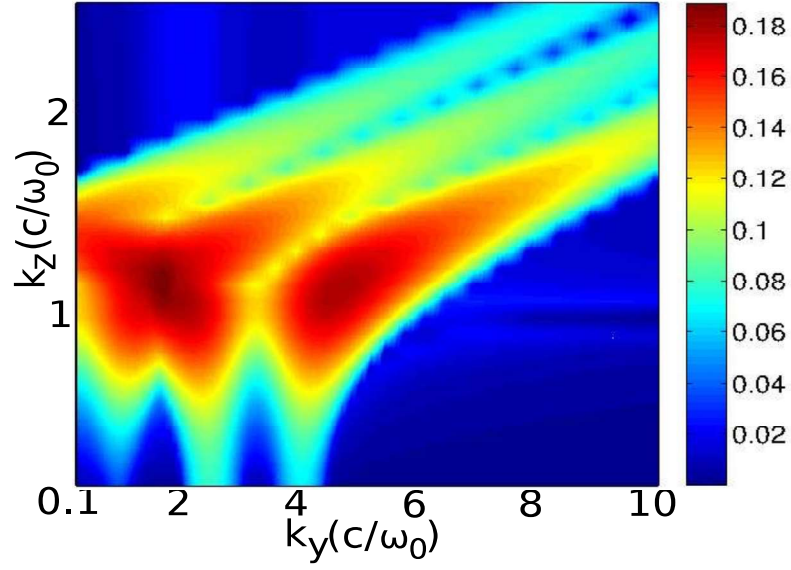
Figure 5.9: Growth rate map of the 2D oblique mode driven instability for a rippled beam-plasma at transverse beam temperature $T_{b0\perp}$=10 keV at $k_s = \pi$ and $\varepsilon = 0.2$.
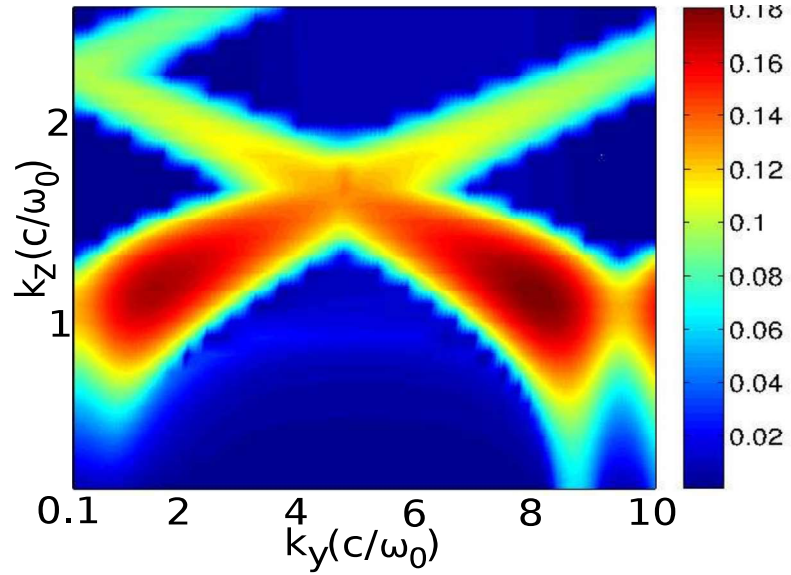
Figure 5.10: Growth rate map of the 2D oblique mode driven instability for a rippled beam-plasma at transverse beam temperature $T_{b0\perp}$=10 keV at $k_s = 3\pi$ and $\varepsilon = 0.1$.
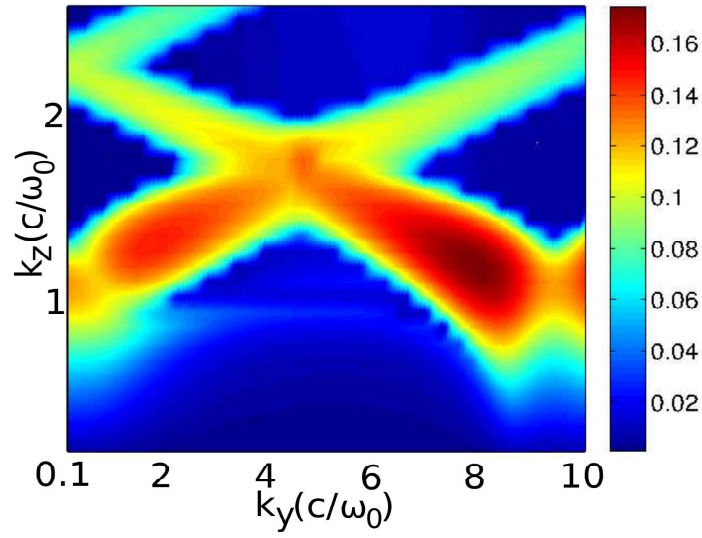
Figure 5.11: Growth rate map of the 2D oblique mode driven instability for a rippled beam-plasma at transverse beam temperature $T_{b0\perp}$=10 keV at $k_s = 3\pi$ and $\varepsilon = 0.2$.

5.5   PIC simulation

In this section, we present the results from the $2\frac{1}{2}$D PIC simulations employed for the beam-plasma. The simulation box is a Cartesian $y-z$ plane with periodic boundary condition for both the electromagnetic field and charged particles. The electron beam is chosen to propagate in the $\hat{z}$ direction with a relativistic velocity v_{0b} whose current is neutralized by the cold return shielding current from the background plasma electron flows in the opposite direction with a velocity v_{0p}. The respective densities are appropriately chosen for the current to be zero. Charge neutrality and a null current density are both ensured initially ($t = 0$). Thus, the system is field free and in equilibrium initially.

The electron beam has also been chosen to have a finite temperature T_{0b}. For the inhomogeneous plasma the pressure contribution in such cases has been avoided by choosing T_{0b} to be space dependent defined by eq. 4.8. The ions are kept at rest during the simulation. The uniform plasma density n_0 is taken as $10n_c$ where $n_c = 1.1 \times 10^{21} cm^{-3}$ is the critical density for 1μm wavelength of laser light. The area of the simulation box R is $30 \times 15\ (c/\omega_0)^2$ corresponding to 1500×750 cells where $c/\omega_0 = d_e = 5.0 \times 10^{-2}\mu$m is the skin depth. The total number of particles is 45000000 each for both electrons and ions. To resolve the underlying physics at the scale which is smaller than the skin depth, we have chosen a grid size of $0.02d_e$. The time step is decided by the Courant condition. The time evolution of the box averaged field energy density for every component of $\vec{E}$ and $\vec{B}$ are recorded at each time step. The energy density is normalized with respect to $(m_e c \omega_0/e)^2$ and time is normalized with respect to the electron plasma frequency ω_0. The results obtained from the simulation of the beam-plasma system for various amplitudes and scale lengths of the density inhomogeneity have been compared with the results of the uniform beam-plasma case. The initial choices of the parameters for simulation are taken as $n_{0b}/n_{0p} = 1/9$ or $n_{0b}/n_{0e} = 0.1$, $v_{0b} = 0.9c$, $v_{0p} = -0.1c$ and $T_{0b\perp} = 10KeV$. These parameters favor the growth of the oblique mode over the filamentation and two-stream modes. While considering the simulation of the rippled inhomogeneous density case, the ripple amplitudes ε is varied from 0.1 to 0.2. The ripple wave number is chosen as $k_s = \pi$, 2π and 3π for each of these amplitudes.

The perturbed field energies (magnetic as well as electric) are tracked in the simulation for the study of instabilities associated with the system. The rate of exponential growth of the perturbed energy provides for twice the growth rate of the fastest growing mode associated with the instability. The growth rates Γ_{pic}(max.), thus evaluated for different cases of simulations have been presented in one of the columns of TABLE IV.

The linear regime can be clearly identified from a log plot of total energy shown in Fig. 5.12. The region of the constant slope after an initial transient provides the
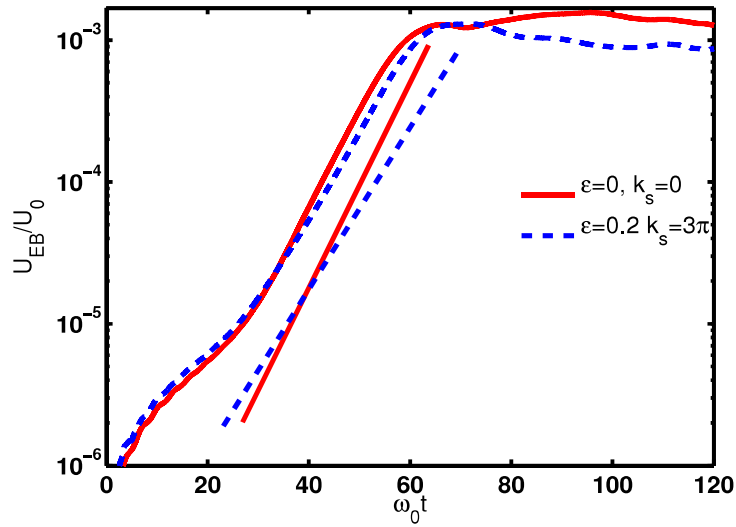
Figure 5.12: The plot on semilog scale of total perturbed normalized electromagnetic energy ($U_{EB} = E^2 + B^2$, $U_0 = B_{nor}^2$) for uniform and rippled($\varepsilon = 0.2$, $k_s = 3\pi$) density both. The growth rate calculated from PIC simulation by energy slope shows reduction for rippled beam-plasma system.

growth rate of the fastest growing mode. The straight line alongside represents the slope obtained from the linear theory provided in section II. It can be observed that the agreement between simulation and the theoretical linear results are remarkably good. The comparison also shows that the reduction in the growth rate in the presence of ripple in plasma density for scales sharper than the skin depth.

The separate evolution of the electric field energy density, and the magnetic field energy density for various simulation cases have been shown in Fig. 5.13 and Fig. 5.14 respectively. The energy associated with the electric field is observed to
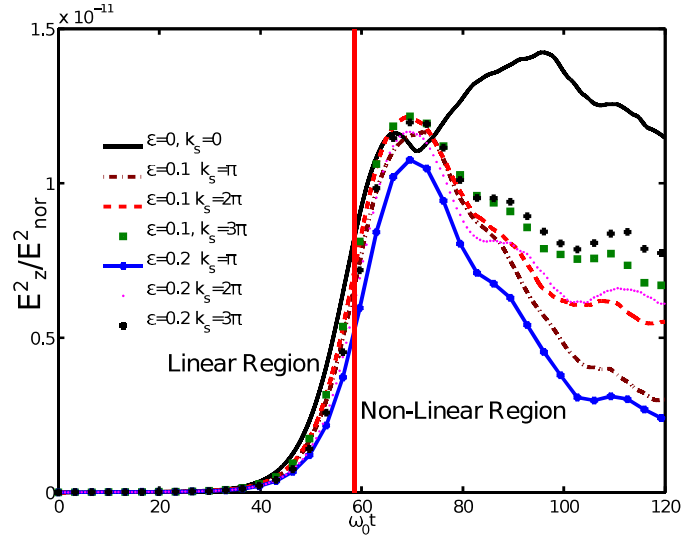
Figure 5.13: The evolution of z-component of normalized electric field energies E_z^2 with time for uniform beam-plasma system and rippled beam-plasma system cases. In non-linear stage, there is a huge drop in the electric field energy for rippled beam-plasma system.

be typically always higher than the energy in magnetic field. It is interesting to compare these perturbed energies in the nonlinear regime. While for the uniform density case the energy continues to remain high, there is a perceptible drop in both electric and magnetic field energies in the presence of inhomogeneity in the nonlinear regime. This has important significance as it suggests that the forward and reverse currents which got separated during the linear phase have a tendency to merge again for the inhomogeneous density when nonlinearity sets in the system.

The snapshot of the spatial profile in the $y - z$ plane of certain fields (B_s, n_b and n_p) at a time $\omega_0 t =$33, 53 and 90 have been shown in Figs. 5.15, 5.16 and 5.17 respectively. In these figures, the first column corresponds to the uniform density case, i.e. $\varepsilon = 0.0$ and second column to the inhomogeneous case with $\varepsilon = 0.2$ and $k_s = 3\pi$ (corresponding to density ripple scale lengths to be sharper than the skin depth). It is clear from these figures that the variations in these fields are in both 'y' as well as 'z' directions, confirming that the oblique mode continues to dominate the instability scene. However, it should also be noted that during the linear phase the magnetic field acquires structures which are extended and aligned
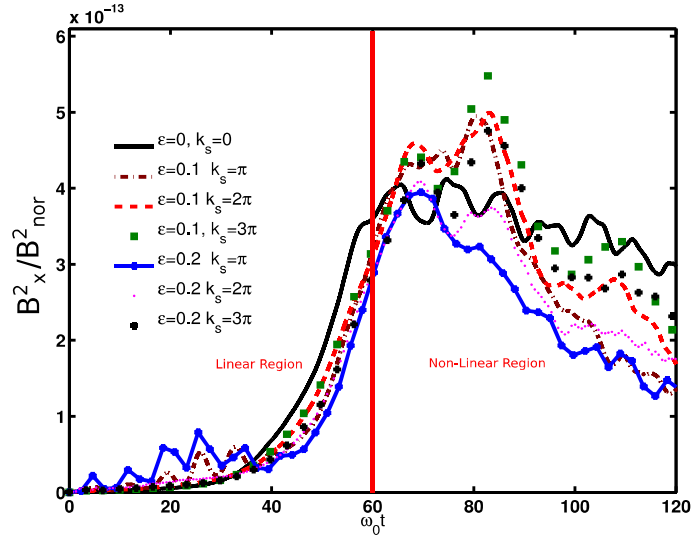
Figure 5.14: The evolution of x-component of normalized magnetic field energies B_x^2 with time for uniform and rippled cases.

along the beam flow direction of $\hat{z}$. The structure size along the y direction is significantly shorter and is found to compare with the typical values of the skin depth. Thus for the inhomogeneous case additional structures at scales shorter than the inhomogeneity scale are observed to ride over those appearing at the skin depth scale. These studies, therefore, suggest that specially tailored targets incorporating appropriate forms of plasma density inhomogeneity can lead to the suppression of the beam-plasma instabilities. Thus would be helpful for efficient transport of electron beam through plasmas.
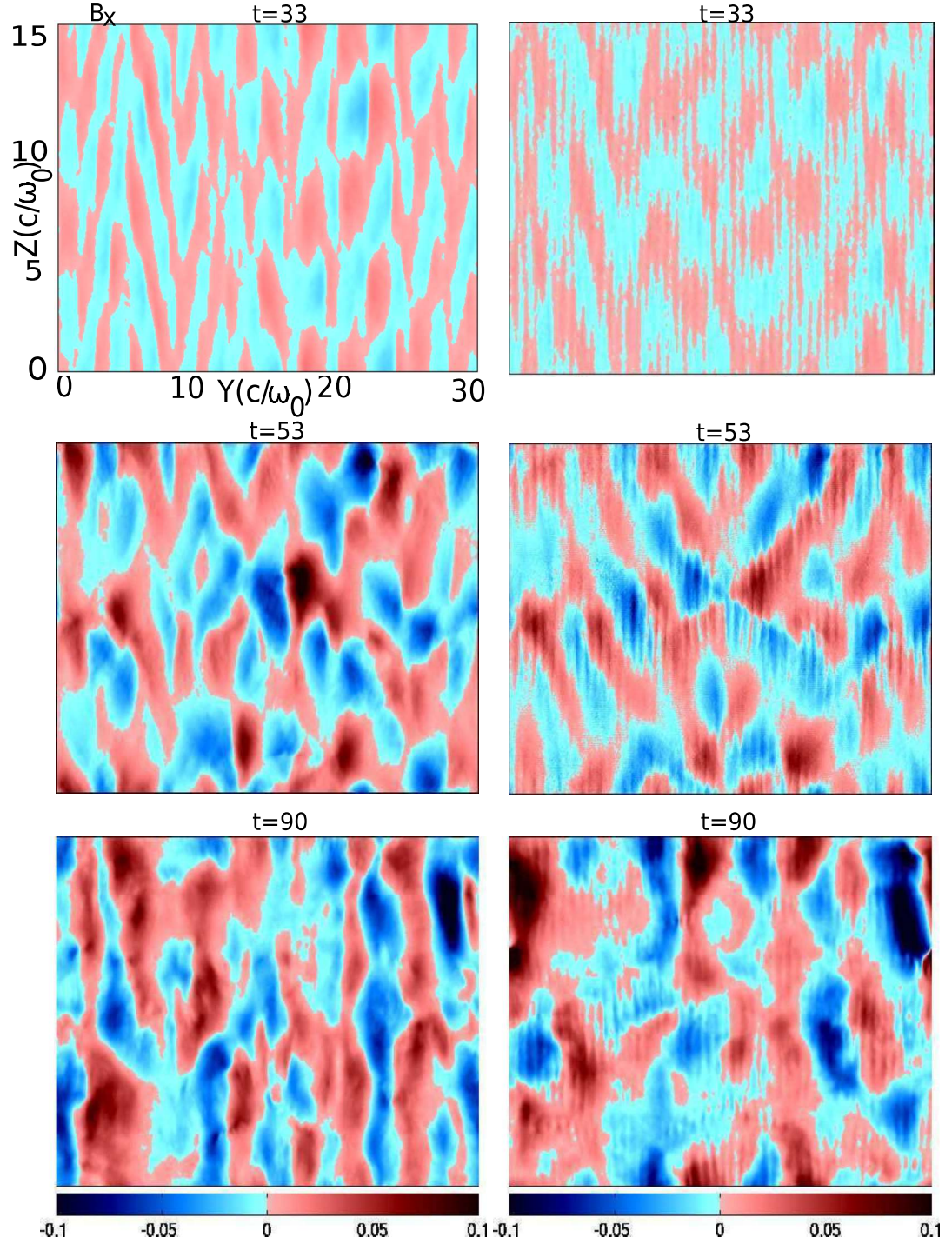
Figure 5.15: Time evolution and spatial configuration of x-component of magnetic field for uniform (first column) and rippled (ε=0.2 at k_s=3π, last column) case at time $\omega_0 t = 33$, $\omega_0 t = 53$ and $\omega_0 t = 90$.

Figure 5.16: Time evolution and spatial configuration of beam density for uniform (first column)and rippled (ε=0.2 at k_s=3π, last column) case at time $\omega_0 t = 33$, $\omega_0 t = 53$ and $\omega_0 t = 90$.

Figure 5.17: Time evolution and spatial configuration of background electron plasma density for uniform (first column)and rippled ($\varepsilon=0.2$ at $k_s=3\pi$, last column) case at time $\omega_0 t = 33$, $\omega_0 t = 53$ and $\omega_0 t = 90$.

5.6   Summary

In this chapter, we have considered the study of beam plasma system in 2-D in different geometrical configurations. In the first case, the 2-D plane of variations is orthogonal to the flow direction, whereas in the second the beam propagation lies in the plane of consideration. In the former configuration only the transverse beam-Weibel instability is permitted to get excited, while for the latter both transverse and longitudinal modes can be observed.

The linear growth rate of beam-Weibel instability have been obtained both analytically and from PIC simulation studies. A good agreement between the two has been observed. The linear regime of instability, clearly shows the spatial separation of the forward and return currents leading to the generation of large number of filaments. In the nonlinear phase, the growth of the magnetic field saturates as a result of the merging of like current filaments.

The coupling of two-stream instability with beam-Weibel/filamentation instability has also been studied in 2-D geometry by choosing the second configuration wherein the flow lies in the 2-D plane of study. The role of density inhomogeneity on the growth of these instabilities have also been explored both by fluid treatment as well as by the PIC runs. It is shown that the growth rate obtained from both approaches are similar. A quantitative comparison of the growth rate of the maximally growing mode for the uniform density case with that of the inhomogeneous one shows that the growth rate reduces in the presence of density inhomogeneity for scales which are sharper than the skin depth. The detailed PIC simulations in 2-D have also been performed which confirms this.

6

Kelvin-Helmholtz instability for sheared electron flows

Electron velocity shear can arise in many physical situations. In fact, a finite size electron beam propagation in plasma would introduce sheared flow at the edges. Furthermore, the configuration resulting after Weibel separation, of forward and return shielding currents of the energetic electron beam propagation in plasma, has a sheared electron flow configuration. It is well known in fluids that a sheared flow is susceptible to Kelvin - Helmholtz instability. The characteristic features of the instability have distinctions for the magnetized electron fluid flow [58]. In the relativistic case, some new additional features arising through sheared relativistic mass are also evident [6].

Some fluid simulation studies based on simplified Electron Magnetohydrodynamic (EMHD) model have been done to understand the instability in its nonlinear regime [7, 59, 88, 89]. In this chapter, we present the two-dimensional particle-in-cell simulations of a 2-D sheared electron flow configuration against a neutralizing background of ions. We simulate cases of the weak, mild, and strongly relativistic flow velocities. In the weakly relativistic case, we observe the development of electromagnetic Kelvin-Helmholtz instability with similar characteristics as that predicted by the electron Magnetohydrodynamic (EMHD) model. On the contrary, in a strong relativistic case, the compressibility effects of electron fluid dominate and introduce upper hybrid electrostatic oscillations transverse to the flow which are very distinct from EMHD fluid behavior. In the nonlinear regime, all three cases (weak, mild and strong relativistic) lead to turbulence with broad power law

spectrum.

6.1   Introduction

The fundamental physical processes, which govern the evolution of electron flows with velocity gradient, are of great interest in wide range of research areas in the astrophysical and laboratory contexts. In the astrophysical scenario, the relativistic jets, which are observed across a wide range of astrophysical scales from micro-quasars to Gamma Ray Bursts (GRBs), supernovas etc., [90–93] would have sheared flow of electrons.

In laser plasma experiments also, there are many situations where the sheared electron flow configuration is inevitable. For instance experiments on the fast-ignition scheme of laser-driven inertial confinement fusion involve electron beam propagation inside a plasma which would invariably result in a sheared configuration of electron flow [94]. The shear flow generation in the fast ignition context can be understood by the following description. When a high-intensity laser irradiates a solid surface and/or a compressed plasma it generates electron beam at the critical density surface of the plasma by the wave breaking mechanism [36, 95, 96]. This beam typically propagates inside the high-density region of the plasma exciting reverse shielding background electron currents. In the previous chapter 5, we have shown that the forward and reverse currents spatially are separated by Weibel instability. This separation leads to a sheared electron flow configuration. In addition to this, since the transverse extent of the beam is finite compared to the plasma width, being commensurate with the laser focal spot, the sheared configuration of electron flow automatically exists between the beam and the background stationary electrons at the edge of the propagating beam [97] even before Weibel destabilization process gets to generate sheared electron flow in the bulk region of the beam. Thus, the Kelvin-Helmholtz (K-H) instability develops immediately at the edge of the beam and does not require a Weibel destabilization process to preempt it.

The K-H instability is a well-known instability and has been widely studied in the context of hydrodynamic fluid. However, the sheared-electron velocity flow encountered in the laboratory and astrophysical cases, mentioned above, differs

from the hydrodynamic fluid flows in many respects. For instance, the sheared-flow configuration of electron fluid invariably has associated currents and they may often have a sheared current configuration as well. Consequently, the evolution of the magnetic field associated with it becomes an integral part of the dynamics. Development of charge imbalance is another aspect in the evolution. Though the equilibrium charge balance is provided by the neutralizing static background of ions, compressible electron flow during evolution can easily lead to charge imbalance as the ions would not respond on fast electron time scale phenomena. This would lead to electrostatic field generation which has added influence in the dynamics. Lastly, the flow of electrons in most cases is relativistic. Thus, to summarize the K-H instability, in this case, has additional effects due to the presence of electromagnetic features, compressibility leading to electrostatic fields, and features associated with relativistic flows. In the non-relativistic limit, the electromagnetic effects on K-H instability in the context of sheared electron flows have been investigated in detail by employing the Electron Magnetohydrodynamic (EMHD) model [7, 98, 99]. This model neglects the displacement currents and space charge effects and assumes stationary ions which provide the neutralizing background. The relativistic effects on K-H instability, in compressible neutral hydrodynamic fluid, has been studied by P. G. Drazin and W. H. Reid [100] and G. Bodo, A. Mignone, and R. Rosner [101]. Recently, [6] Sundar and Das have incorporated relativistic effects on sheared-electron flows. This study points out the crucial role of shear on the relativistic mass factor due to sheared velocity configuration. The effect due to displacement current was retained in the relativistic regime. It was, however, shown that for the weakly relativistic case the effects due to displacement current were negligible. However, in these studies, the space charge effects which may arise when compressibility of the electron fluid are present, was incorporated. The present chapter aims at exploring these features using a PIC simulation.

We have carried out a 2.5D relativistic electromagnetic Particle-in-Cell simulations to study the electron shear flow instability in both cases of weak as well as strong relativistic flows. By 2.5D we mean that all three components of the fields are taken into consideration, however, their spatial variations are confined in a 2-D plane only. When the flow is weakly relativistic, we observe the development of electromagnetic K-H instability at the location of shear which ultimately develops into vortices. These vortices merge subsequently forming longer scales,

in conformity with the inverse cascade phenomena observed in typical 2-D fluid systems. The density perturbations are observed to be weak in this case. The results, in this case, are thus very similar to the predictions of the EMHD fluid behavior. When the relativistic effects are mild (but not weak), the K-H instability occurs at a slower time scales. The K-H vortices are observed initially, which are soon overwhelmed by compressibility effects which introduce magnetized nonlinear electrostatic oscillations (nonlinear upper hybrid oscillations) in plasma transverse to flow. In strongly relativistic regime the electrostatic oscillations dominate right from the very beginning. The amplitude of the oscillations increases leading to phenomena of wave breaking. In the nonlinear regime, the spectra are observed to be broad in all the three cases which imply turbulence.

The chapter is organized as follows. In section II, we describe our simulation methodology. The results of PIC simulations and their implications are presented in section III. It is seen that in strong relativistic case compressibility effects seem to dominate resulting in electrostatic oscillations transverse to the flow. These electrostatic oscillations are understood on the basis of a simplified one-dimensional model in section IV. Section V contains the description of the power spectrum of the fields in the nonlinear regime. Section VI contains the summary and conclusions.

6.2   Simulation set-up

We choose the electron to have a flow velocity along $\hat{z}$ direction with a following sheared flow configuration (double tangent hyperbolic profile) as in equilibrium

$$V_{0z}(y) = V_0 \left[tanh((y - L_y/4)/\epsilon) + tanh((3L_y/4 - y)/\epsilon) \right] - V_0, \qquad (6.1)$$

where ϵ is the width of the shear layer, L_y is the total length of the simulation box in the transverse direction of flow and V_0 is the maximum amplitude of the flow velocity. This flow structure is shown schematically in Fig. 6.1. The electron flow is responsible for current and produces an equilibrium magnetic field B_0 in the $\hat{x}$ direction. During the simulations, ions are kept at rest and provide for the neutralizing background. In order to satisfy the condition for equilibrium force balance on electrons, there is a need to displace the electrons and ions slightly in space, so that an equilibrium electric field $\vec{E_0}$ gets created. This is chosen in such
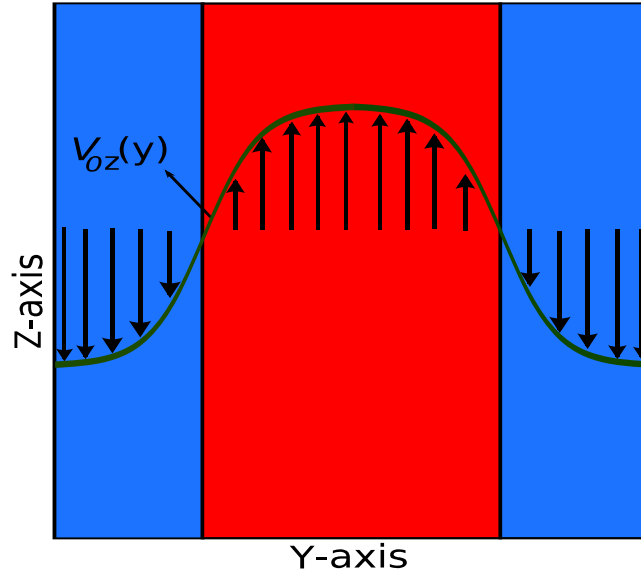
Figure 6.1: The schematic of the system used in the present chapter. Initially, electrons flow in z-direction with double tangent hyperbolic (along the y-axis) with shear width ε.

a fashion so as to satisfy the condition of

$$\vec{E}_0 + \frac{V_{0z}\hat{z} \times \vec{B}_0\hat{x}}{c} = 0 \tag{6.2}$$

This ensures that the Lorentz force on electrons vanishes everywhere. This clearly indicates the necessity for having an equilibrium electric field along $\hat{y}$. The electron and ion charge are thus displaced in an appropriate fashion so as to satisfy the Gauss's law

$$\nabla.\mathbf{E} = \frac{\partial E_y}{\partial y} = -\frac{1}{c}\frac{\partial (B_{0x}V_{0z})}{\partial y} = 4\pi e\left(n_{0i} - n_{0e}\right), \tag{6.3}$$

here n_{0i} and n_{0e} are unperturbed ion and electron number densities respectively in equilibrium, e is the charge of an electron and c is the speed of light. To maintain equilibrium in the system, we have thus arranged the electron particle number density according to the following relationship [102],

$$n_{0e} = n_{0i} + \frac{1}{4\pi ec}\frac{\partial (B_{0x}V_{0z})}{\partial y}. \tag{6.4}$$

The ions are distributed uniformly with a density n_{0i} of $3.18 \times 10^{18} \text{cm}^{-3}$ and n_{0e} is adjusted as per Eq. (6.4). The area of the simulation box R is chosen to be $6 \times 5 \ (c/\omega_{0e})^2$ corresponding to 600×500 cells; where $\omega_{0e} = \sqrt{4\pi n_{0i}e^2/m_e}$ is electron plasma frequency corresponding the uniform plasma at the background density of ions. Also, $c/\omega_{0e} = d_e = 3.0 \times 10^{-4} \text{cm}$ is the skin depth. We have used 128 particles per cell for both ion and electron in our simulation. To resolve the underlying physics at the scale which is smaller than the skin depth, we have chosen a grid size of $0.01d_e$. The time step Δt, decided by the Courant condition, is 0.035 femtosecond.

We have considered four different set of parameters for our investigation. In all cases, the velocity profile of electron is assigned by eq. 6.1. For the first case, we choose the flow velocity of the electron in the weakly relativistic regime and chose the shear width to be less than the plasma skin depth. We would refer this as Case (a) which has the following parameters $V_0 = 0.1c$, $\epsilon = 0.05 \ c/\omega_{0e}$. This is the weakly relativistic case where the EMHD fluid description is supposed to work pretty well. We consider the case (b) then to illustrate the dependence of K-H instability on shear width. We do this by changing the value of shear width in comparison to the skin depth. As per the EMHD description, the growth rate decreases when the shear width is shallow compared to the skin depth. Here, we have chosen $\epsilon = 1.5 \ c/\omega_{0e}$. In the third and fourth cases (c) and (d) a mild and strong relativistic limit with parameters $V_0 = 0.5c$, $\epsilon = 0.05 \ c/\omega_{0e}$ and $V_0 = 0.9c$, $\epsilon = 0.05 \ c/\omega_{0e}$ are respectively considered.

6.3   PIC simulation results

In the three subsections, we discuss the results of (I) Weakly relativistic (II) Mild relativistic (III) Strong relativistic cases.

6.3.1   I. Weakly relativistic

We choose a value of $V_0 = 0.1c$ for electron velocity to study the weakly relativistic case. We observe a destabilization of the sheared flow configuration. The instability is tracked by plotting the evolution of the perturbed kinetic energy(PKE) of the electrons in the system. This is shown in Fig. 6.2. The initial steep rise is
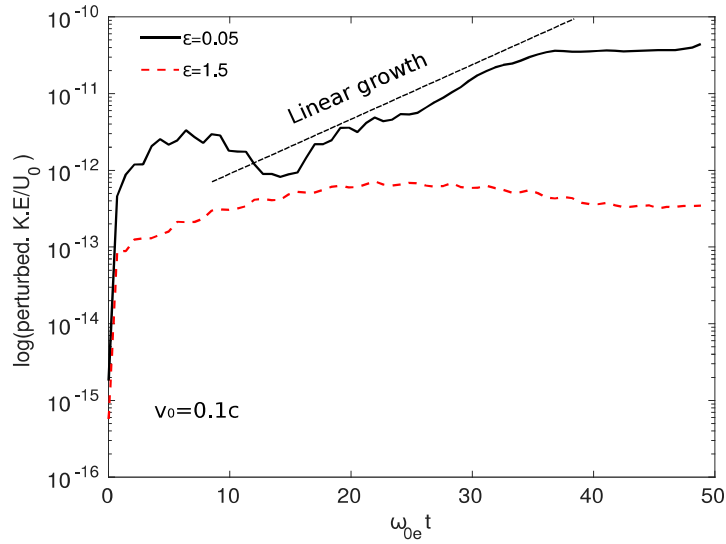
Figure 6.2: Time evolution of perturbed kinetic energy where $U_0 = (mec\omega_{0e}/e)^2$ for case (a) (black color, solid line) and case(b) (red color, solid line). The slope gives linear growth rate of KH instability.

due to numerical noise. Thereafter, the instability grows from the noise spectrum. Since, the initial noisy background would lack the exact eigenmode structure of any particular mode, a combination of unstable modes start growing initially. Subsequently, the mode with the fastest growth dominates, and a linear rise in the semilog plot of PKE with time can be clearly observed. It should be noted that evolution follows the EMHD fluid predictions of the growth rate being higher for the case (a) when the shear width is sharper than the skin depth. In case (b) the growth is observed to be small and the saturation also occurs quite fast.

For a closer look at the instability development, we show the color contour plot of the evolution of the magnetic field (Fig. 6.3)at various times. From (Fig. 6.3) the magnetic field evolution, one can observe that the magnetic perturbations start at the location where velocity shear is maximum and shows the KH vortices resulting from fastest growing mode m=5 at each shear layer with opposite polarity in x-component of magnetic field in linear stage of K-H instability. The perturbations grow to form magnetic vortices which subsequently merge to form bigger structures. The merging process of the magnetic field is along expected lines of 2-D inverse cascade EMHD depiction of the problem. We average the velocity of
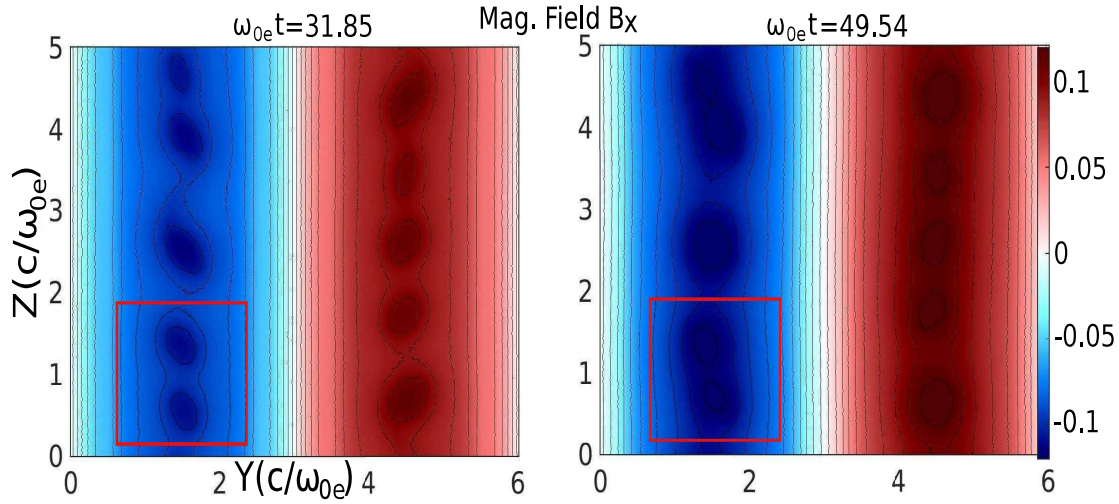
Figure 6.3:   Time evolution of x-component of the magnetic field $B_x = B_x/(mec\omega_{0e}/e)$ for the case (a) at time $\omega_{0e}t$=31.85 and 49.54. The vortices in the magnetic field are highlighted by red box (31.85 $\omega_{0e}t$) which merge at later time $\omega_{0e}t$=49.54 (highlighted by red box).

electron on the simulation grid and calculate the vorticity of the velocity field. The color plot of vorticity for the weakly relativistic case has been shown in Fig. 6.4 at various time. The fluid vorticity also shows similar traits, however, at later times $t = 59.60$ (in normalized units) the long scale vorticities show signs of disintegration. The vortices are eventually disrupted during nonlinear evolution of system and forming two turbulent layers. The spectral analysis of the turbulent electric and magnetic field are presented in section V. The snapshot of two components of electric field has been shown in Fig. 6.5 at various times. The two components of electric fields during evolution also show the emergence of K-H structures and the phenomena of merging. A comparison of normalized amplitudes of electric and magnetic field shows that the electric fields are much weaker than the magnetic fields. We also show the plot of electron density in the nonlinear regime of the K-H instability at $t = 36.75$ in Fig. 6.6. We observe that the density also acquires distinct structures of K-H like vortices in the shear region. The density perturbations, in the weakly relativistic case, are observed to be weak. The maximum observed value of $\tilde{n}_e/n_{e0} \sim 1.2$. On the other hand, we would see in the strongly relativistic case this is as large as 8 to 10. This suggests that in the weakly relativistic regime the instability essentially has an electrostatic character.
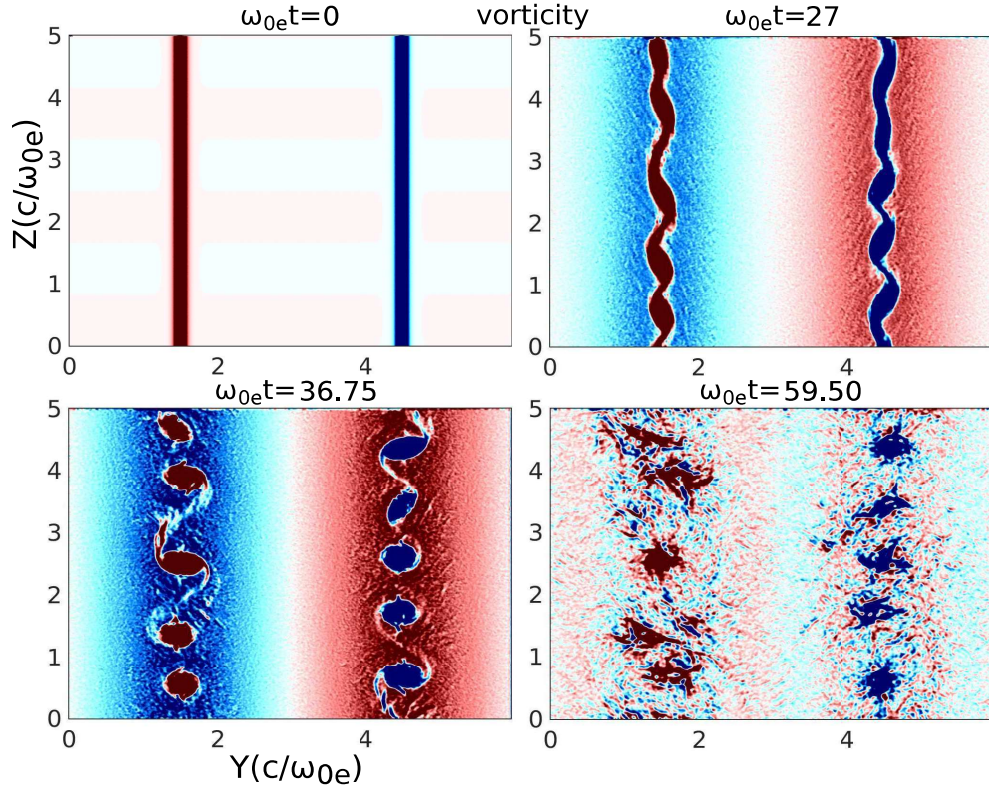
Figure 6.4: The time evolution of vorticity $((\nabla \times V)/\omega_{0e})$ calculated from velocity field for case (a) ($V_0 = 0.1c$, $\varepsilon = 0.05d_e$) which shows merging of vortices with time and turbulence stage of KH instability.

6.3.2   II. Mildly relativistic

In the mild relativistic case where $V_0 = 0.5c$, the K-H is observed to be considerably weak. The snapshots of vorticity have been shown in Fig. 6.7 at various time which show an initial tendency towards developing the K-H rolls.

The K-H rolls, in this case, are fewer in number. For case(a) they were 5 in number, here they are only around 3. This again suggests that the growth rate for relativistic case gets confined towards longer scale as per the predictions of EMHD model. The fluid analysis carried out earlier also suggests that the cut-off wavenumber of the K-H moves towards longer scales in mildly relativistic cases.

The K-H rolls are observed to be very soon overwhelmed by certain oscillations transverse to the flow. The oscillations, transverse to the flow, are also clearly
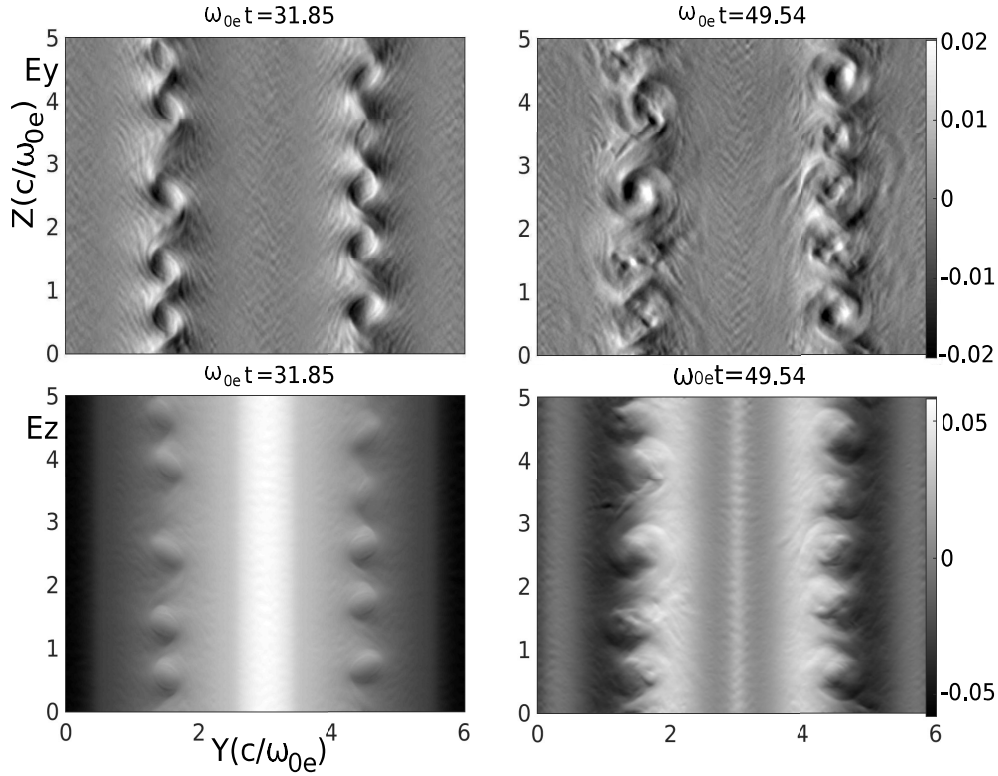
Figure 6.5: The time evolution of electric field: first row shows the y-component of electric field $E_y = E_y/(mec\omega_{0e}/e)$ and second row shows z-component of electric field $E_z = E_z/(mec\omega_{0e}/e)$ for case (a) ($V_0 = 0.1c$, $\varepsilon = 0.05d_e$.)

evident in the electron density plots of Fig. 6.8. The density oscillations, in this case, are pretty strong with $\tilde{n_e}/n_{e0} \sim 4$. The K-H suppression and the appearance of these upper electrostatic oscillations can be understood as follows. As the relativistic effect increases the $\vec{V} \times \vec{B}/c$ force becomes dominating. Thus a small perturbed magnetic field $\tilde{B}$, induces a strong $V_0 \times \tilde{B}/c$ force along y, which is responsible for the upper hybrid electrostatic oscillations.

6.3.3   III. Strong relativistic

We now choose $V_0 = 0.9c$ for understanding the strongly relativistic case. The time evolution of PKE, in this case, shows the linear growth of the instability. However, the instability is dominated by the upper hybrid electrostatic oscillations which are observed right from the very beginning. Thus the development of the rolls, typical
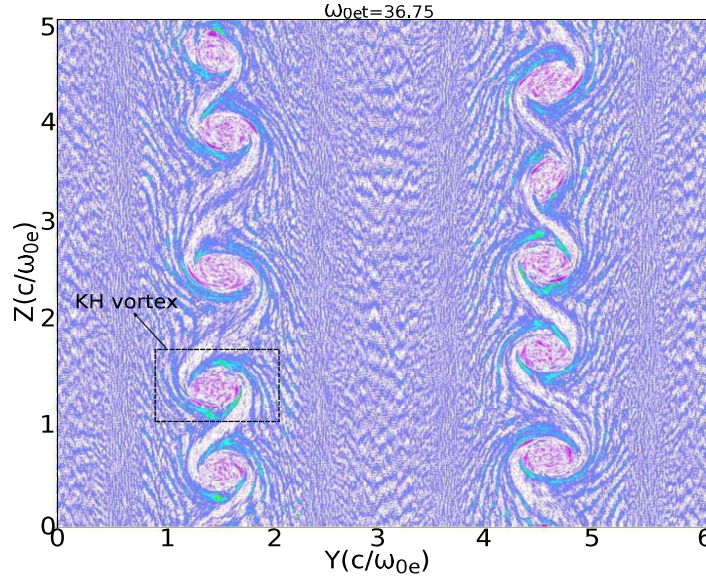
Figure 6.6: Formation of KH vortex (highlighted by black box) in electron density $n_e = n_e/n_{0i}$ at time $\omega_{0e}t =$ 36.75 for case (a).

of the K-H instability, is not very clearly evident in this case. Representing the initial distribution of flowing and the static electrons by different colors (red and blue respectively) we show the snapshots of their displacement in space in Fig. 6.9. The electron compressibility effects are clearly evident, wherein white regions totally devoid of electrons are created (snapshot at $\omega_{0e}t = 3.5$). The Electric fields due to background ions, however, pull these electrons back which results in a large amplitude excitation of nonlinear upper hybrid electrostatic plasma oscillations. These oscillations are discussed in detail in the next section.

A comparative value of the growth rate obtained from the slope of the evolution of PKE in the table below for all the cases studied by us has been provided.

TABLE V

The maximum growth rate ($\Gamma_{gr}max.$) of K-H instability evaluated from slope of perturbed kinetic energy
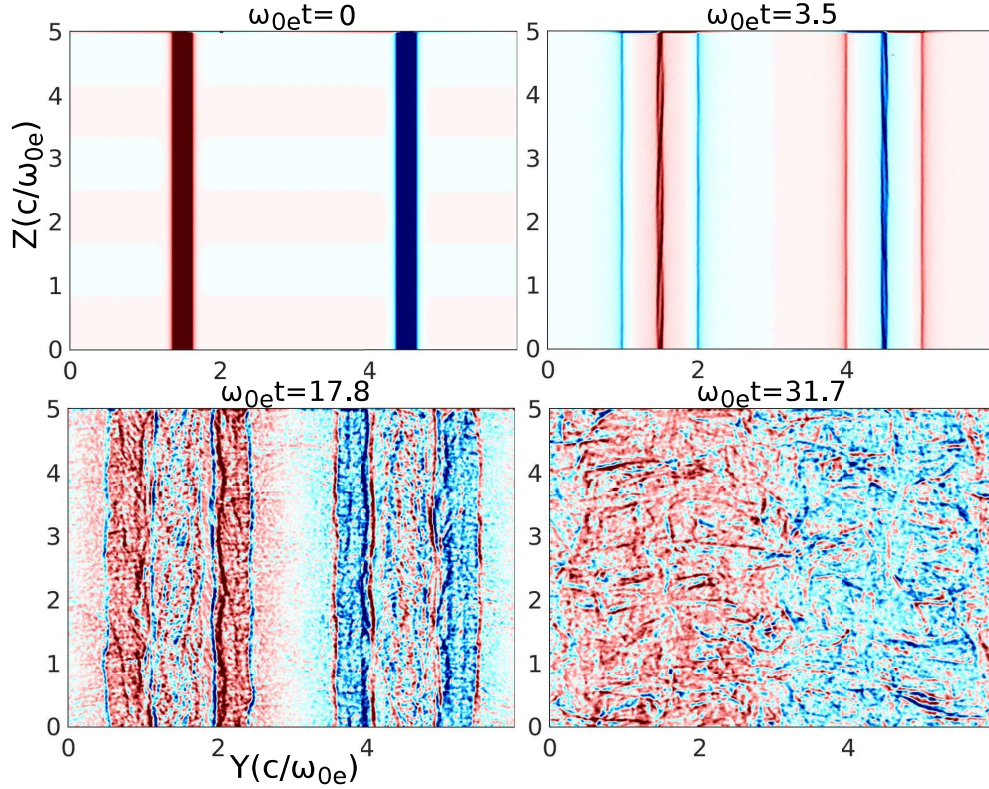
Figure 6.7: The time evolution of vorticity ($\nabla \times V$) calculated from velocity field for case (b).

V_0/c	$\varepsilon/(c/\omega_{0e})$	$\Gamma_{max}/(V_0\omega_{0e}/c)$
0.1	0.05	0.7
0.1	1.5	0.0
0.5	0.05	0.34
0.9	0.05	0.23

Since classically the K-H instability typically scales with the fluid flow velocity we have chosen to divide the growth rate with V_0 for a better appreciation of the comparison. The comparison clearly, shows that Γ_{max}/V_0 decreases due to relativistic effects in agreement with the earlier fluid analysis by Sundar and Das [6]. Thus the distinction between the PIC and EMHD fluid simulations finally boils down to the appearance and dominance of electrostatic oscillations, transverse to the flow direction. We study the physics of the transverse oscillations in detail in the next section.
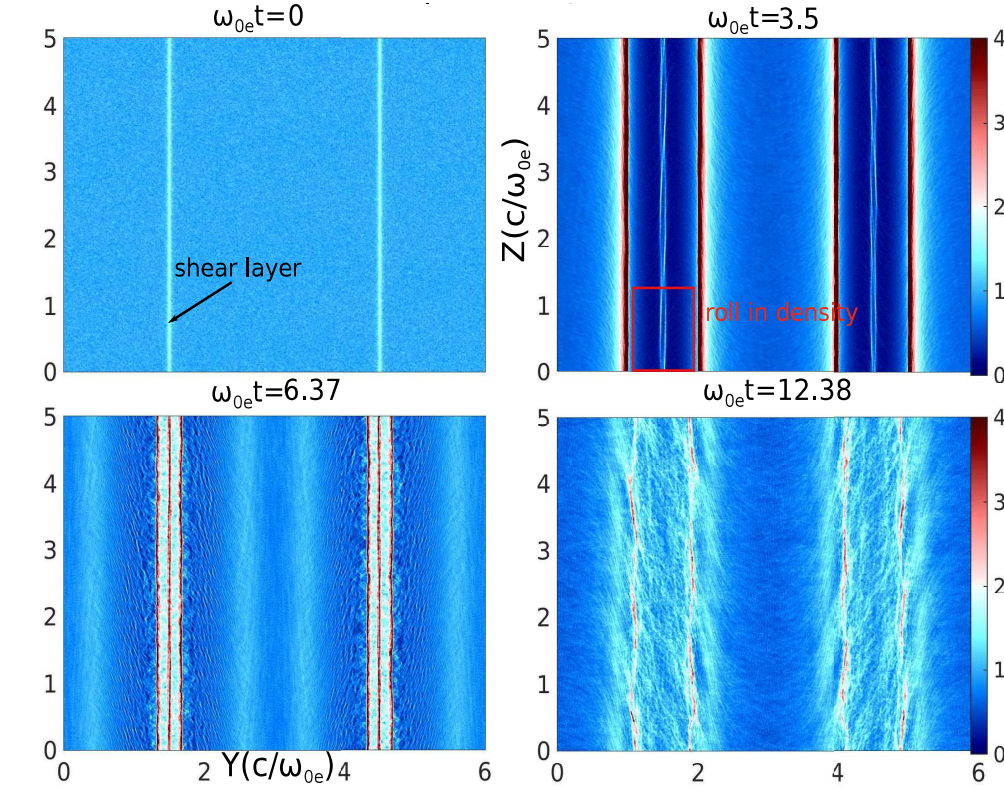
Figure 6.8: The time evolution of electron density $n_e = n_e/n_{0i}$ for case (c) that shows the roll in density at time $\omega_{0e}t=3.5$ at shear layer (highlighted by red box) which is a signature of KH instability. The compression and rare faction in density can be also seen.

6.3.4   IV. Nonlinear oscillation

One of the main observations is the appearance of strong upper hybrid electrostatic oscillations triggered from the edge of the flow region with increasing relativistic effects. We show in Fig. 6.10 the amplitude of these oscillations as a function of time at $z = 2.5$ c/ω_{0e} for the strongly relativistic case of $V_0 = 0.9c$. It can be seen that the density perturbations acquire a very high amplitude fairly rapidly $\tilde{n}_e/n_{e0} \sim 8$. This is a very nonlinear regime for the oscillations where wave breaking and trajectory crossing would occur. This is indeed so as the particle distribution of Fig. 6.9 shows clear crossing of blue and red electrons.

In order to understand the dynamics behind this phenomenon, we model the phenomena by a one-dimensional magnetized relativistic electron fluid equations
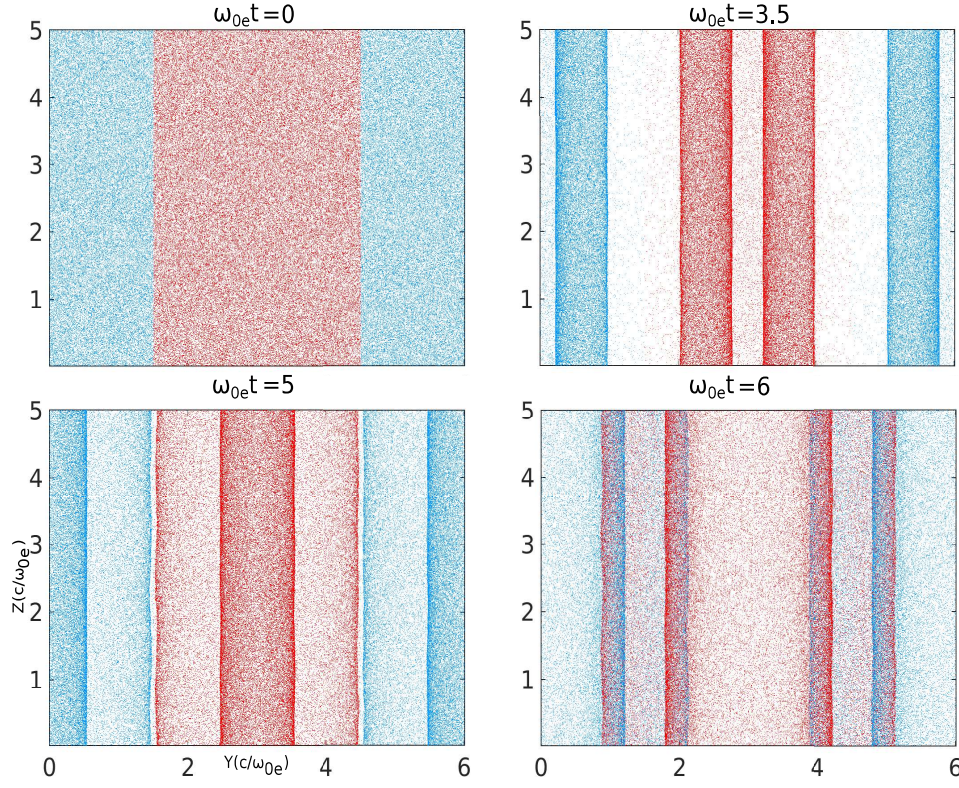
Figure 6.9: Particle picture of 2-D electron velocity shear configuration for case (d) which shows transverse oscillations of particles with time.

for electrostatic disturbances. Thus the governing equations of the model are expressed as

$$\left(\frac{\partial}{\partial t} + v_{ey}\frac{\partial}{\partial y}\right) n_e = -n_{ey}\frac{\partial v_{ey}}{\partial y}, \tag{6.5}$$

$$\left(\frac{\partial}{\partial t} + v_{ey}\frac{\partial}{\partial y}\right) p_{ey} = -eE_y - \frac{ev_{ez}B_0(y)}{c}, \tag{6.6}$$

$$\left(\frac{\partial}{\partial t} + v_{ey}\frac{\partial}{\partial y}\right) p_{ez} = \frac{ev_{ey}B_0(y)}{c}, \tag{6.7}$$

$$\left(\frac{\partial}{\partial t} + v_{ey}\frac{\partial}{\partial y}\right) E_y = 4\pi e n_{0i}v_{ey}, \tag{6.8}$$

$$\tag{6.9}$$

where $p_{e\alpha} = \gamma m_e v_{e\alpha}$ is α-component of momentum;α is subscript for y and z,
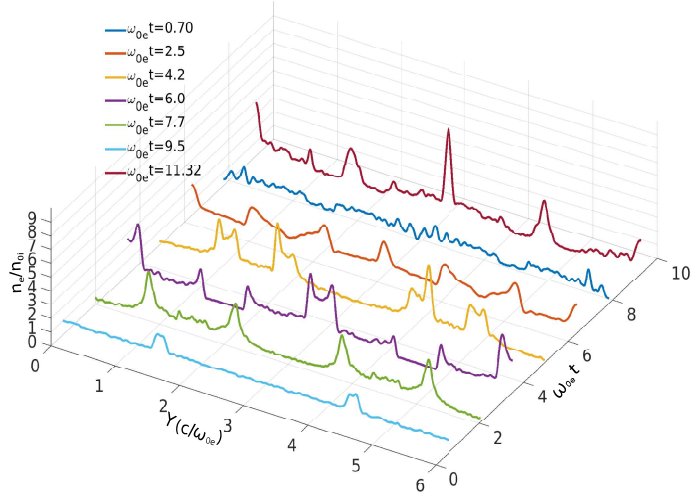
Figure 6.10: Time evolution of electron density diagnosed at y $= 2.5c/\omega_{e0}$ for $V_0 = 0.9c$, $\varepsilon = 0.05d_e$: This figure shows nonlinear large amplitude electrostatic oscillations which break in later time.

$\gamma = [1 + p^2/m_e^2 c^2]^{1/2}$ is the relativistic factor and n_{0i} is background ion density. The inhomogeneous magnetic field $B_0(y)$ is the equilibrium magnetic field generated from the equilibrium electron flow considered in our PIC simulations. For the double tangent hyperbolic profile, it will have the following form:

$$B_0(y) = \frac{4\pi n_{0e} e}{c} \left(V_0 \epsilon \log\left(\cosh\left(0.25 L_y - y\right)\right) + V_0 \epsilon \log\left(\cosh\left(y - 0.75 L_y\right)\right) - V_0 y \right).$$

$$(6.10)$$

We have solved the above equations numerically with the initial profile of v_{ez} using eq. (6.1). For the weakly relativistic case of $V_0 = 0.1c$ the electrostatic oscillations that get generated are quite small and continue to remain so indefinitely (See Fig. 6.11). However, when the value of V_0 is increased to a high value of $V_0 = 0.9c$, large-amplitude nonlinear oscillations in electron density (see Fig. 6.12) can be clearly seen. This is similar to the results of our PIC simulations.

The upper hybrid frequency ω_{UH} is given by

$$\omega_{UH}^2 = \omega_{0e}^2 + \omega_{ce}^2 \qquad (6.11)$$

109
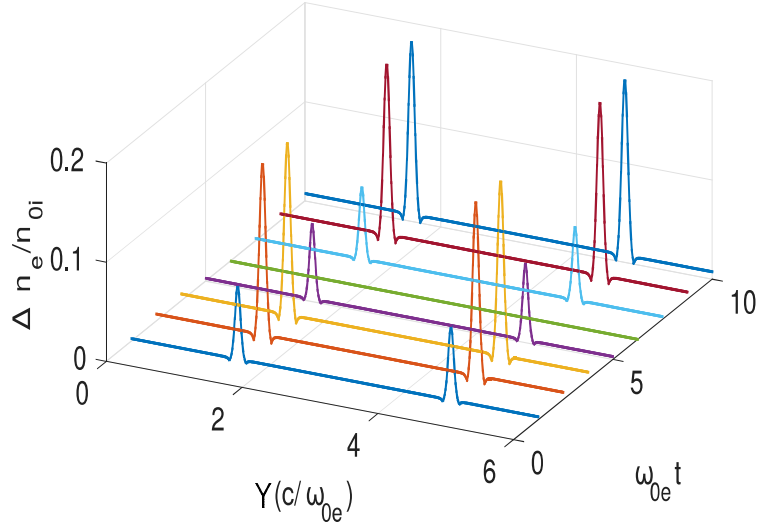
Figure 6.11: Time evolution of perturbed electron density $\Delta n_e = |(n_e - n_{e0})|$ obtained from 1D model diagnosed at y = $2.5c/\omega_{e0}$ for $V_0 = 0.1c$, $\varepsilon = 0.05d_e$:This figure shows small amplitude electrostatic oscillations in presence of inhomogeneous magnetic field B(y).

In our simulations, since the magnetic field is non-uniform, the upper hybrid oscillations occur against an inhomogeneous magnetic field background. For comparing the observed oscillation frequency with that of the upper hybrid oscillations we have chosen to consider an average magnetic field. Thus $\omega_{ce} = eB_{r.m.s}/m_e c$, $B_{r.m.s}$ is root mean square value of magnetic field. We calculate the upper hybrid frequency from dispersion relation eq. 6.11, from PIC simulation of ω_{UH} and from 1D model and have tabulated it in table II for the two cases of mild and strong relativistic flows. It can be seen that both approaches (simplified dispersion equation and 1 D model) yield comparable estimates for the observed electrostatic oscillations in the PIC simulations.

TABLE VI

The table for upper hybrid frequency obtained from dispersion relation eq. 6.11 $\omega_{UH}(anal.)$, from PIC simulation $\omega_{UH}(PIC)$ and from 1d model $\omega_{UH}(1d\ model)$ for various different value of V_0
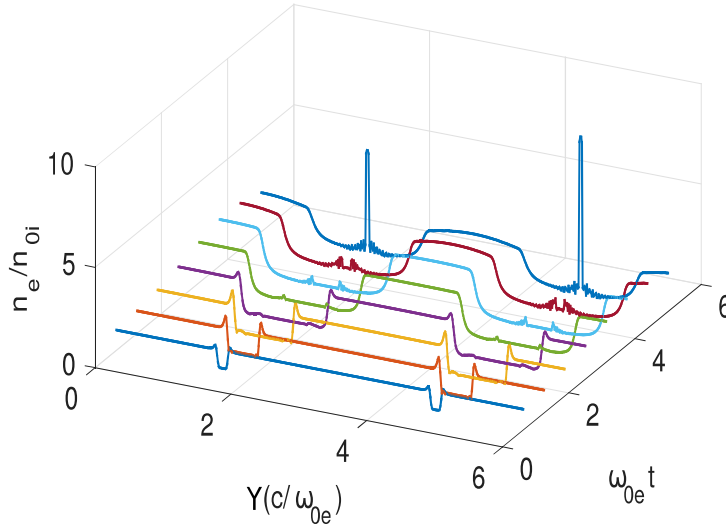
Figure 6.12: Time evolution of perturbed electron density n_e/n_{0i} obtained from 1D model diagnosed at z = $2.5c/\omega_{e0}$ for $V_0 = 0.9c$, $\varepsilon = 0.05d_e$: This figure shows nonlinear large amplitude electrostatic oscillations which break in later time.

V_0/c	$\omega_{UH}(anal.)/\omega_{0e}$	$\omega_{UH}(PIC)/\omega_{0e}$	$\omega_{UH}(\text{1d model})/\omega_{0e}$
0.5	1.09	1.06	1.06
0.9	1.27	1.26	1.25

This clearly shows that the observed electrostatic oscillations in PIC are the upper hybrid oscillations.

6.4   Spectral Analysis

The nonlinear regime of the simulation shows evidence of turbulence generation for both weak and strong relativistic cases. We have plotted the spectra of magnetic and electric fields as a function of k_z defined by the following relationship:

$$S_F(k_z) = \frac{1}{L_y} \int_0^{L_y} F^2(y, k_z) dy, \tag{6.12}$$

where $S_F(k_z)$ is one-dimensional longitudinal energy spectra of the field F where F is the y-dependent longitudinal Fourier transform of any field, (e.g. the electric

and magnetic fields represented by R below)

$$F(k_z, y) = \frac{1}{L_z} \int_0^{L_z} R(y, z) exp(-ik_z z) dz, \tag{6.13}$$

The resulting longitudinal energy spectra corresponding to x-component of magnetic field B_x, y-component of electric field E_y and z-component of electric field E_z are plotted in Fig. 6.13, Fig. 6.14(a) and Fig. 6.14(b) respectively for weak relativistic case at various time. At early time stage ($\omega_{0e}t=3.5$), there is com-
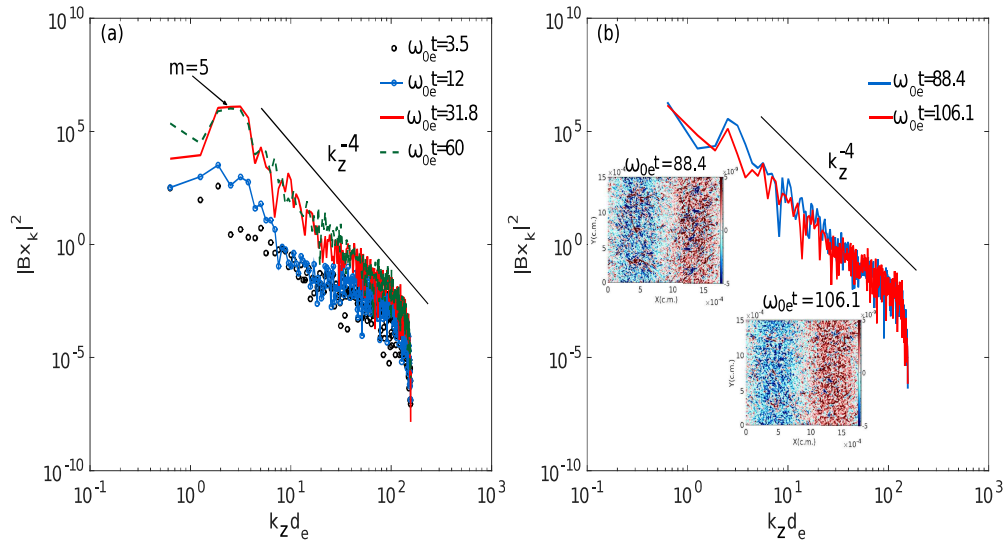
Figure 6.13: Longitudinal spectrum of magnetic field energy $|Bx_k|^2 = |Bx_k/(mec\omega_{0e}/e)|^2$ with time for case ($V_0 = 0.1c$, $\varepsilon = 0.05d_e$). (a) spectra of magnetic field up to linear stage (b) spectra in turbulent stage (inset show the vorticity at turbulent stage).

petition between perturbations so we do not observe dominating power on any particular scale but, as system evolve with time, we observe the domination of mode m=5 (where $k_z = 2\pi m/L_y$) after time ($\omega_{0e}t=31.8$) that is consistent with observation and confirming that appropriately 5 linearly unstable wavelengths are initially growing. At later time (Fig. 6.13 (b)), we have observed the peak diminish that means the energy of linear modes (m=5) are transferred to lower mode by merging or pairing the vortices. This indicates the inverse cascade.

The snapshots of vortices at time $\omega_{0e}t=88.4$, and $\omega_{0e}t=106.1$ have been shown
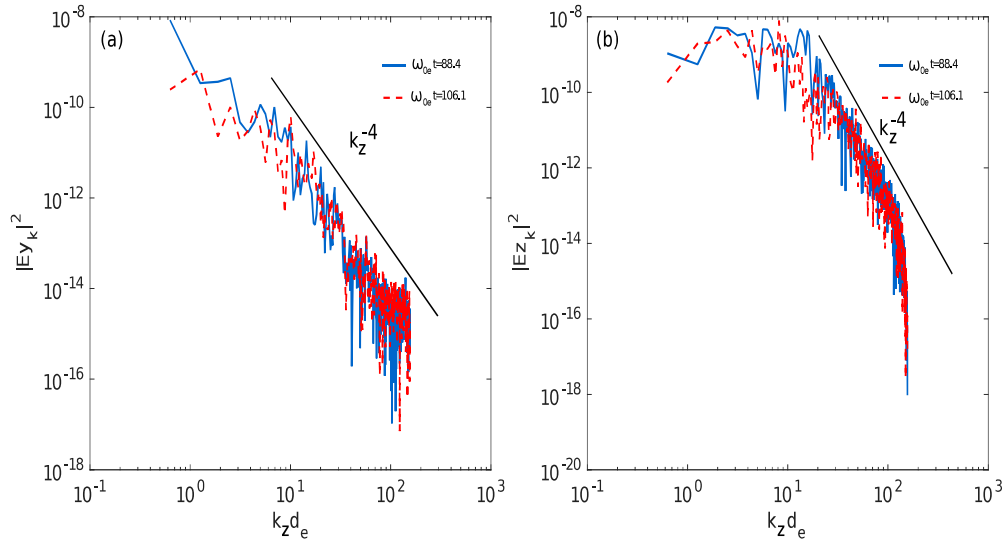
Figure 6.14: Longitudinal spectrum of electric field energy with time for case ($V_0 = 0.1c$, $\varepsilon = 0.05d_e$). (a) spectra of y-component of electric field energy $|Ey_k|^2 = |Ey_k/(mec\omega_{0e}/e)|^2$ (b) spectra of z-component of electric field energy $|Ez_k|^2 = |Ez_k/(mec\omega_{0e}/e)|^2$.

in inset in Fig. 6.13(b) which illustrate the turbulence state of system led by KH instability. The field energy spectra of all three cases (weak, mild and strong relativistic cases) has a power law (k_z^p) behaviuor (see Fig. 6.13, Fig. 6.14, Fig. 6.15 and Fig. 6.16) and the spectral scaling index is found to be close to -4.

For mild relativistic case ($V_0 = 0.9c$, ε=0.05 c/ω_{0e}), the energy spectra corresponding to B_x, E_y and E_z are shown in Fig. 6.15 (b), (c) and (d) respectively at different times. We have observed a bump in magnetic field energy spectra at higher k_z (≈ 100) and power of this bump increases with time which means that the magnetic field energies are trapped in these small scale structures however, the power of intermediate k_z is transfered to lower k_z with time through nonlinear interaction which in turn power to bigger magnetic structures.

For strong relativistic case ($V_0 = 0.9c$, ε=0.05 c/ω_{0e}), the magnetic field energy spectra are shown in Fig. 6.16(b). We observe a bump at higher k_z and that is similar to previous mild relativistic case ($V_0 = 0.5c$, ε=0.05 c/ω_{0e}) but with more power. The energy spectra corresponding to y-component of electric field is shown in Fig. 6.16 (c) at various times.
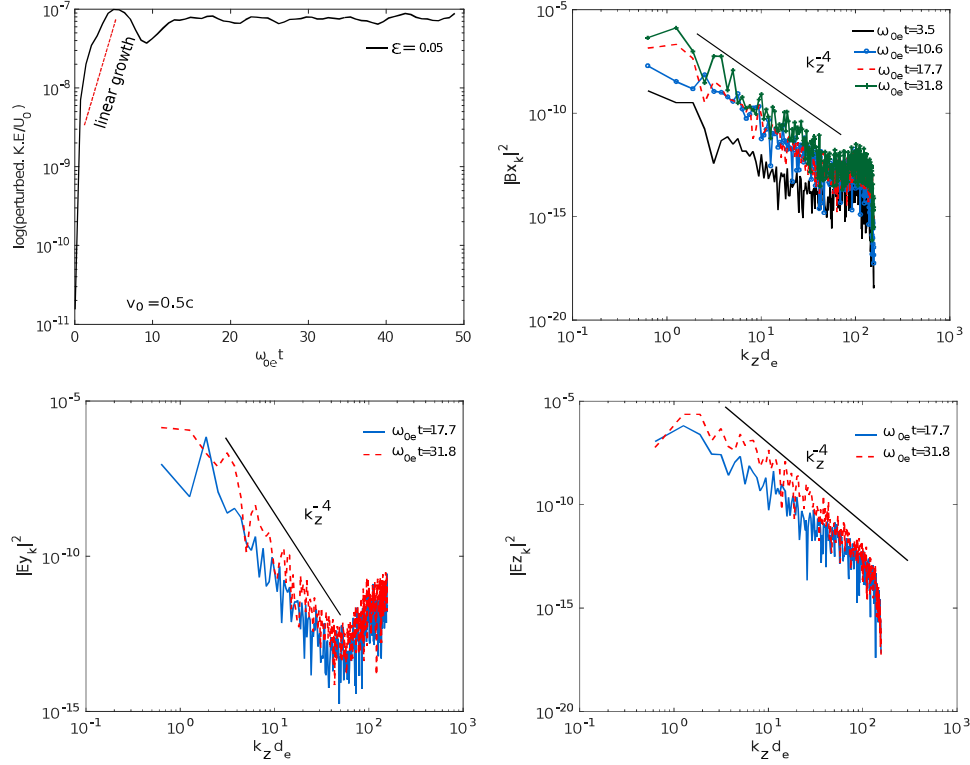
Figure 6.15: perturbed kinetic energy and fields spectra for strong-relativistic case ($V_0 = 0.9c$, ε=0.05 c/ω_{0e}) (a) Time evolution of perturbed kinetic energy (b) longitudinal spectra of magnetic field energy $|Bx_k|^2 = |Bx_k/(mec\omega_{0e}/e)|^2$ (c) longitudinal spectra of y-component of electric field energy $|Ey_k|^2 = |Ey_k/(mec\omega_{0e}/e)|^2$ (d) spectra of z-component of electric field energy $|Ez_k|^2 = |Ez_k/(mec\omega_{0e}/e)|^2$.
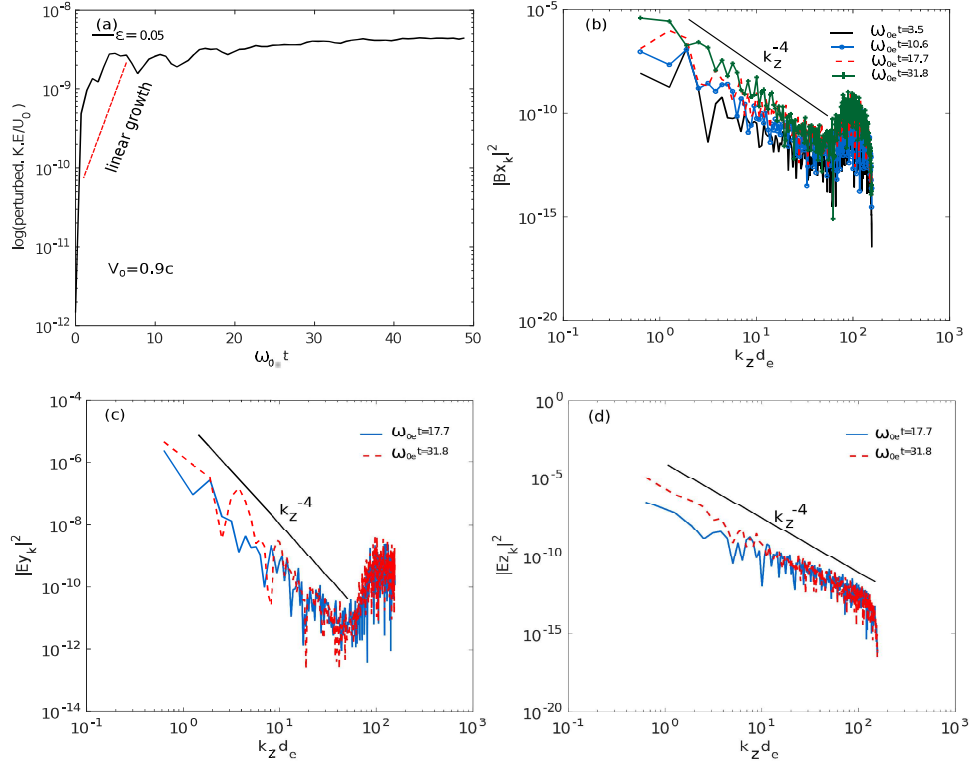
Figure 6.16: perturbed kinetic energy and fields spectra for strong-relativistic case ($V_0 = 0.9c$, ε=0.05 c/ω_{0e}) (a) Time evolution of perturbed kinetic energy (b) longitudinal spectra of magnetic field energy $|Bx_k|^2 = |Bx_k/(mec\omega_{0e}/e)|^2$ (c) longitudinal spectra of y-component of electric field energy $|Ey_k|^2 = |Ey_k/(mec\omega_{0e}/e)|^2$ (d) spectra of z-component of electric field energy $|Ez_k|^2 = |Ez_k/(mec\omega_{0e}/e)|^2$.

6.5   Summary

In summary, we have carried out two-dimension electromagnetic PIC simulation on 2D electron velocity shear flow instability and we have shown the formation of electromagnetic KH vortices in 2-D sheared electron velocity flow configuration against a neutralizing background of ions for weak relativistic cases ($V_0 = 0.1c, \varepsilon = 0.05c/\omega_{0e}$) what have been predicted by EMHD model. However, for mild and strong relativistic case, we have seen the compression and rarefaction in plasma density in transverse direction of sheared-flow and this compression and rarefaction in plasma density increases with velocity of flow. This puts constraint on EMHD model to be used to describe the sheared-flow instability in relativistic regime. In order to understand the compression and rarefaction in mild and strong relativistic flow cases, we model the phenomena by a one-dimensional magnetized relativistic electron fluid equations for electrostatic disturbances and found that compression and rarefaction are upper hybrid oscillation which breaks in nonlinear regime. The spectral behavior of magnetic and electric fields in turbulent stage for weak relativistic regime shows the smooth transition of energy from lower k modes to higher k modes while in mild and strong relativistic cases the energy is trapped in higher k modes which do not change with time.

7

Conclusion and future scope

The interaction of laser with plasma is a highly non-linear process where several complex phenomena take place simultaneously. The experimental investigations are limited in terms of available diagnostics. Numerical simulations, in this scenario, appears as a useful aid. The other advantage of the numerical technique is that one can investigate the response of the system by switching on and off certain physical effects. In the present thesis, Particle-In-Cell (PIC) simulation technique has been adopted to study the electron time scale phenomena in the context of intense laser-plasma interaction. In the preceding chapters, the detail description of some of the studies carried out by us has been presented. We briefly provide a summary of the major findings of the thesis here. The future scope of work has also been identified.

7.1 Main results of the thesis

7.1.1 Enhanced laser energy absorption rate: role of structured targets

One important issue associated with the interaction of laser with plasma is the question of laser energy absorption. One would like to have a mechanism of possible control over this process so as to maneuver the amount of energy absorbed by the plasma. We have provided such a possibility in terms of using structured targets. It has been shown with the help of 2D3V PIC simulations that an appropriate structured configuration of the target can enhance the absorption of laser light.

A structured target gets ionized by the prepulse of a strong laser field. The main pulse, therefore, encounters a structured plasma profile for interaction which is in general overdense. This is because the expansion of the plasma is considerably small by the time the main pulse hits the target after ionization. The energy transfer in this configuration takes place through vacuum heating mechanism proposed by Brunel [3]. This mechanism requires the electric field component of the laser light to be directed perpendicular to the surface which helps in dragging the electrons out of the surface. This is possible only for a p - polarised light incident at an angle. For a planar target, a normally incident light pulse will not be able to transfer any energy to the plasma by this mechanism. On the other hand, if the target surface is corrugated or rippled then there are local regions on the surface for which a normal component of the electric field exists. Furthermore, the effective surface area also gets enhanced. We have shown that both these effects are instrumental in increasing the absorption. We also show that when the ripple spacing is smaller than the typical electron displacement over one cycle of the laser pulse, the absorption efficiency does not improve much. This is so because the intergroove distance, in this case, is such that the electrons which are pulled out from one plasma surface are essentially moved inside the other adjacent region of the plasma. Thus the optimal requirement is that the surface corrugations should be high so that the surface area increases, but smaller compared to the electron displacement in the quiver electric field of the laser.

7.1.2   1-D studies on electron beam propagation in plasmas: the role of plasma density inhomogeneity

Once the electrons acquire energy by the laser efficiently, one would be interested in its efficient transport to the regions within the plasma where one hopes to deposit them. This is essentially the problem of energetic electron beam propagation in plasmas which is known to be beset with various beam-plasma instabilities. These instabilities and possible ways to suppress them have been looked into 1-D and 2-D configurations.

A counterstreaming beam-plasma electron system is considered as an equilibrium configuration in an inhomogeneous plasma medium transverse to the beam propagation direction. In the 1-D configuration, variations transverse to the prop-

agating beam have been permitted. Our simulation study shows that the growth rate of Weibel instability as a function of wavenumber gets suppressed in the presence of plasma inhomogeneity. The numerically obtained growth rate has been found to compare well with approximate analytical predictions made by Mishra *et al.* [56]. The reduction in growth rate can be understood by realising that the transverse electromagnetic perturbation in an un-magnetized plasma with scale length shorter than the skin depth is typically damped. When the plasma density inhomogeneity scale length (perpendicular to the flow direction) is shorter than skin depth it provides a coupling between the growing electromagnetic mode and the short scale perturbations. Thus, the density ripple acts as a conduit for the transfer of the energy of the growing mode to short scale damped perturbations resulting in the suppression of the mode.

7.1.3 2-D studies on electron beam propagation

We considered the evolution of pure Weibel mode in a 2-D configuration for which the variations were confined in a plane transverse to the propagation direction. A kinetic dispersion relation for beam-plasma system was obtained, which shows that the linear growth rate of Weibel instability reduces with beam temperature. The simulation results also confirm this. We have observed the magnetic field (B_z^2) as well as current filaments with the size of skin depth in linear regime of cold beam-plasma system while for warm beam-plasma system strength of such filaments is very weak.

In the nonlinear regime, the like current filaments (formed by the process of Weibel destabilization) start merging. The magnetic field inside the current filaments is found to be large enough to trap the electrons. This is the main cause of saturation of instability. The trapped electrons oscillate with a frequency which is known as bounce frequency. We have estimated the saturated magnetic field by comparing this bounce frequency to the maximum growth rate of linear Weibel instability. The estimate is in good agreement with PIC simulation result.

It is known that in the beam plasma system the oblique modes have a maximum growth rate. We investigated the role of plasma density inhomogeneity on these modes by PIC studies. The 2-D plane formed by the inhomogeneity and the flow direction showed the suppression of the oblique modes in the presence

of inhomogeneous plasma density. The suppression in growth rate was compared with the growth rate obtained from a linearised treatment of two fluid description. Both approaches indicate that there is a reduction in growth rate when the inhomogeneity scale length is found to be less than the plasma skin depth.

7.1.4 2-D studies of electron velocity shear driven instability

The Weibel separated current filaments have a sheared electron current flow configuration. Thus shear flow instabilities would have a role after the Weibel separation occurs in a beam plasma system. Furthermore, since the laser spot size is typically finite, the electron beam generated by such a laser would also have a finite extent. Thus even before a sheared electron flow configuration of Weibel separated currents arise, from the very beginning of electron beam propagation in the plasma the edges would be susceptible to sheared flow instabilities.

In the past, several authors have studied the electron sheared flow instabilities using a simplified EMHD description. It is an incompressible fluid description of magnetized electron flow. The displacement current is not taken into account in this simple model. Also, the relativistic effects are totally ignored in the EMHD description. Sita *et al.* [6] studied the sheared flow instability in the relativistic regime by introducing the relativistic mass variations due to the shear electron flow.

We investigate the sheared electron flow instability through PIC studies which contains all the effects for example compressibility, relativistic mass variation and displacement currents.

- **Shear flow driven instability in various regime**

  The linear stability analysis of shear driven instability for the 2-D sheared flow in weakly relativistic regime shows the existence of K-H instability when shear scale is sharper than skin depth otherwise system is highly stable. Moreover, we have also observed the development of K-H vortices in the shear region which ultimately merge to form longer structures. All observations in weak relativistic flow are in conformity of the fluid EMHD theory.

- **Upper hybrid oscillations in mild and relativistic flow**

In the mild and strong relativistic case, the compressibility effects are dominant and we have observed a characteristic electrostatic oscillations transverse to the flow direction which is Upper Hybrid Oscillation (UHO). This overwhelms the K-H in the system.

- **2-D turbulence in sheared electron flow**

  The nonlinear regime, in all cases, shows broad power spectra of the magnetic field which is indicative of turbulence excitation. We have observed that in both strong and weak relativistic cases, the spectra are broad and have power law behavior. The spectral scaling index is found to be close to -4. In the strong relativistic case, we have observed that the power law extends towards the longer wavelength region nearly at the order of skin depth whereas this is not so for the weak relativistic case. It appears that it is easier to generate longer scales in the strongly relativistic case.

7.2 Future scope of the work

The thesis provides many directions for experimental as well theoretical explorations.

7.2.1 Experimental explorations

For instance, the novel vacuum heating effects associated with structured targets demonstrated in the thesis for enhanced laser absorption can be tested in laboratory experiments. There are already some indications of the suppression of beam plasma instability in inhomogeneous plasmas created by attaching nanowires [56, 103, 104]. Such experiments can be carried out in detail to explore the role of density scale length and inhomogeneity amplitude. An optimized design of the target can be proposed based on the twin requirement of efficient absorption as well as unhindered propagation in the plasma.

7.2.2 Theoretical and simulation

It appears that the finite size of the electron beam adds novel effects related to the shear flow instabilities. It was earlier believed to play a role only after the Weibel

separated current led to a sheared configuration in an infinite periodic system. We have shown that the sheared flow instabilities in this case invariably involves upper hybrid oscillations and their associated wave breaking. The study of wave breaking phenomena for magnetized systems are thus of paramount importance and need to be pursued.

The thesis has restricted to 2-D simulations. In 3-D nonlinear regime, it is well known that the hydrodynamic flows do not permit inverse cascade towards long scales. An extension to 3-D simulations for this problem where electron are magnetized and relativistic would, therefore, be of interest. The ensuing characteristic of turbulence would be interesting to pursue.

Some laboratory experiments have now been able to explore the regime of ion response for the generation of turbulent magnetic fields. In this context, it will be interesting to extend beam-plasma simulations with ion response and characterize the behaviour of turbulence in detail.

Bibliography

[1] M. Tabak, D. S. Clark, S. P. Hatchett, M. H. Key, B. F. Lasinski, R. A. Snavely, S. C. Wilks, R. P. J. Town, R. Stephens, E. M. Campbell, R. Kodama, K. Mima, K. A. Tanaka, S. Atzeni, and R. Freeman. Review of progress in fast ignitiona. *Physics of Plasmas*, 12(057305), 2005.

[2] A Upadhyay, K Patel, B S Rao, P A Naik, and P D Gupta. Three-dimensional simulation of laser-plasma based electron acceleration. *Pramana - J Phys*, 78(613), 2012.

[3] F. Brunel. Not-so-resonant, resonant absorption. *Phys. Rev. Lett.*, 59(52), Jul 1987.

[4] Erich S. Weibel. Spontaneously growing transverse waves in a plasma due to an anisotropic velocity distribution. *Phys. Rev. Lett.*, 2(83), Feb 1959.

[5] Burton D. Fried. Mechanism for instability of transverse plasma waves. *Physics of Fluids*, 2(3), 1959.

[6] Sita Sundar and Amita Das. Electron velocity shear driven instability in relativistic regime. *Physics of Plasmas*, 17(022101), 2010.

[7] Amita Das. Nonlinear aspects of two-dimensional electron magnetohydrodynamics. *Plasma Physics and Controlled Fusion*, 41(A531), 1999.

[8] Max Tabak, James Hammer, Michael E. Glinsky, William L. Kruer, Scott C. Wilks, John Woodworth, E. Michael Campbell, Michael D. Perry, and Rodney J. Mason. Ignition and high gain with ultrapowerful lasers*. *Physics of Plasmas*, 1(1626), 1994.

[9] R Kodama, P A Norreys, K. Mima, A. E. Dangor, R. G. Evans, H. Fujita, Y. Kitagawa, K. Krushelnick, T. Miyakoshi, N. Miyanaga, T. Norimatsu, S. J. Rose, T. Shozaki, K. Shigemori, A. Sunahara, M. Tampo, K. A. Tanaka, Y. Toyama, Y. Yamanaka, and M. Zepf. Fast heating of ultrahigh-density plasma as a step towards laser fusion ignition. *Nature*, 412(798-802), 2001.

[10] T. Tajima and J. M. Dawson. Laser electron accelerator. *Phys. Rev. Lett.*, 43(267), Jul 1979.

[11] C. Joshi, W. B. Mori, T. Katsouleas, J. M. Dawson, J. M. Kindel, and D. W. Forslund. Ultrahigh gradient particle acceleration by intense laser-driven plasma density waves. *Nature*, 311(525-529), 1984.

[12] M. Litos, E. Adli, W. An, C. I. Clarke, C. E. Clayton, S. Corde, J. P. Delahaye, R. J. England, A. S. Fisher, J. Frederico, S. Gessner, S. Z. Green, M. J. Hogan, C. Joshi, W. Lu, K. A. Marsh, W. B. Mori, P. Muggli, N. Vafaei-Najafabadi, D. Walz, G. White, Z. Wu, V. Yakimenko, and G. Yocky. High-efficiency acceleration of an electron beam in a plasma wakefield accelerator. *Nature*, 515(92-95), 2014.

[13] J. Fuchs, J. C. Adam, F. Amiranoff, S. D. Baton, P. Gallant, L. Gremillet, A. Héron, J. C. Kieffer, G. Laval, G. Malka, J. L. Miquel, P. Mora, H. Pépin, and C. Rousseaux. Transmission through highly overdense plasma slabs with a subpicosecond relativistic laser pulse. *Phys. Rev. Lett.*, 80(2326), Mar 1998.

[14] F. Califano, N. Attico, F. Pegoraro, G. Bertin, and S. V. Bulanov. Fast formation of magnetic islands in a plasma in the presence of counterstreaming electrons. *Phys. Rev. Lett.*, 86(5293), Jun 2001.

[15] P. M. Nilson, L. Willingale, M. C. Kaluza, C. Kamperidis, S. Minardi, M. S. Wei, P. Fernandes, M. Notley, S. Bandyopadhyay, M. Sherlock, R. J. Kingham, M. Tatarakis, Z. Najmudin, W. Rozmus, R. G. Evans, M. G. Haines, A. E. Dangor, and K. Krushelnick. Magnetic reconnection and plasma dynamics in two-beam laser-solid interactions. *Phys. Rev. Lett.*, 97(255001), Dec 2006.

[16] Jiayong Zhong, Yutong Li, Xiaogang Wang, Jiaqi Wang, Quanli Dong, Chijie Xiao, Shoujun Wang, Xun Liu, Lei Zhang, Lin An, Feilu Wang, Jianqiang Zhu, Yuan Gu, Xiantu He, Gang Zhao, and Jie Zhang. Modelling loop-top x-ray source and reconnection outflows in solar flares with intense lasers. *Nature*, 6(984–987), 2010.

[17] Bruce A. Remington, David Arnett, R. Paul, Drake, and Hideaki Takabe. Modeling astrophysical phenomena in the laboratory with intense lasers. *Science*, 284(5419):1488–1493, 1999.

124

[18] M. Lazar, R. Schlickeiser, R. Wielebinski, and S. Poedts. Cosmological effects of weibel-type instabilities. *The Astrophysical Journal*, 693(2):1133, 2009.

[19] G. Kulcsár, D. AlMawlawi, F. W. Budnik, P. R. Herman, M. Moskovits, L. Zhao, and R. S. Marjoribanks. Intense picosecond x-ray pulses from laser plasmas by use of nanostructured "velvet" targets. *Phys. Rev. Lett.*, 84(5149), May 2000.

[20] Subhendu Kahaly, S. K. Yadav, W. M. Wang, S. Sengupta, Z. M. Sheng, A. Das, P. K. Kaw, and G. Ravindra Kumar. Near-complete absorption of intense, ultrashort laser light by sub-λ gratings. *Phys. Rev. Lett.*, 101(145001), Sep 2008.

[21] P. P. Rajeev, P. Taneja, P. Ayyub, A. S. Sandhu, and G. Ravindra Kumar. Metal nanoplasmas as bright sources of hard x-ray pulses. *Phys. Rev. Lett.*, 90(115002), Mar 2003.

[22] A. L. Lei, K. A. Tanaka, R. Kodama, G. R. Kumar, K. Nagai, T. Norimatsu, T. Yabuuchi, and K. Mima. Optimum hot electron production with low-density foams for laser fusion by fast ignition. *Phys. Rev. Lett.*, 96(255006), Jun 2006.

[23] C. Gahn, G. Pretzler, A. Saemann, G. D. Tsakiris, K. J. Witte, D. Gassmann, T. Schätz, U. Schramm, P. Thirolf, and D. Habs. Mev $\gamma-$ ray yield from solid targets irradiated with fs-laser pulses. *Applied Physics Letters*, 73(3662), 1998.

[24] Gourab Chatterjee, Prashant Kumar Singh, Saima Ahmed, A. P. L. Robinson, Amit D. Lad, Sudipta Mondal, V. Narayanan, Iti Srivastava, Nikhil Koratkar, John Pasley, A. K. Sood, and G. Ravindra Kumar. Macroscopic transport of mega-ampere electron currents in aligned carbon-nanotube arrays. *Phys. Rev. Lett.*, 108(235005), Jun 2012.

[25] A. P. L. Robinson and M. Sherlock. Magnetic collimation of fast electrons produced by ultraintense laser irradiation by structuring the target composition. *Physics of Plasmas*, 14(083105), 2007.

[26] L. Spitzer. Physics of fully ionized gases. *Interscience Publishers,Inc., New York*, 1956.

[27] R. G. Meyerand and A. F. Haught. Gas breakdown at optical frequencies. *Phys. Rev. Lett.*, 11(401), Nov 1963.

[28] S. Rand. Inverse bremsstrahlung with high-intensity radiation fields. *Phys. Rev.*, 136(B231), Oct 1964.

[29] R. More, Z . Zinamon, K. Warren, R . Falcone, and M. Murnane. Heating of solids with ultra-short laser pulses. *Journal de Physique Colloques*, 49(C7-43-C7-51.), 1988.

[30] P. Gibbon. *Short Pulse Laser Interactions with Matter*. Imperial College Press, London, 2005.

[31] T.Y. Brian Yang, William L. Kruer, Richard M. More, and A. Bruce Langdon. Absorption of laser light in overdense plasmas by sheath inverse bremsstrahlung. *Physics of Plasmas*, 2(3146), 1995.

[32] T.Y. Brian Yang, William L. Kruer, A. Bruce Langdon, and Tudor W. Johnston. Mechanisms for collisionless absorption of light waves obliquely incident on overdense plasmas with steep density gradients. *Physics of Plasmas*, 3(2702), 1996.

[33] D. W. Forslund, J. M. Kindel, Kenneth Lee, E. L. Lindman, and R. L. Morse. Theory and simulation of resonant absorption in a hot plasma. *Phys. Rev. A*, 11(679), Feb 1975.

[34] W. L. Kruer and Kent Estabrook. J×b heating by very intense laser light. *Physics of Fluids*, 28(430), 1985.

[35] S. C. Wilks, W. L. Kruer, M. Tabak, and A. B. Langdon. Absorption of ultra-intense laser pulses. *Phys. Rev. Lett.*, 69(1383), Aug 1992.

[36] G. Malka and J. L. Miquel. Experimental confirmation of ponderomotive-force electrons produced by an ultrarelativistic laser pulse on a solid target. *Phys. Rev. Lett.*, 77(75), Jul 1996.

[37] Z.-M. Sheng, K. Mima, Y. Sentoku, M. S. Jovanović, T. Taguchi, J. Zhang, and J. Meyer-ter Vehn. Stochastic heating and acceleration of electrons in colliding laser fields in plasma. *Phys. Rev. Lett.*, 88(055004), Jan 2002.

[38] J. F. Drake, P. K. Kaw, Y. C. Lee, G. Schmid, C. S. Liu, and Marshall N. Rosenbluth. Parametric instabilities of electromagnetic waves in plasmas. *Physics of Fluids*, 17(778), 1974.

[39] M. H. Key, M. D. Cable, T. E. Cowan, K. G. Estabrook, B. A. Hammel, S. P. Hatchett, E. A. Henry, D. E. Hinkel, J. D. Kilkenny, J. A. Koch, W. L. Kruer, A. B. Langdon, B. F. Lasinski, R. W. Lee, B. J. MacGowan, A. MacKinnon, J. D. Moody, M. J. Moran, A. A. Offenberger, D. M. Pennington, M. D. Perry, T. J. Phillips, T. C. Sangster, M. S. Singh, M. A. Stoyer, M. Tabak, G. L. Tietbohl, M. Tsukamoto, K. Wharton, and S. C. Wilks. Hot electron production and heating by hot electrons in fast ignitor research. *Physics of Plasmas*, 5(1966), 1998.

[40] L. Gremillet, F. Amiranoff, S. D. Baton, J.-C. Gauthier, M. Koenig, E. Martinolli, F. Pisani, G. Bonnaud, C. Lebourg, C. Rousseaux, C. Toupin, A. Antonicci, D. Batani, A. Bernardinello, T. Hall, D. Scott, P. Norreys, H. Bandulet, and H. Pépin. Time-resolved observation of ultrahigh intensity laser-produced electron jets propagating through transparent solid targets. *Phys. Rev. Lett.*, 83(5015), Dec 1999.

[41] D. Bohm and E. P. Gross. Theory of plasma oscillations. a. origin of medium-like behavior. *Phys. Rev.*, 75(1851), Jun 1949.

[42] F. Califano, R. Prandi, F. Pegoraro, and S. V. Bulanov. Nonlinear filamentation instability driven by an inhomogeneous current in a collisionless plasma. *Phys. Rev. E*, 58(7837), Dec 1998.

[43] Irving Langmuir. Scattering of electrons in ionized gases. *Phys. Rev.*, 26(585), Nov 1925.

[44] Laurent Gremillet, Guy Bonnaud, and Francois Amiranoff. Filamented transport of laser-generated relativistic electrons penetrating a solid target. *Physics of Plasmas*, 9(941), 2002.

[45] P. A. Norreys, F. N. Beg, Y. Sentoku, L. O. Silva, R. A. Smith, and R. M. G. M. Trines. Intense laser-plasma interactions: New frontiers in high energy density physics. *Physics of Plasmas*, 16(041002), 2009.

[46] H. M. Milchberg, R. R. Freeman, S. C. Davey, and R. M. More. Resistivity of a simple metal from room temperature to 10^6 k. *Phys. Rev. Lett.*, 61(2364), Nov 1988.

[47] J. A. Cobble, G. A. Kyrala, A. A. Hauer, A. J. Taylor, C. C. Gomez, N. D. Delamater, and G. T. Schappert. Kilovolt x-ray spectroscopy of a subpicosecond-laser-excited source. *Phys. Rev. A*, 39(454), Jan 1989.

[48] M. I. K. Santala, M. Zepf, I. Watts, F. N. Beg, E. Clark, M. Tatarakis, K. Krushelnick, A. E. Dangor, T. McCanny, I. Spencer, R. P. Singhal, K. W. D. Ledingham, S. C. Wilks, A. C. Machacek, J. S. Wark, R. Allott, R. J. Clarke, and P. A. Norreys. Effect of the plasma density scale length on the direction of fast electrons in relativistic laser-solid interactions. *Phys. Rev. Lett.*, 84(1459), Feb 2000.

[49] Q. L. Dong and J. Zhang. Electron acceleration by static and oscillating electric fields produced in the interaction between femtosecond laser pulses and solid targets. *Physics of Plasmas*, 8(1025), 2001.

[50] J. Kupersztych, M. Raynaud, and C. Riconda. Electron acceleration by surface plasma waves in the interaction between femtosecond laser pulses and sharp-edged overdense plasmas. *Physics of Plasmas*, 11(1669), 2004.

[51] M. Raynaud, J. Kupersztych, C. Riconda, J. C. Adam, and A. Heron. Strongly enhanced laser absorption and electron acceleration via resonant excitation of surface plasma waves. *Physics of Plasmas*, 14, 2007.

[52] K. Eidmann, R. Rix, T. Schlegel, and K. Witte. Absorption of intense high-contrast sub-picosecond laser pulses in solid targets. *EPL (Europhysics Letters)*, 55(3), 2001.

[53] D. G. Stearns, O. L. Landen, E. M. Campbell, and J. H. Scofield. Generation of ultrashort x-ray pulses. *Phys. Rev. A*, 37(1684), Mar 1988.

[54] O. Culfa, G. J. Tallents, E. Wagenaars, C. P. Ridgers, R. J. Dance, A. K. Rossall, R. J. Gray, P. McKenna, C. D. R. Brown, S. F. James, D. J. Hoarty, N. Booth, A. P. L. Robinson, K. L. Lancaster, S. A. Pikuz, A. Ya. Faenov, T. Kampfer, K. S. Schulze, I. Uschmann, and N. C. Woolsey. Hot electron production in laser solid interactions with a controlled pre-pulse. *Physics of Plasmas*, 21(043106), 2014.

[55] B. Ramakrishna, S. Kar, A. P. L. Robinson, D. J. Adams, K. Markey, M. N. Quinn, X. H. Yuan, P. McKenna, K. L. Lancaster, J. S. Green, R. H. H. Scott, P. A. Norreys, J. Schreiber, and M. Zepf. Laser-driven fast electron collimation in targets with resistivity boundary. *Phys. Rev. Lett.*, 105(135001), Sep 2010.

[56] S. K. Mishra, Predhiman Kaw, A. Das, S. Sengupta, and G. Ravindra Kumar. Stabilization of beam−weibel instability by equilibrium density ripples. *Physics of Plasmas (1994-present)*, 21(012108), 2014.

[57] C. M. Huntington, F. Fiuza, J. S. Ross, A. B. Zylstra, R. P. Drake, D. H. Froula, G. Gregori, N. L. Kugland, C. C. Kuranz, M. C. Levy, C. K. Li, J. Meinecke, T. Morita, R. Petrasso, C. Plechaty, B. A. Remington, D. D. Ryutov, Y. Sakawa, A. Spitkovsky, H. Takabe, and H.-S. Park. Observation of magnetic field generation via the weibel instability in interpenetrating plasma flows. *Nature Physics*, 11(173–176), 2015.

[58] Amita Das and Predhiman Kaw. Nonlocal sausage-like instability of current channels in electron magnetohydrodynamics. *Physics of Plasmas*, 8(4518), 2001.

[59] Neeraj Jain, Amita Das, Predhiman Kaw, and Sudip Sengupta. Role of current shear driven turbulence in anomalous stopping of energetic electrons. *Physics Letters A*, 363:125 − 129, 2007.

[60] H. Matsumoto and Y. Omura. *Computer Space Plasma Physics: Simulation Techniques and Software:KEMPO1*. Terra Scientific Publishing Company (TERRAPUB), Tokyo, 1993.

[61] William H. Press, Saul A. Teukolsky, William T. Vetterling, and Brian P. Flannery. *Numerical Recipes in C*. Cambridge University Press, 1992.

[62] Charles K. Birdsall and A. Bruce Langdon. *Plasma physics via computer simulation*. Series in plasma physics. Taylor & Francis, New York, 1985. Originally published: New York ; London : McGraw-Hill, 1985.

[63] Roger W. Hockney and James W. Eastwood. *Computer simulation using particles*. Adam Hilger, Bristol, 1988. Includes indexes.

[64] T. Umeda, Y. Omura, T. Tominaga, and H. Matsumoto. A new charge conservation method in electromagnetic particle-in-cell simulations. *Computer Physics Communications*, 156(73-85), December 2003.

[65] R. B. Stephens, R. A. Snavely, Y. Aglitskiy, F. Amiranoff, C. Andersen, D. Batani, S. D. Baton, T. Cowan, R. R. Freeman, T. Hall, S. P. Hatchett, J. M. Hill, M. H. Key, J. A. King, J. A. Koch, M. Koenig, A. J. MacKinnon, K. L. Lancaster, E. Martinolli, P. Norreys, E. Perelli-Cippo, M. Rabec Le Gloahec, C. Rousseaux, J. J. Santos, and F. Scianitti. K_α fluorescence measurement of relativistic electron transport in the context of fast ignition. *Phys. Rev. E*, 69(066414), Jun 2004.

[66] S. Kar, A. P. L. Robinson, D. C Carroll, O Lundh, K. Markey, P. McKenna, P. Norreys, and M. Zepf. Guiding of relativistic electron beams in solid targets by resistively controlled magnetic fields. *Phys. Rev. Lett.*, 102(055001), Feb 2009.

[67] J. Fuchs, P. Antici, E. DHumires, E. Lefebvre, M. Borghesi, E. Brambrink, C. A. Cecchetti, M. Kaluza, V. Malka, M. Manclossi, S. Meyroneinc, P. Mora, J. Schreiber, T. Toncian, and H. Ppin. Laser-driven proton scaling laws and new paths towards energy increase. *Nature Physics*, 2(48–54), 2006.

[68] Antoine Rousse, Christian Rischel, and Jean-Claude Gauthier. Femtosecond x-ray crystallography. *Rev. Mod. Phys.*, 73(17–31), Jan 2001.

[69] L. M. Chen, F. Liu, W. M. Wang, M. Kando, J. Y. Mao, L. Zhang, J. L. Ma, Y. T. Li, S. V. Bulanov, T. Tajima, Y. Kato, Z. M. Sheng, Z. Y. Wei,

and J. Zhang. Intense high-contrast femtosecond k-shell x-ray source from laser-driven ar clusters. *Phys. Rev. Lett.*, 104(215004), May 2010.

[70] U. Teubner and P. Gibbon. High-order harmonics from laser-irradiated plasma surfaces. *Rev. Mod. Phys.*, 81(445–479), Apr 2009.

[71] Hong-bo Cai, Wei Yu, Shao ping Zhu, Chun yang Zheng, Li hua Cao, Bin Li, Z. Y. Chen, and A. Bogerts. Short-pulse laser absorption in very steep plasma density gradients. *Phys. Plasmas*, 13(094504), 2006.

[72] K.-H. Hong, B. Hou, J. A. Nees, E. Power, and G. A. Mourou. Generation and measurement of $>10^8$ intensity contrast ratio in a relativistic khz chirped-pulse amplified laser. *Applied Physics B*, 81(4), 2005.

[73] J. D. Kmetec, C. L. Gordon, J. J. Macklin, B. E. Lemoff, G. S. Brown, and S. E. Harris. Mev x-ray generation with a femtosecond laser. *Phys. Rev. Lett.*, 68(1527), Mar 1992.

[74] M. P. Kalashnikov, E. Risse, H. Schönnagel, and W. Sandner. Double chirped-pulse-amplification laser: a way to clean pulses temporally. *Opt. Lett.*, 30(8), Apr 2005.

[75] Hiromitsu Kiriyama, Norihiro Inoue, Yutaka Akahane, and Koichi Yamakawa. Prepulse-free, multi-terawatt, sub-30-fs laser system. *Opt. Express*, 14(1), Jan 2006.

[76] J. E. Crow, P. L. Auer, and J. E. Allen. The expansion of a plasma into a vacuum. *Journal of Plasma Physics*, 14(65–76), 8 1975.

[77] L. V. Pariiskaya A. V. Gurevich and L. P. Pitaevskii. Self-similar motion of rarefied plasma. *JETP*, 22(449), 1966.

[78] C. Ren, M. Tzoufras, J. Tonge, W. B. Mori, F. S. Tsung, M. Fiore, R. A. Fonseca, L. O. Silva, J.-C. Adam, and A. Héron. A global simulation for laser-driven mev electrons in 50 -μm-diameter fast ignition targets. *Phys. Plasmas*, 13(056308), 2006.

[79] Sharad Kumar Yadav. *ELECTRON MAGNETOHYDRODYNAMIC (EMHD) STUDIES ON ELECTRON TRANSPORT IN AN INHOMOGENEOUS PLASMA MEDIUM.* PhD thesis, Institute for Plasma Research, HBNI, 2011.

[80] S. K. Yadav, A. Das, and P. Kaw. Propagation of electron magnetohydrodynamic structures in a two-dimensional inhomogeneous plasma. *Physics of Plasmas*, 15(062308), 2008.

[81] S. Kar, A. P. L. Robinson, D. C Carroll, O Lundh, K. Markey, P. McKenna, P. Norreys, and M. Zepf. Guiding of relativistic electron beams in solid targets by resistively controlled magnetic fields. *Phys. Rev. Lett.*, 102(055001), FEBRUARY 2009.

[82] Jeremy Martin Hill, Michael H. Key, Stephen P. Hatchett, and Richard R. Freeman. Beam-weibel filamentation instability in near-term and fast-ignition experiments. *Physics of Plasmas (1994-present)*, 12(082304), 2005.

[83] A. R. Bell and R. J. Kingham. Resistive collimation of electron beams in laser-produced plasmas. *Phys. Rev. Lett.*, 91(035003), Jul 2003.

[84] A. P. L. Robinson, M. Sherlock, and P. A. Norreys. Artificial collimation of fast-electron beams with two laser pulses. *Phys. Rev. Lett.*, 100(025002), Jan 2008.

[85] P. McKenna, A. P. L. Robinson, D. Neely, M. P. Desjarlais, D. C. Carroll, M. N. Quinn, X. H. Yuan, C. M. Brenner, M. Burza, M. Coury, P. Gallegos, R. J. Gray, K. L. Lancaster, Y. T. Li, X. X. Lin, O. Tresca, and C.-G. Wahlström. Effect of lattice structure on energetic electron transport in solids irradiated by ultraintense laser pulses. *Phys. Rev. Lett.*, 106(185004), May 2011.

[86] Roswell Lee and Martin Lampe. Electromagnetic instabilities, filamentation, and focusing of relativistic electron beams. *Phys. Rev. Lett.*, 31(1390), Dec 1973.

[87] Luís O. Silva, Ricardo A. Fonseca, John W. Tonge, Warren B. Mori, and John M. Dawson. On the role of the purely transverse weibel instability in fast ignitor scenarios. *Physics of Plasmas (1994-present)*, 9(2458), 2002.

[88] Amita Das, Neeraj Jain, Predhiman Kaw, and Sudip Sengupta. Sausage instabilities in the electron current layer and its role in the concept of fast ignition. *Nuclear Fusion*, 44(1):98, 2004.

[89] Neeraj Jain, Amita Das, and Predhiman Kaw. Kink instability in electron magnetohydrodynamics. *Physics of Plasmas*, 11(4390), 2004.

[90] J.H. Nuckolls, L.Wood, A.Thiessen, and G.B.Zimmerman. Laser compression of matter to super-high densities: Thermonuclear (ctr) applications. *Nature*, 239(139), 1972.

[91] Yosuke Mizuno, Philip E. Hardee, and Ken-Ichi Nishikawa. Spatial growth of the current-driven instability in relativistic jets. *APJ*, 784(167), 2014.

[92] R.A. Chevalier, J. M. Blondin, and R. T. Emmering. Hydrodynamic instabilities in supernova remnants: self-similar driven waves. *Astrophysical Journal*, 392:118–130, 1992.

[93] K.-I. Nishikawa, Hardee P., Zhang B., Dutan I., Medvedev M., Choi E. J., Min K. W., Niemiec J., Mizuno Y., Nordlund A., Frederiksen J. T., Sol H., and and D. H. Hartmann Pohl M. Magnetic field generation in a jet-sheath plasma via the kinetic kelvin-helmholtz instability. *Annales Geophysicae*, 31(9):1535–1541, 2013.

[94] T Yabuuchi, A Das, G R Kumar, H Habara, P K Kaw, R Kodama, K Mima, P A Norreys, S Sengupta, and K A Tanaka. Evidence of anomalous resistivity for hot electron propagation through a dense fusion core in fast ignition experiments. *New Journal of Physics*, 11(9):093031, 2009.

[95] A. Modena. Electron acceleration from the breaking of relativistic plasma waves. *Nature*, 377(606–608), 1995.

[96] K. B. Wharton, S. P. Hatchett, S. C. Wilks, M. H. Key, J. D. Moody, V. Yanovsky, A. A. Offenberger, B. A. Hammel, M. D. Perry, and C. Joshi.

Experimental measurements of hot electrons generated by ultraintense ($>10^{19}$ w/cm^2) laser-plasma interactions on solid-density targets. *Phys. Rev. Lett.*, 81(822), Jul 1998.

[97] C. Shukla, A. Das, and K. Patel. Effect of finite beam width on current separation in beam plasma system: Particle-in-cell simulations. *preprint arXiv.org*, 2015.

[98] S. V. Bulanov, F. Pegoraro, and A. S. Sakharov. Magnetic reconnection in electron magnetohydrodynamics. *Physics of Fluids B*, 4(8), 1992.

[99] D. Jovanović and F. Pegoraro. Two-dimensional electron-magnetohydrodynamic nonlinear structures. *Physics of Plasmas*, 7(889), 2000.

[100] P. G. Drazin and W. H. Rnumber. *Hydrodynamic Stability*. Cambridge University Press, Cambridge, 1982.

[101] G. Bodo, A. Mignone, and R. Rosner. Kelvin-helmholtz instability for relativistic fluids. *Phys. Rev. E*, 70(036304), Sep 2004.

[102] P. L. Pritchett and F. V. Coroniti. The collisionless macroscopic kelvin-helmholtz instability: 1. transverse electrostatic mode. *Journal of Geophysical Research: Space Physics*, 89(A1), 1984.

[103] Chandrasekhar Shukla, Amita Das, and Kartik Patel. 1d3v pic simulation of propagation of relativistic electron beam in an inhomogeneous plasma. *Phys. Scr.*, 90(085605(10p)), 2015.

[104] Chandrasekhar Shukla, Amita Das, and Kartik Patel. Two-dimensional studies of relativistic electron beam plasma instabilities in an inhomogeneous plasma. *Physics of Plasmas*, 22(112118), 2015.

[105] J.P. Boris, A.M. Landsberg, E.S. Oran, and J.H. Gardner. Lcpfct - a flux-corrected transport algorithm for solving generalized continuity equations. Technical Report NRL Memorandum Report 93-7192., Navel Research Laboratory, 1993.

134

[106] Sy-Bor Wen, Mao, Xianglei, Greif, Ralph, Russo, and Richard E. Laser ablation induced vapor plume expansion into a background gas. ii. experimental analysis. *Journal of Applied Physics*, 101(023115), 2007.

[107] J. R. Pierce. Possible fluctuations in electron streams due to ions. *Journal of Applied Physics*, 19(231), 1948.

[108] A. P. L. Robinson, M. Sherlock, and P. A. Norreys. Artificial collimation of fast-electron beams with two laser pulses. *Phys. Rev. Lett.*, 100(025002), Jan 2008.

[109] G. Malka and J. L. Miquel. Experimental confirmation of ponderomotive-force electrons produced by an ultrarelativistic laser pulse on a solid target. *Phys. Rev. Lett.*, 77(75), Jul 1996.

[110] Marian Karlický. Electron beam-plasma interaction and the return-current formation. *The Astrophysical Journal*, 690(1), 2009.

[111] A. Bret, L. Gremillet, and M. E. Dieckmann. Multidimensional electron beam-plasma instabilities in the relativistic regime. *Physics of Plasmas*, 17(120501), 2010.

[112] B. Ramakrishna, S. Kar, A. P. L. Robinson, D. J. Adams, K. Markey, M. N. Quinn, X. H. Yuan, P. McKenna, K. L. Lancaster, J. S. Green, R. H. H. Scott, P. A. Norreys, J. Schreiber, and M. Zepf. Laser-driven fast electron collimation in targets with resistivity boundary. *Phys. Rev. Lett.*, 105(135001), Sep 2010.

[113] J.R. Cary, Lester E. Thode, Don S. Lemons, Michael E. Jones, and Michael A. Mostrom. Simple criteria for the absence of the beam−weibel instability. *Physics of Fluids (1958-1988)*, 24(10), 1981.

[114] Han S. Uhm and Martin Lampe. Return−current−driven instabilities of propagating electron beams. *Physics of Fluids (1958-1988)*, 25(8), 1982.

[115] Jeremy Martin Hill, Michael H. Key, Stephen P. Hatchett, and Richard R. Freeman. Beam-weibel filamentation instability in near-term and fast-ignition experiments. *Physics of Plasmas (1994-present)*, 12(082304), 2005.

[116] M. Tatarakis, F. N. Beg, E. L. Clark, A. E. Dangor, R. D. Edwards, R. G. Evans, T. J. Goldsack, K. W. D. Ledingham, P. A. Norreys, M. A. Sinclair, M-S. Wei, M. Zepf, and K. Krushelnick. Propagation instabilities of high-intensity laser-produced electron beams. *Phys. Rev. Lett.*, 90(175001), Apr 2003.

[117] F. Califano, N. Attico, F. Pegoraro, G. Bertin, and S. V. Bulanov. Fast formation of magnetic islands in a plasma in the presence of counterstreaming electrons. *Phys. Rev. Lett.*, 86(5293), Jun 2001.

[118] A. Bret and C. Deutsch. Hierarchy of beam plasma instabilities up to high beam densities for fast ignition scenario. *Physics of Plasmas (1994-present)*, 12(082704), 2005.

[119] A. J. Mackinnon, Y. Sentoku, P. K. Patel, D. W. Price, S. Hatchett, M. H. Key, C. Andersen, R. Snavely, and R. R. Freeman. Enhancement of proton acceleration by hot-electron recirculation in thin foils irradiated by ultraintense laser pulses. *Phys. Rev. Lett.*, 88(215006), May 2002.

[120] G. Malka and J. L. Miquel. Experimental confirmation of ponderomotive-force electrons produced by an ultrarelativistic laser pulse on a solid target. *Phys. Rev. Lett.*, 77(75), Jul 1996.

[121] H.-S. Park, D. M. Chambers, H.-K. Chung, R. J. Clarke, R. Eagleton, E. Giraldez, T. Goldsack, R. Heathcote, N. Izumi, M. H. Key, J. A. King, J. A. Koch, O. L. Landen, A. Nikroo, P. K. Patel, D. F. Price, B. A. Remington, H. F. Robey, R. A. Snavely, D. A. Steinman, R. B. Stephens, C. Stoeckl, M. Storm, M. Tabak, W. Theobald, R. P. J. Town, J. E. Wickersham, and B. B. Zhang. High-energy kÎś radiography using high-intensity, short-pulse lasersa. *Physics of Plasmas (1994-present)*, 13(056309), 2006.

[122] T. Taguchi, T. M. Antonsen, and K. Mima. Study of hot electron beam transport in high density plasma using 3d hybrid-darwin code. *Computer Physics Communications*, 164(1-3), 2004.

136

[123] A. Bret, M.-C. Firpo, and C. Deutsch. Collective electromagnetic modes for beam-plasma interaction in the whole k space. *Phys. Rev. E*, 70(046401), Oct 2004.

[124] Jacob Trier Frederiksen and Mark Eric Dieckmann. Electromagnetic turbulence driven by the mixed mode instability. *Physics of Plasmas (1994-present)*, 15(094503), 2008.

[125] M. E. Dieckmann, J. T. Frederiksen, A. Bret, and P. K. Shukla. Evolution of the fastest-growing relativistic mixed mode instability driven by a tenuous plasma beam in one and two dimensions. *Physics of Plasmas (1994-present)*, 13(112110), 2006.